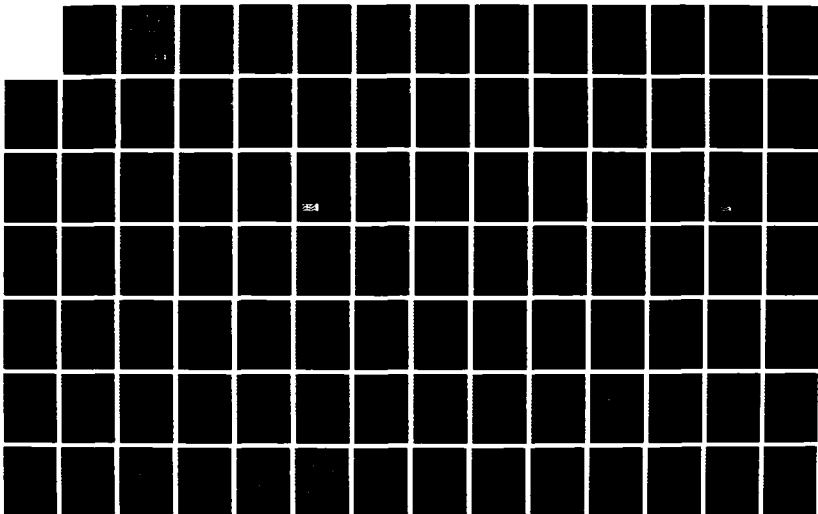RARE GAS HALIDE (RGH) KINETICS(U) SPECTRA TECHNOLOGY
INC BELLEVUE WA W D KIMURA FEB 88 C-11-333
N00014-85-C-0043

UNCLASSIFIED
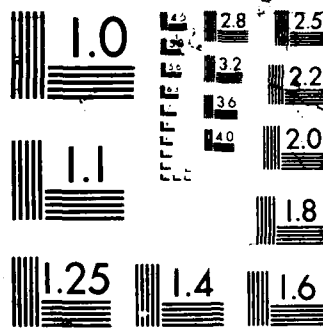
F/G 7/2

NL

⑤ Spectra Technology

AD-A192 352

Contract N00014-85-C-0843

RARE GAS HALIDE (RGH) KINETICS FINAL REPORT

Submitted to
OFFICE OF NAVAL RESEARCH
DEPARTMENT OF THE NAVY

Submitted by
SPECTRA TECHNOLOGY, INC.

DTIC
ELECTE
MAR 1 7 1988
S ᵃ D
H

February 1988

88 2 29 012

Ⓢ Spectra Technology

RARE GAS HALIDE (RGH) KINETICS FINAL REPORT

Submitted to
OFFICE OF NAVAL RESEARCH
DEPARTMENT OF THE NAVY

Submitted by
SPECTRA TECHNOLOGY, INC.

February 1988

C.11.333

Contract #: N00014-85-C-0843

Final Report

for

Rare Gas Halide (RGH) Kinetics

Submitted to

OFFICE OF NAVAL RESEARCH
Department of the Navy
800 N. Quincy Street
Arlington, VA 22217-5000

by

SPECTRA TECHNOLOGY, INC.
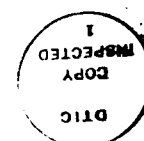2755 Northup Way
Bellevue, WA 98004-1495

Wayne D. Kimura
Principal Investigator

Doreen Pillie
Proposer's Contracting Official

Telephone: (206) 827-0460

Facsimile: (206) 828-3517

February 1988

Accession For	
NTIS GRA&I	☑
DTIC TAB	☐
Unannounced	☐
Justification	
By	
Distribution/	
Availability Codes	
Dist	Avail and/or Special
A-1	

TABLE OF CONTENTS

Section		Page

i

Section 1

EXECUTIVE SUMMARY AND RECOMMENDATIONS

1.1 BACKGROUND

The understanding and model validation of electron beam (e-beam) pumped XeCl kinetics has lagged that of the other excimers, primarily because of the lack of appropriate data with which to check the models. The goal of this program was to measure fundamental quantities in e-beam excited XeCl mixtures and use this data to help improve and validate existing codes. As an added benefit, some data was also obtained in XeF and KrF laser mixtures in parallel programs. This data, whose collection was not part of the original statement of work for this program, has proven very valuable in elucidating the differences between XeCl and the other excimers.

The work performed during this program resulted in a number of papers being written, some of which have been published in scientific journals and others that are still being reviewed. Since these papers describe the experiments, data, and analysis in great detail, the bulk of this final report are reprints of these papers. They are contained in the appendix after this section. The remainder of this section summarizes the accomplishments of this program and ends with a discussion of the consequences of the work and recommendations for additional experiments.

1.2 PROGRAM ACCOMPLISHMENTS

During this program the following tasks were successfully completed:

1) The electron beam for the Tahoma laser, used during all the measurements, was upgraded to enable 1 μs e-beam pulse durations and energy loadings >100 J/ℓ. The long e-beam pulse length is important

for measuring certain kinetics phenomenon such as halogen depletion.

2) Time-dependent electron densities in XeCl, XeF, and KrF were measured as a function of initial halogen and minor rare gas concentrations. The most noteworthy result of these measurements is that the electron density is higher than was expected.

3) Depletion of the HCl halogen donor in XeCl was measured after termination of the e-beam pulse. Although not a time-dependent measurement, the results demonstrate that a considerable amount of halogen is depleted during the e-beam pulse. This depletion is also higher than expected.

4) Time-dependent xenon excited state densities in XeCl and XeF were measured as a function of initial halogen concentration and e-beam pulse duration. The xenon excited state density behaves in several unexpected ways that are described in the papers.

5) The XeCl computer model was upgraded and compared with the experimental data. In particular, it was determined that careful calculation of the electron energy distribution is necessary in order to predict the observed electron density behavior. The code comes close to predicting the measured electron density, xenon excited state density, and HCl depletion; however, best agreement between the code and the data occurs only when additional HCl depletion is included above what the model predicts.

As a result of this work, the following papers were written and are located in the appendix of this report:

1. W.D. Kimura, D.R. Guyer, S.E. Moody, J.F. Seamans, and D.H. Ford, "Electron Density Measurements in Electron-Beam Pumped XeCl Laser Mixtures," Appl. Phys. Lett., 49, 1569 (1986).

2. W.D. Kimura, D.R. Guyer, S.E. Moody, J.F. Seamans, and D.H. Ford, "Electron Density Measurements in Electron-Beam Pumped XeF and KrF Laser Mixtures," Appl. Phys. Lett., 50, 60 (1987).

3. D.R. Guyer, W.D. Kimura, and S.E. Moody, "HCl Burnup and Electron Densities in E-Beam Pumped XeCl," in Proceedings of the International Conference on Lasers '86, R.W. McMillan, Editor (STS Press, McLean, 1987), pp. 589-593.

4. F. Kannari and W.D. Kimura, "Kinetics Issues of Electron Beam Pumped KrF Lasers," in Proceedings of the International Conference on Lasers '86, R.W. McMillan, Editor (STS Press, McLean, 1987), pp. 446-452.

5. F. Kannari, W.D. Kimura, J.F. Seamans, and D.R. Guyer, "Xenon Excited State Density Measurements in Electron-Beam Pumped XeCl Laser Mixtures," Appl. Phys. Lett., 51, 1986 (1987).

6. F. Kannari, W.D. Kimura, J.F. Seamans, and D.R. Guyer, "Xenon Excited State Densities in Electron-Beam Pumped XeCl and XeF," submitted to Journal of Applied Physics.

7. F. Kannari and W.D. Kimura, "High-Energy Electron Distribution in Electron-Beam Excited Ar/Kr and Ne/Xe Mixtures," to be published in Journal of Applied Physics, April 15, 1988.

8. F. Kannari and W.D. Kimura, "Low-Energy Electron Distribution in Electron-Beam Excited XeCl Laser Mixtures," submitted to Journal of Applied Physics.

9. W.D. Kimura, F. Kannari, J.F. Seamans, and D.R. Guyer, "Diagnostic Techniques for Studying Excimer Laser Kinetics," Excimer Laser Technology and Advanced Scientific Applications, R. Sauerbrey and J.H. Tillotson, Editors, to be published in Proceedings of SPIE.

Besides the preceding publications, the following papers were presented at various conferences during this program:

1. W.D. Kimura, D.R. Guyer, S.E. Moody, J.F. Seamans, and D.H. Ford, "Electron Density Measurements of XeCl, XeF, and KrF Laser Mixtures," 39th Gaseous Electronics Conference, Madison, WI, Oct. 7-10, 1986, Paper N-1.

2. E.T. Salesky and W.D. Kimura, "Model Comparisons of Electron Density Measurements in KrF, XeF, and XeCl," 39th Gaseous Electronics Conference, Madison, WI, Oct. 7-10, 1986, Paper N-2.

3. D.R. Guyer, W.D. Kimura, and S.E. Moody, "HCl Burnup and Electron Densities in E-Beam Pumped XeCl," International Conference on Lasers '86, Orlando, FL, Nov. 3-7, 1986, Paper HF.8.

4. F. Kannari, S.E. Moody, and W.D. Kimura, "Kinetics Issues of Electron Beam Pumped KrF Lasers," International Conference on Lasers '86, Orlando, FL, Nov. 3-7, 1986, Paper WK.7.

5. E.T. Salesky, W.D. Kimura, and F. Kannari, "The Role of Electron Dissociative Attachment and Impact Dissociation of HCl in XeCl Lasers," Conference on Lasers and Electro-Optics (CLEO), Baltimore, MD, Apr. 27-May 1, 1987, Paper WR4.

6. D.R. Guyer, F. Kannari, W.D. Kimura, and S.E. Moody, "Implications of Recent Kinetics Measurements in XeCl," Atomic, Molecular, and Optical Physics Meeting of the American Physical Society, Cambridge, MA, May 18-20, 1987, poster paper.

7. F. Kannari, J.F. Seamans, D.R. Guyer, and W.D. Kimura, "Xenon Excited State Density Measurements in XeCl," International Conference on Lasers '87, Lake Tahoe, NV, Dec. 7-11, 1987, Paper HK.3.

8. W.D. Kimura, F. Kannari, J.F. Seamans, and D.R. Guyer, "Diagnostic Techniques for Studying Excimer Laser Kinetics," O-E/LASE '88, Excimer Laser Technology and Advanced Scientific Applications, Los Angeles, CA, Jan. 10-15, 1988, Paper 894-09.

9. W.D. Kimura, F. Kannari, and J.J. Ewing, "Recent Developments in Understanding E-Beam Pumped XeCl Lasers," Conference on Lasers and Electro-Optics (CLEO), Anaheim, CA, Apr. 25-29, 1988, Paper TuH1.

Spectra Technology also participated in the Workshop on XeCl Kinetics held December 19, 1985 at SRI International.

1.3   DISCUSSION AND RECOMMENDATIONS

As a result of the measurements performed during this program and the refinements made to the computer model, our understanding of XeCl kinetics has increased dramatically. Qualitatively, one might state that our understanding of XeCl is now comparable to the other major excimers.

Much of the mystery associated with the XeCl kinetics has been lifted. For example, significant vibrational excitation of HCl appears to be occurring as indirectly indicated by the behavior of the electron density. The exact character of the electron energy distribution and its affect on the kinetics is now better understood. The distribution is not entirely Maxwellian, as was generally assumed by models before this work. Instead, only the low energy distribution (the distribution below the ionization energy of xenon) is Maxwellian; the high energy distribution is non-Maxwellian. The problems with assuming a Maxwellian distribution can be avoided by using a Boltzmann solution for the electron energy distribution; however, we have found that the high and low energy parts of the distribution can be solved separately, thereby simplifying the calculation process.

As with any research investigation, occasionally one finds new mysteries. In our case, the data all indicate that more HCl is being lost than can be predicted by the model. Put another way, the model predicts quite well the time-dependent electron and xenon excited state density behaviors, and the total HCL depletion, but only when additional HCl destruction to neutrals is artificially included in the model. Depletion of HCl through dissociative attachment and impact dissociation is already in the model; hence, this additional destruction channel corresponds to a process still unknown. It is important to understand this HCl loss channel because scaling of these lasers to long pulse lengths directly depends on the HCl burnup rate.

In light of this new mystery, one recommendation regarding further work in this area are experiments to determine how the additional HCl is being lost. Time-dependent measurements of the HCl(v = 0, 1, and 2) concentrations during the e-beam pulse are needed. Performing these measurements as a function of buffer gas may also provide clues regarding the role of neon and xenon is this process.

As another recommendation, it was identified during the Workshop on XeCl Kinetics that measurements of the electron density and temperature are critically needed. The electron density has now been measured; to measure the electron temperature is much more difficult. However, with the ability to measure the electron density, it may be possible to determine the electron temperature by measuring phenomena that are dependent on both electron density and temperature. For example, free-free absorption by inverse bremsstrahlung is a function of the electron velocity distribution. This distribution is dependent on the electron density and temperature; knowing the density, one can deduce the temperature.

Ultimately, the interest is in improving the performance of XeCl lasers, in particular, scaling them to longer pulse lengths. As mentioned earlier, control of halogen depletion is crucial for achieving long pulse lengths. Therefore, as a final recommendation, either experiments and/or

tests of the model should be performed to investigate methods for reducing
the total HCl depletion.

APPENDIX

Electron density measurements of electron beam pumped XeCl laser mixtures

W. D. Kimura, Dean R. Guyer, S. E. Moody, J. F. Seamans, and D. H. Ford

Spectra Technology, Incorporated, 2755 Northup Way, Bellevue, Washington 98004

Time-dependent electron density measurements of electron beam pumped XeCl laser mixtures (nonlasing) are performed using a CO_2 (10.6 μm) quadrature interferometer. The electron beam pulse length is ≈ 500 ns (full width at half-maximum) and delivers $\gtrsim 10$ A/cm² at the foil. Electron densities are measured as a function of the halogen (HCl) and xenon concentration. For a 98.3% Ne/1.5% Xe/0.16% HCl mixture at 3000 Torr, the electron density peaks near the beginning of the pulse at $\approx 7 \times 10^{14}$ cm⁻³, decreases to 3×10^{14} cm⁻³, then gradually increases to $\approx 6 \times 10^{14}$ cm⁻³ at the end of the pulse. As the initial halogen concentration is reduced, the electron density increases, rising dramatically near the end of the pulse. This increase in the electron density later in the pulse is accompanied by a decrease of the XeCl* sidelight fluorescence.

In electron beam (e-beam) pumped excimer lasers, the primary driving mechanism is e-beam generation of ions, excited states, and secondary electrons. The secondaries are involved with the excimer formation through many different channels.[1] Electrons are also important with regard to quenching of the excimer molecule and of excited states leading to the excimer formation. Due to the governing role of electrons in the kinetics of excimer lasers, there is a great deal of interest in determining the magnitude and temporal behavior of the electron density in these devices.

There have been some measurements of the electron density in discharge excimer lasers[1,5] and in e-beam pumped pure rare gases.[6] These measurements cannot be easily applied to e-beam pumped rare gas halide mixtures due to the different pumping mechanisms which exist in discharge lasers and the importance of electron attachment. Recently, the electron density in e-beam pumped Ar/HCl and Ar/F₂ mixtures has been determined.[7] This letter presents the first measurements of electron densities in e-beam pumped XeCl gas mixtures.

As shown schematically in Fig. 1, the electron density is measured using a CO_2 (10.6 μm) quadrature interferometer in which the e-beam pumped gas chamber is located in one arm of the interferometer. This gas chamber is part of the Tahoma laser system.[8] The laser mirrors have been removed and the fused silica windows on the chamber replaced with BaF_2 windows. The CO_2 laser beam has a diameter of ≈ 1 cm within the laser chamber. As is shown in Fig. 1, the beam passes twice through the chamber approximately 3 cm from the foil and centered around the nominal lasing axis. Liquid-nitrogen-cooled HgCdTe detectors, with 1.5 mm × 1.5 mm active areas, monitor the transmitted energy in the probe and reference beams.

Quadrature detection offers several advantages over conventional interferometry.[9] The primary advantage is the elimination of ambiguous interpretation of the detector signals when either passes through an extremum. This is because when one detector is at an extremum, the other detector will be at its maximum differential sensitivity and provides enough information to determine the sign of the phase shift. The output from the detectors is recorded on a dual-beam oscilloscope for later analysis.
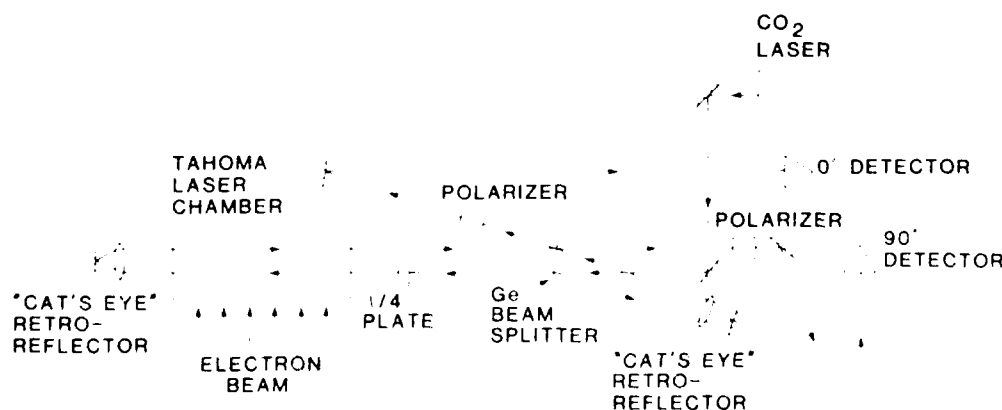

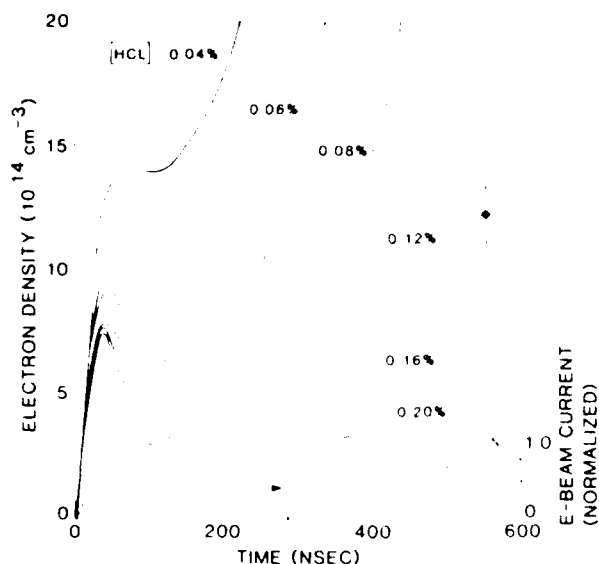FIG. 1. Schematic of electron density measurement system.

FIG. 2 Typical electron densities of XeCl mixtures (1.5% Xe, balance Ne to 3000 Torr) for various initial HCl concentrations. The dashed curve is a normalized trace of a typical electron beam current waveform. Data points are not shown, however, a representative error bar is indicated

FIG. 3 XeCl* sidelight fluorescence waveforms for the same mixtures shown in Fig. 2

The index of refraction of a weakly ionized plasma is given by

$$n_p = (1 - \omega_p^2/\omega^2)^{1/2} \approx 1 - \omega_p^2/2\omega^2 ,$$

where ω_p is the plasma frequency and ω is the optical frequency. Since $\omega_p = (4\pi e^2/m_e)n_e$, $n_p - 1 = -3.18 \times 10^9 n_e$, where e is the electron charge, m_e is the electron mass, and n_e is the electron density in cm^{-3}, the index change due to electron density is $\Delta n_p = -5.03 \times 10^{-20} n_e$. The e-beam dimensions are 10 cm × 35 cm (the e beam was baffled down to half its nominal length of 70 cm); hence, the total optical path of the laser plasma is $2 \times 35 = 70$ cm. Therefore, a shift of one fringe on our system corresponds to an electron density of $n_e = 3.0 \times 10^{14}$ cm^{-3}.

Infrared interferometry to measure electron densities is a well established technique; however, special care was taken to eliminate possible errors in the measurement. The detectors are placed a considerable distance (~18 m) from the laser chamber to eliminate detection of infrared emission from the XeCl mixture. Tare shots were taken with the reference arm of the interferometer blocked to ensure that no stray emission was being detected, and that no loss of signal was occurring due to absorption or transient refractive index effects. The issue of refractive index changes caused by resonances occurring nearby the probe wavelength has been considered by others and determined not to be a significant problem. This agrees with our own estimation that fringe shifts caused by nearby transitions, such as the 9.7 and 11.3 μm xenon lines, contribute, at most, a fraction of a fringe shift. In addition, some data were taken at 10.8 μm and yielded essentially identical results as the 10.6 μm data. Reactions occurring within the mixture can also induce an index change, but even for "worse case" estimates, they would contribute only a fraction of a fringe shift. The return to zero of the detector signal within a few microseconds after termi-
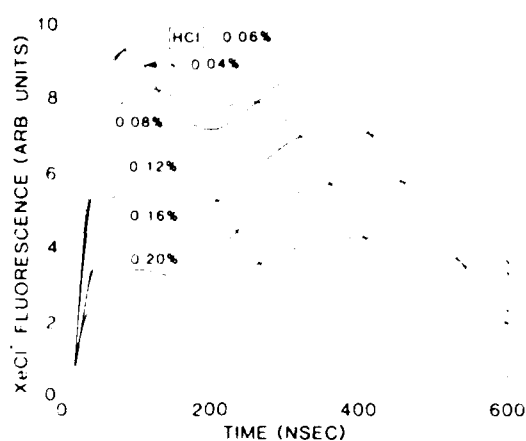
nation of the pump pulse indicates that acoustic waves in the gas chamber do not contribute to the detected index change.

The detector 3-dB bandwidths are ≈130 MHz. This causes some loss of signal amplitude during periods of rapid electron density changes; however, it does not appreciably affect the accuracy of the results. The largest uncertainty in the data is caused by the lower bandwidth limit of the detector amplifiers (5 MHz). We estimate the uncertainty to be approximately ±0.4 fringes (1.2 × 10^{14} cm^{-3}).

In all the gas mixtures, the halogen donor is HCl and the diluent is neon. Total gas pressure is 3000 Torr (3.7 amagats) and the initial temperature is 294 K. Power deposition in the gas is approximately 180 kW/cm^3 (~10 A/cm^2 at the foil), and is measured using a pressure rise technique. The e-beam source uses a carbon felt, cold cathode at 300 kV and ≈23 kA peak current

Figure 2 shows typical time-dependent electron density results for various initial HCl concentrations (the Xe concentration is constant at 1.5%). A normalized typical e-beam current pulse shape is drawn at the bottom of the figure. During the first 50 ns of the e-beam pulse, the electron density rises sharply, then gradually decreases, with the amount of decrease dependent on the initial halogen concentration. Since the dissociative attachment rate constants for HCl increase dramatically with vibrational excitation, this behavior can be attributed to the production of HCl (v > 0) during the pumping process. For a typical laser mixture of 98.3%Ne/1.5% Xe/0.16% HCl, the electron density varies between 3 and 7 × 10^{14} cm^{-3}.

A surprising result is the magnitude of the electron density; it is roughly 3-4 times larger than that predicted by a computer model developed at Spectra Technology, Inc. This has a number of important implications, some of which are discussed elsewhere and will not be examined here.

When lasing XeCl on the Tahoma device, nominal HCl concentrations range from 0.08% to 0.16%. From the electron density results, it is clear why leaner HCl concentrations do not perform as well. At lean HCl concentrations, the electron density reaches very high densities (~10^{15} cm^{-3}), which implies loss of HCl fuel and increased electron quenching. This effect can be seen more clearly in Fig. 3
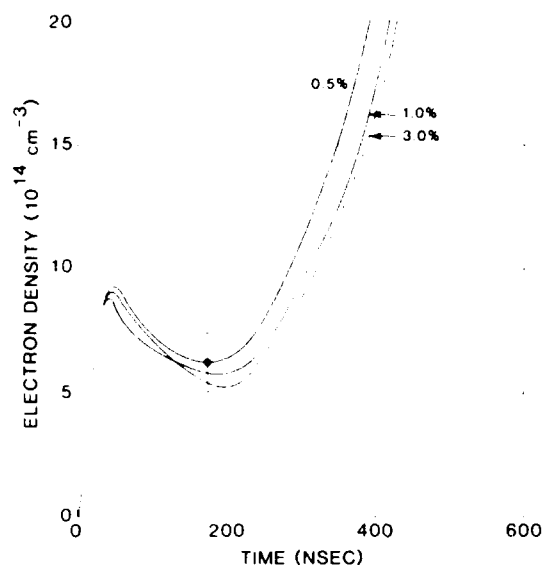
FIG. 4. Typical electron densities of XeCl mixtures (0.08% HCl, balance Ne to 3000 Torr) for various initial Xe concentrations. Data points are not shown; however, a representative error bar is indicated.

which shows the XeCl* sidelight fluorescence for the same mixtures given in Fig. 2. Although the electron density remains "under control" in the rich HCl mixtures ($\geqslant 0.16\%$ HCl), Fig. 3 demonstrates that the overall XeCl* population decreases with HCl concentrations above $\approx 0.08\%$.

Figure 4 shows the electron density for various xenon concentrations, with the HCl concentration fixed at 0.08%. There is little change with xenon concentration over the range of 0.5–3.0%.

The authors wish to acknowledge Dr. J. J. Ewing and Dr. M. J. Kushner for their helpful discussions and to thank

[1] L. A. Levin, S. E. Moody, E. L. Klosterman, R. E. Center, and J. J. Ewing, IEEE J. Quantum Electron. QE-17, 2282 (1981).

[2] F. Kannari, A. Suda, M. Obara, and T. Fujioka, IEEE J. Quantum Electron. QE-19, 1587 (1983).

[3] J. E. Ford, J. Meyer, and H. Houtman, Appl. Phys. Lett. 48, 1639 (1986).

[4] R. C. Hollins, D. L. Jordan, and J. Coutts, J. Phys. D 19, 37 (1986).

[5] M. Lando, Z. Rozenberg, and M. Rokni, "Negative Differential Conductivity in E-Beam Irradiated Ar-HCl Mixtures," Annual Conference of the Israeli Physical Society, 20 April 1986, Weitzman Institute, Rohovot, Israel.

[6] E. Zamir, C. W. Werner, W. P. Lapatovich, and E. V. George, Appl. Phys. Lett. 27, 56 (1975).

[7] Z. Rozenberg, M. Lando, and M. Rokni, "Direct Measurement of the Electron Density in Electron Beam Irradiated Ar/F₂ Gas Mixtures by Time Resolved Interferometry," Annual Conference of the Israeli Physical Society, 20 April 1986, Weitzman Institute, Rohovot, Israel.

[8] S. E. Moody, L. A. Levin, R. E. Center, J. J. Ewing, and E. L. Klosterman, IEEE J. Quantum Electron. QE-17, 1856 (1981).

[9] C. J. Buchenauer and A. R. Jacobson, Rev. Sci. Instrum. 48, 769 (1977).

[10] S. F. Fulghum, J. Rizzo, D. W. Trainor, C. Appel, in digest of Conference on Lasers and Electro-Optics (CLEO), June 9–13, 1986, Session TuN4.

[11] M. J. Weber, ed., CRC Handbook of Laser Science and Technology (CRC, Boca Raton, 1982), Vol. II, p. 97.

[12] E. T. Salesky and W. D. Kimura, IEEE J. Quantum Electron. QE-21, 1761 (1985).

[13] M. Allan and S. F. Wong, J. Chem. Phys. 74, 1687 (1981).

[14] R. E. Center and H. L. Chen, J. Chem. Phys. 61, 3785 (1974).

[15] E. T. Salesky and W. D. Kimura, "Model Comparisons of Electron Density Measurements in KrF, XeF, and XeCl," 39th Gaseous Electronics Conference, Oct. 7–10, 1986, Madison, WI, Session N-2.

[16] M. J. Kushner, "Implication of Attachment Rates on KrF Laser Performance in Light of Recent Measurements of Electron Density," 39th Gaseous Electronics Conference, Oct. 7–10, 1986, Madison, WI, Session N-3.

Electron density measurements of electron-beam-pumped XeF and KrF laser mixtures

W. D. Kimura, Dean R. Guyer, S. E. Moody, J. F. Seamans, and D. H. Ford

Spectra Technology, Incorporated, 2755 Northup Way, Bellevue, Washington 98004

A CO_2 quadrature interferometer is used to measure the temporal evolution of the electron density in XeF and KrF electron-beam-pumped laser mixtures (nonlasing). Measurements are obtained using a 300-kV electron beam which delivers $\gtrsim 10$ A/cm^2 at the foil for pulse durations $\lesssim 650$ ns (FWHM). For typical XeF mixtures (99.35% Ne/0.5% Xe/0.15% F_2 at 2888 Torr) the electron density varies between 3 and 4.5×10^{14} cm^{-3} during the pulse. The electron density is found to increase as the initial F_2 concentration is decreased. Both 10% Kr in argon diluent and argon-free KrF mixtures are tested. The electron density for these mixtures has the same magnitude and behavior as the typical XeF mixture.

Several computer models of electron-beam (*e*-beam)-pumped XeF and KrF lasers exist.[1-4] All the models rely on verification using experimental data on the laser performance, for example, the laser output flux and efficiency. The models have been very useful in improving the understanding of the complex plasma chemistry which occurs in these lasers. One key area is the role of the primary and secondary electrons which are very important in the formation of the excimers, both through ionic and metastable channels[5] and in quenching of excited states.[6] Despite the importance of the electrons, none of the codes has been validated with regard to their predictions of the electron densities, primarily because of the lack of experimental data.

This letter reports the first measurements of electron densities in *e*-beam-pumped XeF and KrF (10% Kr and argon-free) laser mixtures under nonlasing conditions. Electron density measurements have been previously reported in discharge pumped XeCl[7,8] and XeF[9]; and, recently, the electron density in *e*-beam-pumped Ar/F_2 and Ar/HCl has been measured.[10,11] An earlier letter[12] gives the electron density results for *e*-beam-pumped XeCl laser mixtures.

The experimental system is described in more detail elsewhere.[12] Briefly, the gas chamber of the Tahoma laser system[13] is placed in one arm of a CO_2 (10.6 μm) quadrature interferometer.[14] The electron density is determined from the refractive index change of the plasma due to the presence of free electrons. In this particular experiment, one fringe shift corresponds to an electron density of 3.0×10^{14} cm^{-3}.

The electron beam source is a carbon felt, cold cathode at 300 kV with a peak emission current of ≈ 23 kA. The current density at the foil (0.13 mm aluminized Kapton) is $\gtrsim 10$ A/cm^2. A pressure rise technique[15] is used to calibrate the power deposition in the gas mixtures. In the XeF gas mixtures, the deposition is ≈ 180 kW/cm^3. In the KrF gas mixtures, the deposition is kept constant at ≈ 120 kW/cm^3 by adjusting the total pressure of the gas mixtures to compensate for the different electron stopping powers of Ar and Kr. All measurements are performed at 294 K.

Figure 1 shows typical time-dependent electron density results for XeF as a function of the F_2 concentration. The XeF mixture is 0.5% Xe in Ne diluent to a total gas pressure of 2888 Torr. For reference, Fig. 2 shows a normalized typi-

cal trace of the excimer sidelight fluorescence for the 0.15% F_2 XeF mixture (the same trace is also representative of the KrF* sidelight fluorescence for the data given in Fig. 3). The top of Fig. 3 gives a normalized typical pulse shape of the *e*-beam current. The *e*-beam pulse length does vary slightly shot to shot; some of the data curves (e.g., the 0.15% and 0.20% F_2 mixtures in Fig. 1) represent data for pulse lengths shorter than shown in Fig. 2 and the top of Fig. 3.

As seen in Fig. 1, as the initial halogen concentration is reduced, the electron density tends to increase more rapidly towards the end of the pulse. This is not surprising, since as the F_2 is depleted (burned up), due to the dissociative attachment with electrons, less F_2 is available to control the electron density. Without the attacher, the electron density appears to approach the higher densities found in *e*-beam-pumped pure rare gas mixtures.[16] Dissociative recombination of the electrons with dimer ions does not help control the electron density because the dimer ion number density tends to be too small[2,3] for the conditions of this experiment. The rapid increase in the electron density as the halogen is depleted has been predicted in *e*-beam sustained discharge models,[4] but the increase tends to be at least an order of
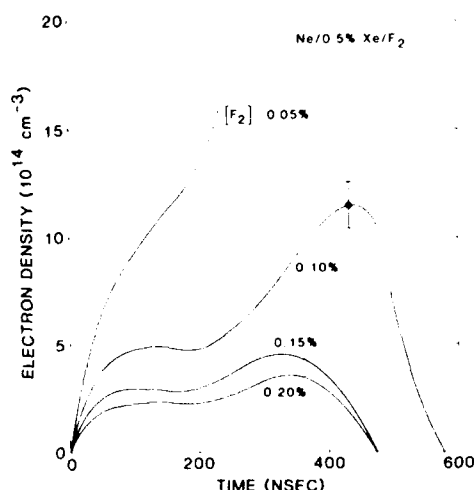

FIG. 1. Typical electron densities of XeF mixtures (0.5% Xe, balance Ne to 2888 Torr) for various initial F_2 concentrations. Data points are not shown; however, a representative error bar is indicated.
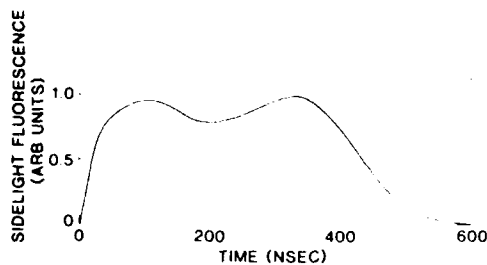
FIG. 2. Normalized waveform of typical XeF* and KrF* sidelight fluorescence emission for the data given in Figs. 1 and 3.

magnitude larger than the results in Fig. 1. Since the mechanism for electron population growth in discharge lasers (metastable ionization leading to electron avalanche and arcing) is very different from that in e-beam-pumped systems, care must be taken when comparing the two pumping schemes.

From past experience[17] on the Tahoma laser device, for these pulse lengths, the optimum laser performance on XeF occurs at F_2 concentrations of 0.10–0.15%. At higher F_2 concentrations, although the electron density may decrease, there is a significant increase in F_2 quenching and F_2 absorption which reduces the laser efficiency. The electron density profiles in Fig. 1 do not display a peak in the density at the beginning of the pulse as is seen in the XeCl data.[12]

The electron density results for the KrF mixtures are given in Fig. 3. The mixtures are 89.7% Ar/10% Kr/0.27% F_2 at 1007 Torr, and 99.6% Kr/0.4% F_2 at 665 Torr. For both mixtures, the F_2 partial pressure is 2.7 Torr, corresponding to a density of 8.9×10^{16} cm^{-3}. The electron density behavior is very similar between the two KrF mixtures. The slight increase in density towards the end of the pulse is apparently due to F_2 burn-up.

To investigate the effects of high-energy loading, measurements are performed on the 10% Kr and Kr/F_2 mixtures for e-beam pulse lengths of 650 ns (FWHM). The results are depicted in Fig. 4. The F_2 concentration has been increased in the 10% Kr mixture to 5 Torr (1.6×10^{17}
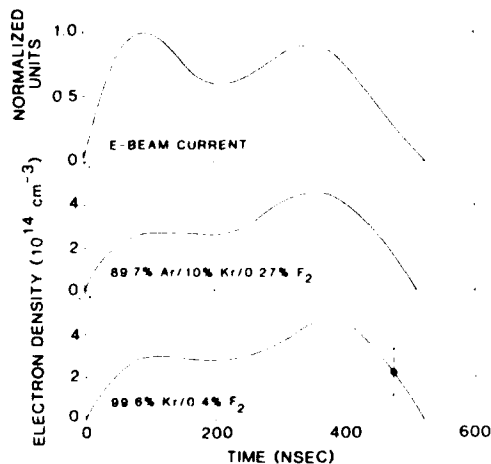

FIG. 3. Typical electron densities of KrF mixtures (89.7% Ar/10% Kr/0.27% F_2 at 1007 Torr, and 99.6% Kr/0.4% F_2 at 665 Torr). The top trace is the normalized e-beam current pulse. Data points are not shown; however, a representative error bar is indicated.

FIG. 4. Typical electron densities of KrF mixtures (89.5% Ar/10% Kr/0.5% F_2 at 1007 Torr, and 99.4% Kr/0.6% F_2 at 665 Torr). The top trace is the normalized e-beam current pulse. Data points are not shown; however, a representative error bar is indicated.
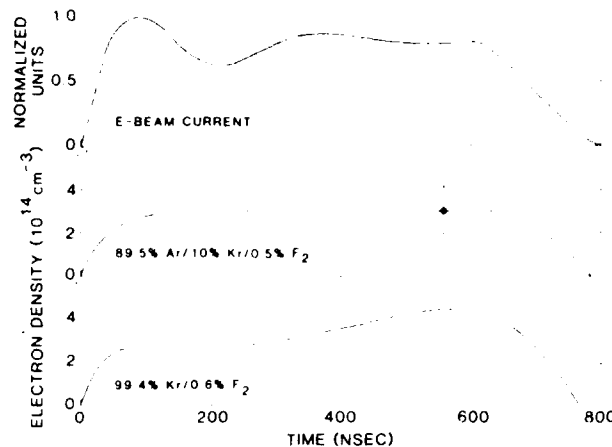
cm^{-3}), and in the Kr/F_2 mixture to 4 Torr (1.3×10^{17} cm^{-3}). At this higher F_2 concentration, the electron density for the Ar/Kr/F_2 mixture does not increase after 300 ns as seen in Fig. 3, but remains essentially constant. On the other hand, the Kr/F_2 mixture still displays a gradual increase in the electron density towards the end of the pulse. Although the initial F_2 concentration in the Kr/F_2 mixture is slightly less than in the Ar/Kr/F_2 mixture, this tendency for the electron density to be higher in the Kr/F_2 mixtures is consistent with model predictions[2] and long pulse extraction measurements.[18] Kr* is formed more efficiently in Kr/F_2 than Ar* is in Ar/Kr/F_2,[15] which means more electrons are freed per unit of power deposition. Higher gas heating effects in the Kr/F_2 mixtures also slightly increase the dissociative attachment rate constant of F_2,[19] which leads to a faster depletion of the halogen fuel and an increase in the electron density.

The KrF mixtures given in Figs. 3 and 4 represent optimum mixtures on the Tahoma laser. For the optimum XeF and KrF laser mixtures, the electron density varies between 3 and 4.5×10^{14} cm^{-3}. The density can be estimated analytically from the expression

$$n_e = \frac{P_i/(eW_i)}{k_a[F_2]}, \tag{1}$$

where n_e is the electron density, P_i is the input power deposition, (eW_i) is the energy loss per ion pair produced,[20] k_a is the F_2 attachment rate constant, and $[F_2]$ is the F_2 number density. Using a typical F_2 attachment rate constant of 2×10^{-9} cm^3/s,[19] and values for (eW_i) of 36 and 26 eV for Ne and Ar, respectively,[20] we find that electron densities of $1-2 \times 10^{14}$ cm^{-3} are predicted which are 2–3 times smaller than measured.

Although Eq. (1) may predict lower electron densities, preliminary comparisons[21] with a computer model[2] yield good agreement in overall magnitude and temporal behavior with the data. The model uses a time-dependent Boltzmann equation solution[22] and indicates that the secondary electron energy distribution is significantly non-Maxwellian for the pump conditions of this experiment. It also predicts that the

F_2 dissociative attachment rate constant is lower than that assumed in Eq. (1), which leads to higher electron densities.

The reasons the electron distribution is non-Maxwellian are complex because the distribution is affected by a variety of interrelated kinetic processes. For example, the electron dissociative attachment rate constant of F_2 is directly dependent on gas temperature[19] and inversely dependent on electron temperature.[19,23] However, Rosenberg et al.[10] show that the dissociative attachment rate constant is also a function of the F_2 concentration and e-beam current density, and that adding F_2 has the net effect of increasing the average electron temperature, caused by removal of low-energy electrons through attachment. This affects the electron energy distribution and, at the concentrations and densities used in this work, may lead to a lower attachment rate constant. Other implications of the electron density results are reported elsewhere.[24]

[1] J. A. Blauer, T. T. Yang, C. E. Turner, Jr., and D. A. Copeland, Appl. Opt. 23, 4352 (1984).

[2] E. T. Salesky, D. E. Shulman, and D. Korff, "Kinetics Modeling and Interpretation of Experimental Results, KrF," North East Research Associates, Inc. annual report from 6 May 1985 to 30 Sept. 1985 to Los Alamos National Laboratory, LAUR 86-1507.

[3] F. Kannari, M. Obara, and T. Fujioka, J. Appl. Phys. 57, 4309 (1985).

[4] T. H. Johnson and A. M. Hunter, II, J. Appl. Phys. 51, 2406 (1980).

[5] M. Rokni, J. A. Mangano, J. H. Jacob, and J. C. Hsia, IEEE J. Quantum Electron. QE-14, 464 (1978).

[6] D. W. Trainor, J. H. Jacob, and M. Rokni, J. Chem. Phys. 72, 3646 (1980).

[7] J. E. Ford, J. Meyer, and H. Houtman, Appl. Phys. Lett. 48, 1639 (1986).

[8] R. C. Hollins, D. L. Jordan, and J. Coutts, J. Phys. D 19, 37 (1986).

[9] J. F. Friichtenicht, K. R. Chien, J. Betts, and R. Stenzel, "Discharge Excimer Laser Technology," TRW, Inc. final report to the U.S. Army Ballistic Missile Technical Center, Sept. 1979 (unpublished).

[10] Z. Rozenberg, M. Lando, and M. Rokni, "Direct Measurement of the Electron Density in Electron Beam Irradiated Ar/F_2 Gas Mixtures by Time Resolved Interferometry," Annual Conference of the Israeli Physical Society, 20 April 1986, Weitzman Institute, Rohovot, Israel.

[11] M. Lando, Z. Rozenberg, and M. Rokni, "Negative Differential Conductivity in E-Beam Irradiated Ar-HCl Mixtures," Annual Conference of the Israeli Physical Society, 20 April 1986, Weitzman Institute, Rohovot, Israel.

[12] W. D. Kimura, D. R. Guyer, S. E. Moody, J. F. Seamans, and D. H. Ford, Appl. Phys. Lett. 49, 1569 (1986).

[13] S. E. Moody, L. A. Levin, R. E. Center, J. J. Ewing, and E. L. Klosterman, IEEE J. Quantum Electron. QE-17, 1856 (1981).

[14] C. J. Buchenauer and A. R. Jacobson, Rev. Sci. Instrum. 48, 769 (1977).

[15] E. T. Salesky and W. D. Kimura, IEEE J. Quantum Electron. QE-21, 1761 (1985).

[16] E. Zamir, C. W. Werner, W. P. Lapatovich, and E. V. George, Appl. Phys. Lett. 27, 56 (1975).

[17] W. D. Kimura, S. E. Moody, and J. F. Seamans, Appl. Phys. Lett. 49, 255 (1986).

[18] W. D. Kimura and E. T. Salesky, "Pump Energy Limitations of Kr/F_2 Mixtures in E-Beam Pumped KrF Lasers," Proceedings of the International Conference on Lasers '85, Las Vegas, NV, 1985, edited by C. P. Wang (STS, McLean, 1986), pp. 417-422.

[19] D. W. Trainor and J. H. Jacob, Appl. Phys. Lett. 35, 920 (1979).

[20] J. J. Ewing, in Laser Handbook, edited by M. L. Stitch (North-Holland, Amsterdam, 1979), Vol. 3, pp. 162, 163.

[21] E. T. Salesky and W. D. Kimura, "Model Comparisons of Electron Density Measurements in KrF, XeF, and XeCl," 39th Gaseous Electronics Conference, Oct. 7-10, 1986, Madison, WI, Session N-2.

[22] W. L. Morgan, Joint Institute for Laboratory Astrophysics (JILA) Information Center Report No. 19, University of Colorado, June 1979.

[23] P. Chantry, in Applied Atomic Collision Physics, Vol. 3 Gas Lasers, edited by H. S. W. Massey, E. W. McDaniel and B. Bederson (Academic, New York, 1982).

[24] M. J. Kushner, "Implication of Attachment Rates on KrF Laser Performance in Light of Recent Measurements of Electron Density," 39th Gaseous Electronics Conference, Oct. 7-10, 1986, Madison, WI, Session N-3.

KINETICS ISSUES OF ELECTRON BEAM PUMPED KrF LASERS

F. Kannari and W. D. Kimura
Spectra Technology, Inc.
2755 Northup Way
Bellevue, WA 98004

Abstract

Two separate topics are discussed in this paper. The first examines the kinetic processes associated with the secondary electrons in electron-beam excited rare-gas halide lasers. The results of experimental measurements of the secondary electron density in KrF laser mixtures suggest that the assumption of a Maxwellian electron energy distribution, used in some computer models, may not be valid under certain circumstances. Calculations of the high energy distribution of the secondary electrons produced by the electron beam also predict a non-Maxwellian distribution. Moreover, the calculated W-values [eV/electron-ion pair] and yields of rare gas metastables show a dependence on the laser mixture composition. The second topic of this paper deals with time-resolved calculations of multiplexed short-pulse amplification in KrF. The calculations include nonsaturable and saturable absorption, amplified spontaneous emission effects, and end mirrors for a double pass amplification arrangement. It is found that a train of short pulses, with a short time interval between the pulses, can extract energy from the gain media with little cost to extraction efficiency and is comparable to the performance of a contiguous train of short pulses. This suggests that a novel, simpler angular-multiplexing system can be designed for high energy, short pulse KrF laser systems.

Introduction

Efforts are currently in progress to scale up electron-beam (e-beam) pumped KrF laser to multi-10 kJ levels, to serve as drivers in advanced inertial confinement fusion.[1] Kinetics models of the KrF laser are very important tools for predicting the output performances of such systems. However, there are several important kinetics issues, which affect the basic design of these models, that are still not well understood. Some of these issues are: 1) The secondary electron energy distribution; 2) the yields of primary ionization and excitation; 3) vibrational relaxation in $KrF^*(B)$ and (C) states; 4) mixing between $KrF^*(B)$ and (C); 5) Kr_2F^* formation channels in atmospheric pressure laser mixtures; 6) nonsaturable absorptions; 7) the temperature dependences of the absorbers; and 8) photoassociative KrF^* formation. Further development of the models requires additional fundamental kinetics measurements, such as measurements of the secondary electron density and the electron mean temperature, the fluorescence yield of the $KrF^*(C)$ state, time-resolved saturated absorption at various gas temperatures, and so on.

One of these measurements, the secondary electron density, has been measured recently.[2-3] The results for e-beam pumped KrF laser mixtures[2] indicate that the density is significantly higher than that calculated by some models. This seems to imply that the treatment of the secondary electron processes, which generally has assumed a Maxwellian distribution for the electron energy distribution, is invalid.[4] In light of these measurements, the first half of this paper examines the importance of the secondary electron processes with regard to the kinetics models. Presented are the calculated results of the e-beam source energy distribution in the gas, and new results pertaining to the W-value (the energy expended per ion produced) and metastable yields in the gas mixtures.

The second half of this paper deals with another important topic related to KrF laser fusion drivers, and that is multiplexed short pulse amplification. Recent measurements[5] have shown that a train of short pulses, with an appropriate time interval between the

pulses, can extract the same energy as that by long pulses consisting of a train of contiguous short pulses without intervening time spaces. This is because of repumping occurring during the time spaces. This dynamic characteristic of KrF^* permits the design of a novel, simpler multiplexed short pulse amplifier system. By reducing the number of multiplexed beams needed, while maintaining a similar output energy as the concatenated multiplexed system, the complexity and cost of the system is reduced. In the latter half of this paper, the results of a computer simulation of this amplification concept are described. Examined are extraction efficiency and amplified spontaneous emission (ASE) effects as a function of the time space between the pulses.

Electron Density Measurements and E-Beam Source Calculation

A CO_2 quadrature interferometer is used to measure the temporal evolution of the electron density in e-beam pumped KrF laser mixtures. The experimental system has been described extensively elsewhere.[2,3] Figure 1 shows the results for mixtures of 89.5% Ar/10% Kr/0.5% F_2 at 1007 torr, and 99.4% Kr/0.6% F_2 at 665 torr. The pumping pulse width of the electron beam is ≈ 700 ns with an average excitation rate of ≈ 120 kW/cm^3. Measured electron densities are $\approx 3 \times 10^{14}$ cm^{-3} for both mixtures at early times during the pumping.

The secondary electron density can be estimated by using the excitation rate, a rate constant for F_2 dissociative attachment, and a W-value. Assuming a secondary electron temperature of 1 eV and a corresponding attachment rate of 4.5×10^{-9} cm^3/sec, which are the same assumptions used by Trainer and Jacob[6] in their paper on the electron quenching of KrF^*, an electron density of 5×10^{13} cm^{-3} is calculated. A detailed model calculation, using a Maxwellian assumption for the energy distribution of secondary electrons in conjunction with the energy balance equation, gives an electron density of 1×10^{14} cm^{-3}. Hence, the magnitude of the measured electron density is roughly 3 to 6 times larger than that predicted by the simple analysis and the model calculation.
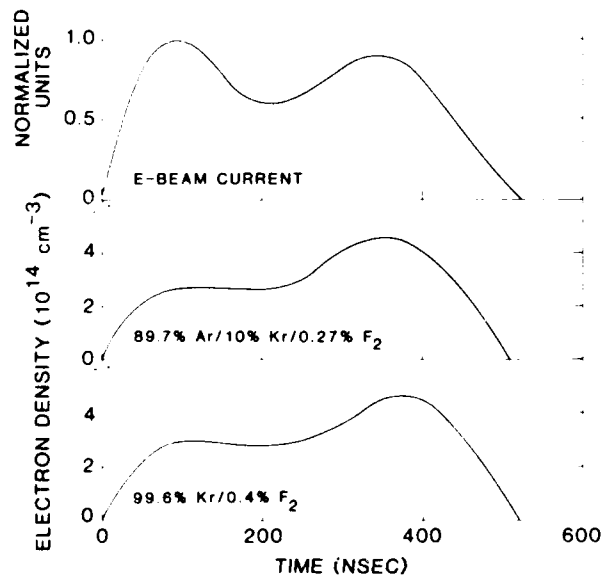

Figure 1. Typical electron densities of KrF mixtures (89.5% Ar/10% Kr/0.5% F_2 at 1007 torr, and 99.4% Kr/0.6% F_2 at 665 torr). The top trace is the normalized e-beam current pulse.

To understand the reasons for these differences, it is helpful to review the energy flow channels for the electrons in an e-beam pumped laser mixture. First, the primary electrons from the e-beam directly produce ions, secondary electrons, and excited molecules. This process is usually accounted for in the models by using a stopping power constant for the gases. The hot secondary electrons are cooled by collisions with gas molecules and produce more ions and metastables. This process is usually modeled by using W-values and the yield of metastables relative to the ion formation.[7] W-value is defined as the energy loss per

electron-ion pair produced, and is generally higher (typically a factor of 2) than the ionization potential of the atom.[8]

The primary electrons from the e-beam and the hot secondary electrons are generally treated collectively as the e-beam source. Because the preceding two processes are very fast (usually <100 ps for typical e-beam voltages and laser mixtures), the formation of the ions and metastables by the e-beam source has been treated as an instantaneous process by simply using gross macroscopic values for the stopping power constant and W-values.

The cold secondary electrons redistribute their energy through slow electron reactions such as dissociative attachment with the halogen, excitation and ionization of metastables, recombination with positive ions, elastic collisions with neutral gases, superelastic collisions, and electron-electron collisions. This redistribution can be calculated by solving the Boltzmann transport equation, as is usually done for discharge pumped lasers. However, in e-beam pumped models, the distribution of the cooled secondary electrons is many times either ignored or assumed to be Maxwellian.

To illustrate how non-Maxwellian the electron distributions can become in e-beam pumped gases, Fig. 2 shows the energy distribution of the e-beam source calculated for a laser mixture of 380 torr Ar/380 torr Kr. The method used for this calculation is based on that described by Elliott and Green.[9] The calculations in this paper also include excitation of the ground state rare-gases, as well as their ionizations.
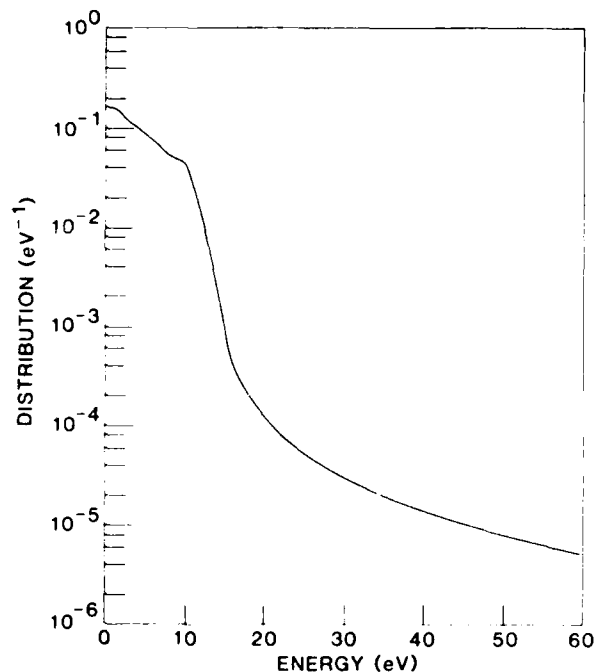
Figure 2. Energy distribution of the e-beam source in a mixture of 50% Ar/50% Kr at 760 torr.

In Fig. 2, the e-beam source distribution is truncated at a first excitation threshold of Kr(5s) at 10 eV. Note, the distribution below this first excitation threshold is very close to being Maxwellian. However, the distribution above this threshold is no longer Maxwellian. Although the slow electron reactions of the low energy electrons change the distribution, especially in the low energy part of the distribution below the excitation threshold, the high energy tail of the distribution remains relatively unchanged as it is driven by the e-beam source because the effects of slow electron reactions are negligible for high energy electrons.

Figure 3 shows how the effective W-value for the Ar ion changes as a function of the Kr concentration in an Ar/Kr mixture. The effective W-value is the W-value, calculated from the total energy deposition, times the fraction of energy deposited in Ar. Also plotted in
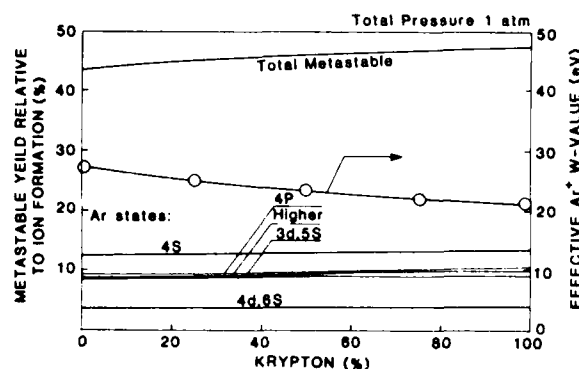
Figure 3. Plots of the effective W-values for the Ar ion and yields of Ar metastables relative to the Ar ion formation in Ar/Kr mixtures as a function of Kr concentration.

Fig. 3 are the Ar metastable yields, both for individual states and for the total yield, relative to the ion formation. It can be seen that the W-value is not a unique constant, but depends on the mixture composition. The total yield of the metastables is approximately 0.45, which is much higher than the amount typically used in the models of 0.3. Figure 4 shows the same calculations for Kr in an Ar/Kr mixture.

A Boltzmann code calculation is necessary to calculate the low energy distribution of the secondary electrons and to obtain accurate rate constants for the secondary electron reactions. This is especially true with regard to dissociative attachment by fluorine molecules, which can affect the low energy part of the electron distribution.[10] A detailed Boltzmann calculation for the low-energy electron distribution, in conjunction with a proper calculation of the e-beam source distribution for the high energy electrons, will significantly improve the models.
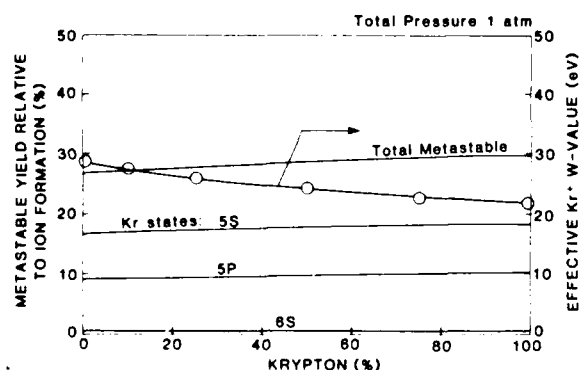

Figure 4. Plots of the effective W-values for the Kr ion and yields of Kr metastables relative to the Kr ion formation in Ar/Kr mixtures as a function of Kr.

Multiplexed Short Pulse Amplification

This last section of the paper discusses calculations related to short pulse amplification in e-beam pumped KrF amplifiers. Figure 5 is a schematic comparison of the transient gain dynamics of a cw amplifier, which corresponds to the usual concatenated multiplexed amplifier, and the gain dynamics of a multiplexed short pulse amplifier with intervening time periods between pulses. With cw amplification, the gain is depleted and kept constant during the energy extraction. Hence, the number of beams required for this scheme is simply calculated by dividing the pumping pulse length by the input laser pulse length. The KrF laser medium is not an energy storage one; the lifetime of KrF* is typically 3 to 5 ns. Therefore, if the input laser pulses to the amplifier are arranged in a series of short pulses with an appropriate time interval between the pulses, the gain medium is repumped during the interval, and the following short pulse can see the highly recovered gain and extract the extra energy stored during the interval. In this scheme, the number of the beams, N_{beams}, needed is calculated using the following equation.

$$N_{beams} = \frac{(\text{pumping pulse length})}{(\text{interval between pulses}) + (\text{input pulse length})} \qquad [1]$$

449

The gain recovery time is defined by the balance between the pumping and the deactivation lifetime of KrF^*. The gain depletion time, $\tau_{depletion}$, which corresponds to the time that the input pulse can extract the extra energy, is obtained by,

$$\tau_{depletion} = \frac{\tau_D}{1 + \phi/\phi_s} \qquad [2]$$

where τ_D is the deactivation lifetime of KrF^*, ϕ is the input beam intensity, and ϕ_s is the saturation intensity. The pulse length required for laser fusion is comparable to the deactivation lifetime of KrF^*; this means the transient dynamics of the KrF^* medium can be utilized to reduce the number of optics and laser beams.
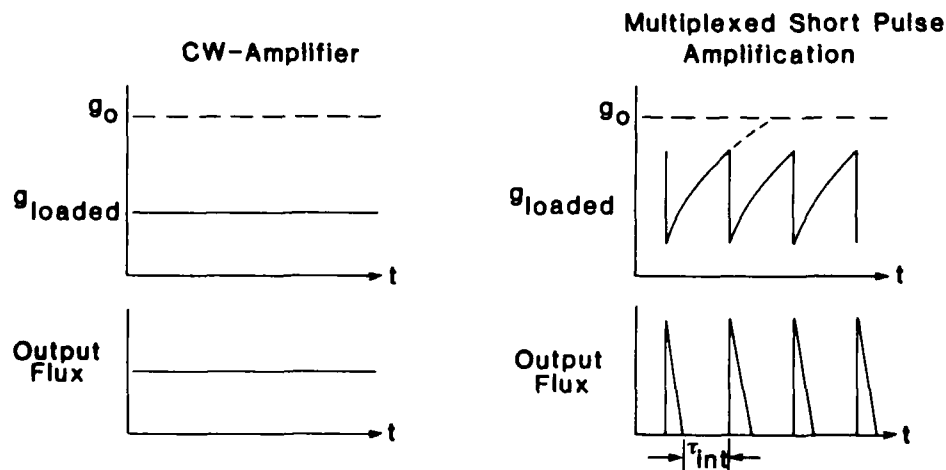

Figure 5.   Schematics of the transient gain dynamics of a cw amplifier and a multiplexed short pulse amplifier with intervening time periods between pulses.

Model calculations are performed and compared with the results of multiplexed short pulse experiments reported by Shaw et al.[5] The code[11] used for this calculation contains the full KrF kinetics, including vibrational relaxation and $KrF^*(B)/(C)$ mixing, but not a detailed secondary electron distribution calculation; however, such a calculation is not necessary when evaluating the performance of this novel amplification scheme. Time-dependent ASE calculations are also available from the model. The model results show that a series of 5-ns pulses, with a 7-ns interval between the pulses, can obtain an energy gain of ≈1.7 times larger than that obtained by a series of 12-ns pulses without time intervals. A peak input intensity of 0.1 MW/cm^2 is assumed. This is in good agreement with the experimental data.

Next analyzed is the amplification scheme being considered for the Large Aperture Module (LAM) KrF amplifier of the Aurora system at Los Alamos National Laboratory (LANL). The gain length is 2 m with 20 cm unpumped regions at the ends, the excitation rate is 240 kW/cm^3, and the laser mixture is 665 torr Kr/F_2. The input pulses to the LAM are amplified by a double pass arrangement. For the case when the two-way propagation time of the laser pulse in the amplifier is longer than the pulse width, the gain depletion caused by the forward and backward pulses has to be properly distributed in the amplifier model to account for depleted regions of gas in the amplifier. The gain recovery time is dependent on location within the amplifier because when and where the pulses pass through a region of gas depends on the pulse length and interpulse time interval. The net effect is that the recovery time is generally shorter than the interval between the pulses.

Figure 6 shows a plot of the extraction efficiency and energy gain, with respect to cw amplification, as a function of the time interval between pulses. For this case, the pulse width of the input pulse is 5 ns. In these calculations, ASE effects have been neglected. The effects of ASE are calculated separately and are given later. The extraction efficiency decreases with increasing time interval. At a 5 ns interval, the reduction of the efficiency is 20%. However, with a 5 ns interval, the number of beams needed for multiplexing is 50% of that needed for the normal concatenated multiplexed system, and the energy gain is three times higher.
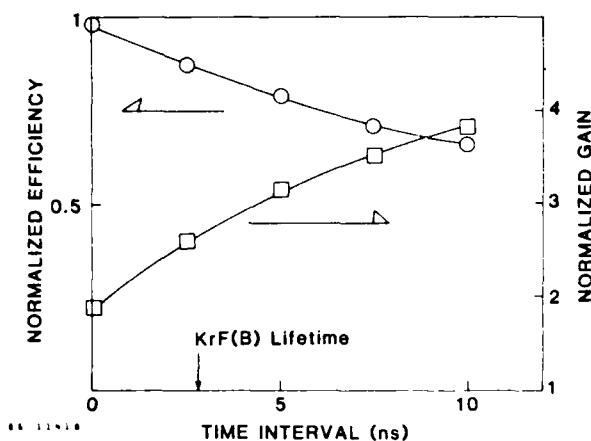
Figure 6. Plots of extraction efficiency and energy gain for multiplexed short pulse amplification relative to cw amplification. The pulse width of the input laser is 5 ns.

Figure 7 shows the effects of ASE on the extraction efficiency. In these calculations, the gain length is shorten to 40 cm to conserve on computation time. However, the gain-length product is the same as the 2-m
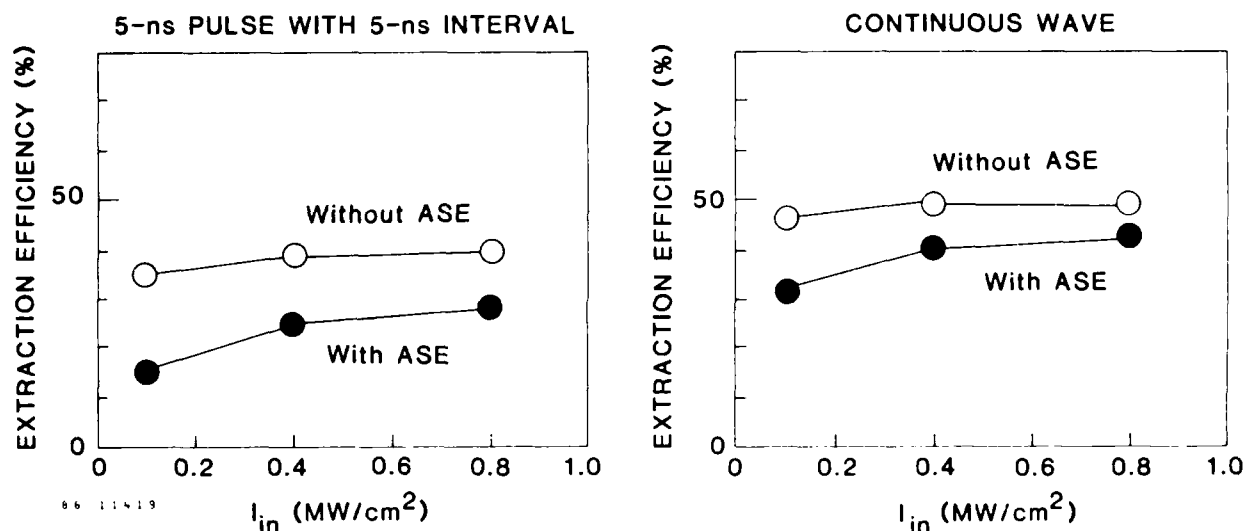

Figure 7. Decrease of extraction efficiency for multiplexed short pulse amplification and cw amplification due to the effects of ASE.

device. Since the propagation time in the 40 cm gain length is shorter than the input pulse width of 5 ns, the gain recovery time is longer than for a 2-m gain length, even with the same input pulse width and interval. Therefore, Fig. 7 represents a worse case example of the affects of ASE build-up. The ASE significantly degrades the extraction efficiency for both cw and short pulse amplifications. The percentage of degradation is about the same if a higher input intensity is assumed during short pulse amplification.

Conclusion

The results of secondary electron density measurements and e-beam source calculations reveal that the energy distribution of the secondary electrons in e-beam pumped laser gases is not Maxwellian. Detailed Boltzmann calculations for the low energy electron distribution and detailed calculations of the e-beam source for the high energy distribution are essential in order to obtain the correct rate constants for electron reactions. These calculations are especially important when determining the dissociative attachment rate constant for F_2 and predicting the number density of the secondary electrons.

The transient dynamics of the KrF^* gain medium permit a novel multiplex short pulse amplification scheme to be used, which reduces the number of optics and laser beams needed. Model predictions agree well with the

experimental results, and demonstrate higher energy gain than the usual concatenated multiplexing schemes. The extraction efficiency, during the condition that reduces the number of beams by 50%, is approximately 30% lower than the usual multiplexing scheme. This multiplexed short pulse amplification scheme is applicable even for the amplification of picosecond short pulses.

Acknowledgments

References

1. L.A. Rosocha, P.S. Bowling, M.J. Burrows, M. Kang, J. Hanlon, J. Mcleod, and G.W. York, Jr., Lasers and Particle Beams, 4, 55 (1986).

2. W.D. Kimura, D.R. Guyer, S.E. Moody, J.F. Seamans, and D.H. Ford, "Electron Density Measurements in Electron-Beam Pumped XeF and KrF Laser Mixtures," to be published in Applied Physics Letters, Jan. 12, 1987.

3. W.D. Kimura, D.R. Guyer, S.E. Moody, J.F. Seamans, and D.H. Ford, Appl. Phys. Lett., 49, 1569 (1986).

4. E.T. Salesky and W.D. Kimura, "Model Comparisons of Electron Density Measurements in KrF, XeF, and XeCl," 39th Gaseous Electronics Conference, Madison, WI, October 7-10, 1986, Paper N-2.

5. M.J. Shaw, I.N. Ross, F. Kannari, E.M. Hodgson, J. Paratanen, E. Turch, and F. O'Neill, Conference on Lasers and Electro-Optics (CLEO), June 9-13, 1986, San Francisco, CA, Paper ThF5.

6. D.W. Trainer and J.H. Jacob, Appl. Phys. Lett., 37, 675 (1980).

7. D. Lorents and R.E. Olson, "Excimer Formation and Decay Processes", Semi-Annual Report No.1, Stanford Research Institute, 1972, (unpublished).

8. D.C. Lorents, Physica, 82C, 19 (1976).

9. C.J. Elliot and A.E. Greene, J. Appl. Phys., 47, 2946 (1976).

10. Z. Rozenberg, M. Lando, and M. Rokni, "Direct Measurement of the Electron Density in Electron Beam Irradiated Ar/F_2 Gas Mixtures by Time Resolved Interferometry," Annual Conference of the Israeli Physical Society, April 20, 1986, Weitzman Institute, Rohovot, Israel.

11. F. Kannari, M. Obara, and T. Fujioka, J. Appl. Phys., 57, 4309 (1985).

HCl BURNUP AND ELECTRON DENSITIES IN E-BEAM PUMPED XeCl

D. R. Guyer, W. D. Kimura, and S. E. Moody

Spectra Technology, Inc.
2755 Northup Way
Bellevue, Washington 98004

Abstract

Presented are the results of electron density and HCl depletion measurements in electron-beam excited XeCl laser mixtures. The results are used to infer the importance of different kinetic processes.

Introduction

There is a body of experimental evidence suggesting that the achievable energy density in e-beam pumped XeCl lasers is limited by cumulative kinetic processes. Several laboratories have observed limiting efficiencies of the laser output at a threshold of ≈5 J/ℓ.[1-3] There is currently no consensus in the field concerning the mechanisms causing this effect. Interpretation of these observations is difficult since there is little experimental data on the concentration changes of key species during e-beam excitation.

As part of a continuing program to characterize and understand the reaction kinetics occurring in these systems, we have performed measurements to determine the time-dependent electron density and extent of halogen consumption in e-beam pumped XeCl. This paper reports the first measurements of HCl consumption in e-beam pumped XeCl laser mixtures under non-lasing conditions. The results of the electron density measurements have also been reported elsewhere.[4,5]

Experimental Results and Discussion

The electron beam source used in both studies is a carbon felt, cold cathode source operating at ≈300 kV and delivers >10 A/cm² at the foil. To better characterize the gain length in the gas mix, the e-beam was baffled down prior to the foil with metal plates. Power deposition in the gas is ≈180 kW/cm³ and is measured using a pressure rise technique.[6] For all gas mixtures presented in this study, the halogen donor is HCl, the diluent is neon, and the xenon concentration is 1.5%. The total gas pressure is 3000 torr and the initial temperature 300 K.

Electron Densities

The experimental setup used to determine electron densities is shown schematically in Fig. 1. The gas chamber of the Tahoma laser system[1] is placed in one arm of a 10.6 μm quadrature interferometer.[7] The laser mirrors are removed and the fused silica windows replaced with BaF_2. The CO_2 probe laser passes ≈3 cm from the foil, centered on the nominal lasing axis. As the index of refraction of the plasma is proportional to electron number density, the measured fringe shifts during the pulse directly yield the temporal changes in the electron density.

Figure 2 shows the temporal evolution of electron density for a variety of initial HCl concentrations. The dashed line at the bottom of the figure depicts a normalized typical-current waveform. During the first 50 nsec of the pulse, the electron density rises sharply then gradually decreases. Since the dissociative attachment rate constants for HCl increase dramatically with vibrational excitation,[8] this behavior can be attributed to the production of vibrationally-excited HCl during the pumping process.
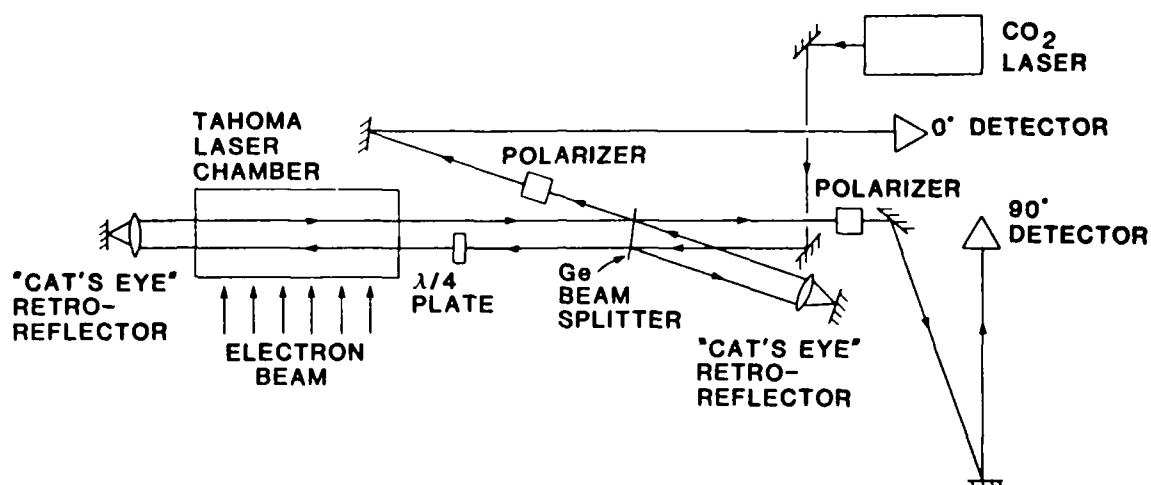
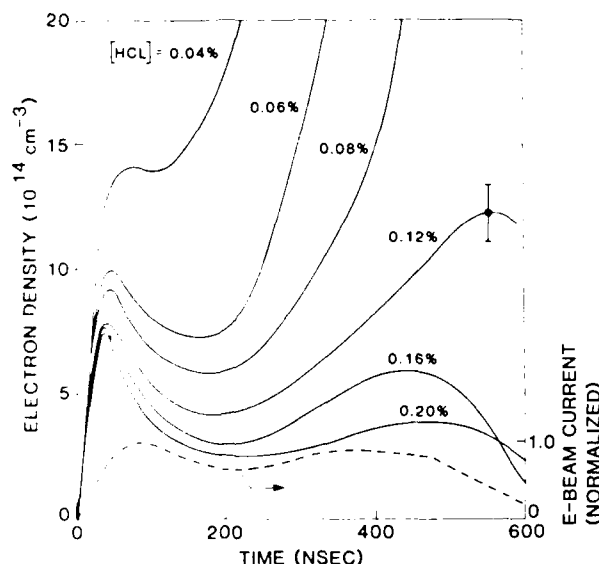Figure 1. Schematic of the electron density measurement system.

Figure 2. Electron densities of XeCl mixtures for various initial HCl concentrations. The dashed curve is a normalized trace of a typical electron beam current waveform. Data points are not shown; however, a representative error bar is shown.

This initial peak in electron density is also observed in model predictions for e-beam discharges under these conditions.[9,10] The surprising result is the magnitude of the electron density, which is 2-4 times greater than the model predictions. Peak laser performance on Tahoma, for this pulse duration, is obtained with HCl concentrations of ≈0.1%. The reason leaner mixtures do not perform as well is evident from the electron density results. At lower HCl concentrations, the electron density is found to increase rapidly at late times during the pulse, implying that the HCl fuel has been exhausted. Halogen burnup at low HCl concentrations is also evident in the XeCl* sidelight fluorescence shown in Fig. 3.

HCl Depletion

The experimental setup is schematically represented in Fig. 4. HCl(v,J) densities are measured directly by infrared absorption on the first vibrational overtone of v"=0,1, and 2. All measurements were made on the P(3) rotational transition and rotational
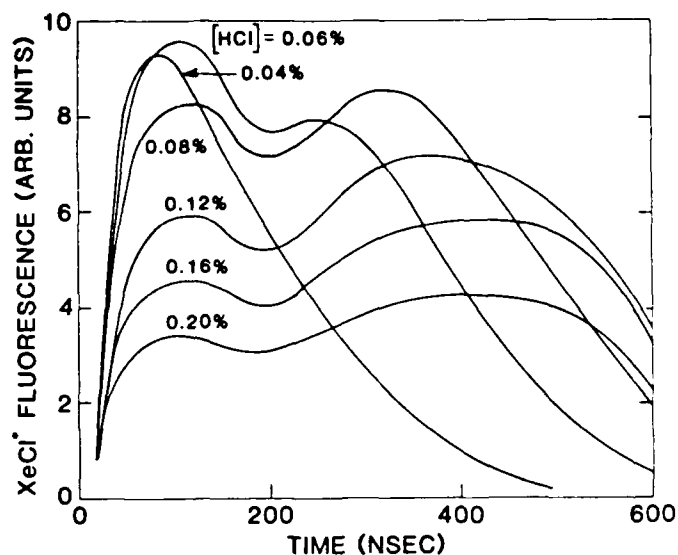
Figure 3. XeCl sidelight fluorescence waveforms for the same mixtures shown in Fig. 2.
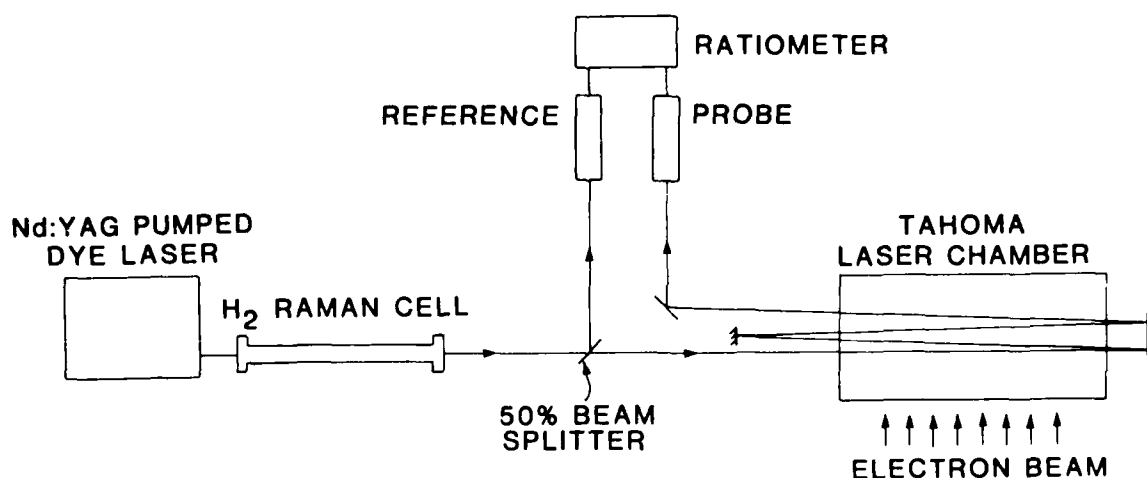
Figure 4. Schematic of the experimental set up for the halogen depletion studies.

equilibration at a final gas temperature of ≈400 K is assumed. To generate tunable light around 1.8 μm, the output of a Nd:YAG pumped dye laser was Raman-shifted in a high pressure H_2 cell. The desired Stokes component was isolated and directed through the nominal active zone of the Tahoma laser chamber. A portion of the probe beam was split off prior to the chamber for normalization purposes. The transmitted power was measured with a pyroelectric detector and ratioed to the reference power to yield the relative amount of absorption.

From measurements with static gas fills of known HCl concentrations, a significant deviation from a simple exponential absorption was observed. Figure 5 shows the measured HCl number density as calculated assuming an exponential absorption and using published overtone absorption cross sections.[11] This behavior was reproducible throughout the measurements and is attributed to saturation effects. A polynomial fit to these data points was made and used to correct the measurements taken during e-beam excitation.

The presence of a strong absorption during the e-beam pulse prevented the time-dependent loss rate of HCl from being determined. This absorption is structureless within our resolution (≈0.3 cm^{-1}) and was found to be strongest in the absence of HCl. This

591

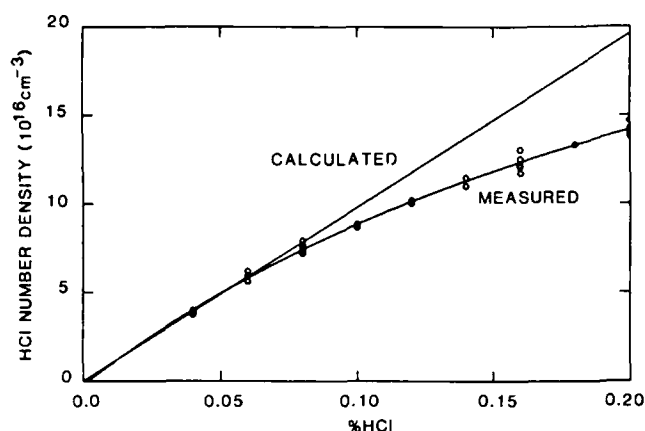Figure 5. Measured HCl number densities as determined assuming an exponential absorption. The staight line shows the expected behavior and the curve is a polynomial fit to the data points.

signal decayed quite rapidly after termination of the e-beam, allowing the residual HCl density to be measured 2 μsec after the excitation pulse. The identity of this absorbing species could not be accurately determined, but the lack of spectral structure, the strength of the absorption, and the short lifetime suggest an assignment of Xe_2^+.

Figure 6 gives the results of the HCl(v=0) depletion measurements. For initial concentrations below ≈0.1% HCl the data show nearly complete removal of the HCl. This is consistent with the electron density measurements; for these lower HCl concentrations, the HCl is depleted at some point during the pulse and this absence of an attacher allows the electron density to increase. At higher initial HCl concentrations, the fractional burnup does not level off but continues to increase. At the highest initial concentrations studied (0.20% HCl), the fractional loss of HCl(v=0) is found to be 61±8%. Higher vibrational states were observed only at the higher HCl densities. At 0.20% initial HCl, the population in HCl(v=1) shows a maximum of 2.4% of the HCl added. HCl(v=2) was never observed, allowing an upper limit of 0.2% to be determined from our noise level for this transition.
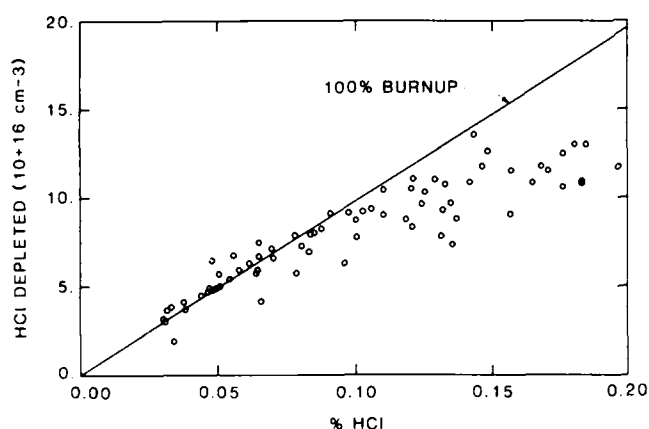
Figure 6. Measured HCl(v=0) loss after firing the electron beam for various initial HCl concentrations. The straight line shows the expected behavior for 100% consumption of the HCl present.

Quantitatively, these results represent a __minimum__ cumulative loss of HCl. Since the probe pulse is delayed by 2 μsec, some degree of HCl regeneration will have occurred via three-body recombination and associative detachment reactions. The residual populations in HCl(v=1,2) also must be regarded as a minimum since vibrational relaxation by superelastic collisions with electrons is expected to be significant.

Concluding Remarks

The kinetic processes, involved in e-beam pumped XeCl lasers, represent a rich chemistry that at present is still incompletely understood. The data presented here show

both a significantly higher electron density and a greater HCl loss than expected from model predictions for this system. These results suggest that electron associative detachment cannot, by itself, account for the depletion of HCl and that other loss channels must be considered. A likely candidate is direct electron impact dissociation of HCl leading to neutral atomic products. Further analysis of the data is currently in progress.

Acknowledgement

References

1. S.E. Moody, L.A. Levin, R.E. Center, J.J. Ewing, and E.L. Klosterman, IEEE J. Quant. Elec., QE-17, 1856 (1981).

2. Kenneth Tang, Western Research Corp., private communication.

3. L. Litzenberger, R. Slater, D.W. Trainor, Internatonal Conference on Lasers '85, December 2-6, 1985, Las Vegas, NV, Paper HK.7.

4. W.D. Kimura, D.R. Guyer, S.E. Moody, J.F. Seamans, and D.H. Ford, Appl. Phys. Lett., 49, 1569 (1986).

5. W.D. Kimura, D.R. Guyer, S.E. Moody, J.F. Seamans, and D.H. Ford, to be published in Appl. Phys. Lett., Jan. 12, 1987.

6. E.T. Salesky and W.D. Kimura, IEEE J. Quan. Elec., QE-21, 1761-1765 (1985).

7. C.J. Buchenauer and A.R. Jacobson, Rev. Sci. Instrum., 48,769 (1977).

8. J.N. Bardsley and J. M. Wadehra, J. Chem. Phys., 78,7227 (1983).

9. Fumihiko Kannari, Spectra Technology Inc., private communication.

10. E.T. Salesky and W.D. Kimura, 39th Gaseous Electronics Conference, Madison, WI, October 7-10, 1986, Paper N-2.

11. D. Oba, B.S. Agrawalla and D.W. Setser, J. Quant. Spectrosc. Radiat. Transfer, 34,283 (1985).

Xenon excited state density measurements in electron beam pumped XeCl laser mixtures

F. Kannari, W. D. Kimura, J. F. Seamans, and Dean R. Guyer

Spectra Technology, Inc., 2755 Northup Way, Bellevue, Washington 98004-1495

Time-dependent density measurements of the lowest xenon excited states ($5p^5 6s$) in electron beam (e-beam) pumped XeCl laser mixtures (nonlasing) are performed using pulsed hook interferometry. The e-beam pulse length is $\approx 0.45 \mu s$ (full width at half-maximum) with an average excitation rate of ≈ 250 kW/cm^3. Density differences (ΔN^*) of transitions at 823.2 nm ($6s[3/2]_2^0-6p[3/2]_2$), 828.0 nm ($6s[3/2]_1^0-6p[1/2]_0$), and 840.9 nm ($6s[3/2]_2^0-6p[3/2]_1$) are obtained for various HCl and Xe concentrations. For a 98.3% Ne/1.5% Xe/0.16% HCl mixture at 3000 Torr, ΔN^* (823.2 nm) and ΔN^*(828.0 nm) are relatively constant at $\approx 3 \times 10^{14}$ and $\approx 1.7 \times 10^{14}$ cm^{-3}, respectively. At lower initial HCl concentrations, the ΔN^*(823.2 nm) density starts out similar to the 0.16% HCl case, but tends to increase dramatically during the e-beam pulse. For a 0.04% HCl mixture, a ΔN^*(840.9 nm) density of $\approx 4.5 \times 10^{15}$ cm^{-3} is measured at the end of the e-beam pulse. Preliminary comparisons of the data with a computer model show good agreement for HCl concentrations $\geqslant 0.16\%$, but disagreements at leaner concentrations.

The formation of XeCl ($B\,^2\Sigma^+$) in electron beam (e-beam) pumped lasers has been the topic of considerable debate.[1,2] This letter describes, to our knowledge, the first time-dependent measurements of xenon excited state (Xe*) densities in e-beam pumped XeCl mixtures (nonlasing). These results together with earlier measurements of the time-dependent electron density[3] and the HCl depletion[4] in XeCl were performed to help improve our understanding and modeling of XeCl formation and laser kinetics.

Excited states of xenon are important for the neutral channel formation of XeCl. The first excited levels of xenon, Xe*($5p^5[^2P_{3/2}^0]6s$), have very small XeCl formation rate constants with vibrational ground-state HCl[5]; however, the rate constants increase dramatically with vibrational excitation of HCl.[6]

The Xe* density is measured using hook interferometry[7] in which the e-beam pumped laser medium is placed in one branch of a laser interferometer (see Fig. 1). An excimer pumped broadband dye laser output passes twice through the gas chamber ≈ 3 cm from the foil and centered around the nominal lasing axis. The output of the interferometer is directed into a spectrometer whose output is an interference pattern that contains "hooks" caused by the anomalous dispersion around atomic absorption lines. Interference patterns are detected by a vidicon camera and recorded on videotape for later analysis. The e-beam excitation rate is ≈ 250 kW/cm^3, which is higher than during the earlier electron density measurements.[3]

The wavelength separation Δ between the hooks in the interference pattern, centered around a transition wavelength λ_{ij} (where i and j are the lower and upper levels, respectively), is given by[7,8]

$$\Delta^2 = N_i \left(1 - \frac{g_i N_j}{g_j N_i}\right) \frac{r_0 \lambda_{ij}^3 l f_{ij}}{\pi K}, \tag{1}$$

where N_{ij} are the population densities, g_{ij} are the statistical weights of each level, r_0 is the classical electron radius, l is the length of the medium, f_{ij} is the oscillator strength of the

transition, and K is a constant that can be determined from an undistorted interference pattern. A knowledge of a particular transition oscillator strength allows the population difference, $\Delta N^* = N_i - (g_i/g_j)N_j$, to be determined from the hook spectra.

Hook interferometry offers several advantages. It has a relatively large dynamic range, the results are insensitive to line shape perturbations such as pressure broadening, and complicated geometrical or detector calibrations are unnecessary.

Figure 2 is an energy-level diagram showing the transitions examined during the experiment: 823.2 nm ($6s[3/2]_2^0-6p[3/2]_2$), 828.0 nm ($6s[3/2]_1^0-6p[1/2]_0$), and 840.9 nm ($6s[3/2]_2^0-6p[3/2]_1$). Oscillator strengths for these lines are 0.23, 0.12, and 0.012, respectively.[9] The total optical path of the excited laser medium is 70 cm. The value of K in Eq. (1) is typically $\approx 1.5 \times 10^3$. Thus, on our system a hook separation of 1 nm at 823.2 nm corresponds to a ΔN^* density of 7×10^{13} cm^{-3}.

A typical hook interference pattern is shown in Fig. 3. As can be seen, not all the transitions are well separated from one another. In our case, two relatively strong transitions are
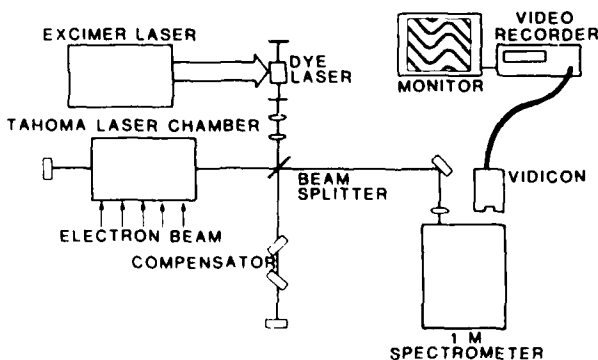

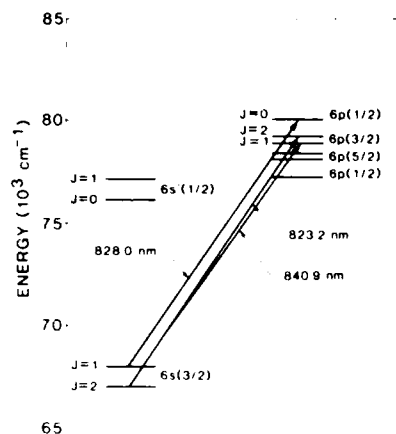FIG. 1. Schematic of xenon excited state density measurement system.

FIG. 2. Energy-level diagram of xenon showing transitions examined.

FIG. 4. Time-dependent ΔN^* densities of a 3000 Torr mixture of 98.3% Ne/1.5% Xe/0.16% HCl at 294 K. Closed and open circles correspond to ΔN^* (823.2 nm) and ΔN^* (828.0 nm), respectively. The dashed curve is a normalized trace of the e-beam current waveform.

observed at 826.6 and 822.1 nm near the 828.0 and 823.2 nm transitions. The transition at 826.6 nm corresponds to Xe $(6s'[1/2]_1^0 - 6p'[1/2]_1)$. The transition at 822.1 nm (not shown in Fig. 3) has not been identified. These lines distort the hook profiles and position on the short wavelength side of the 828.0 and 823.2 nm transitions, while the effects on the long wavelength side of the transitions are negligible.

For an isolated transition, the hook separation is symmetric about the transition wavelength. The quadratic Stark effect can displace the hooks towards long wavelengths,[9] but because the electron density is relatively low[4] ($\approx 10^{15}$ cm^{-3}), this effect can be ignored. Therefore, during analysis of the data, it is assumed the total hook separation can be calculated by doubling the distance between the hook on the long wavelength side and line center (see Fig. 3).

In typical laser kinetics models, Xe** is a generic highly excited state representing Xe($6p$) states above Xe($6s$). Calculations indicate that the total population of Xe** is significant. Since cross sections for stepwise excitation of Xe* are estimated to be large,[10] the two-body relaxation rates of Xe** by neutral molecules are small,[11] and the electron density is appreciable,[4] thermalization among these levels at near the electron temperature of ≈ 1.5 eV (Ref. 12) is expected. Within this assumption, the upper state populations of the probed transitions are estimated to be $\approx 10-36\%$ of the lower state. Measurements of Xe($6s'[1/2]_1$) in XeCl,

XeF, and Ne/Xe mixtures also suggest significant upper state densities.[13] Due to the uncertainty in the upper state population, all measurements herein are presented as density differences (ΔN^*) rather than level densities.

Figure 4 shows typical experimental results obtained at the 828.0 and 823.2 nm transitions, for an initial HCl concentration of 0.16%. The estimated measurement uncertainty associated with all the data points presented in this letter is $\pm 10\%$. As can be seen, the density differences are relatively constant during the e-beam pumping.

Xenon excited states are produced primarily by recombination reactions of dimer ions (Xe$_2^+$, NeXe$^+$) rather than direct excitation of ground-state Xe by electrons. Cl from HCl controls the Xe* population by intercepting Xe$^+$, the precursor to the dimer ions, to form XeCl. Hence, as long as dissociative attachment is the dominant electron loss process, the Xe* density decreases with increasing initial HCl concentration. In fact, experimental results for 0.32% HCl (not shown) are $\approx 47\%$ of ΔN^* at 0.16% HCl. However, Figs. 5 and 6 show time-dependent ΔN^* densities for rela-

828.0 nm   826.6 nm   823.2 nm

FIG. 3. Typical hook interference pattern. Δ is the total hook separation.

FIG. 5. Time-dependent ΔN^* densities for an initial HCl concentration of 0.08%. The other gas parameters and symbols are the same as in Fig. 4. Closed triangles correspond to ΔN^* (840.9 nm).
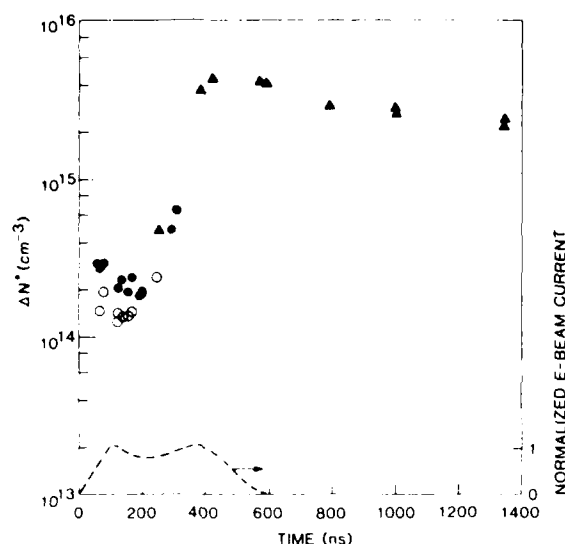
FIG. 6. Time-dependent ΔN^* densities for an initial HCl concentration of 0.04%. The other gas parameters and symbols are the same as in Figs. 4 and 5.

Preliminary comparisons with a computer model[14] yield good agreement with the data for initial HCl concentrations $\geq 0.16\%$. At leaner concentrations the model does not predict the rapid increase in Xe* density seen during the pulse. T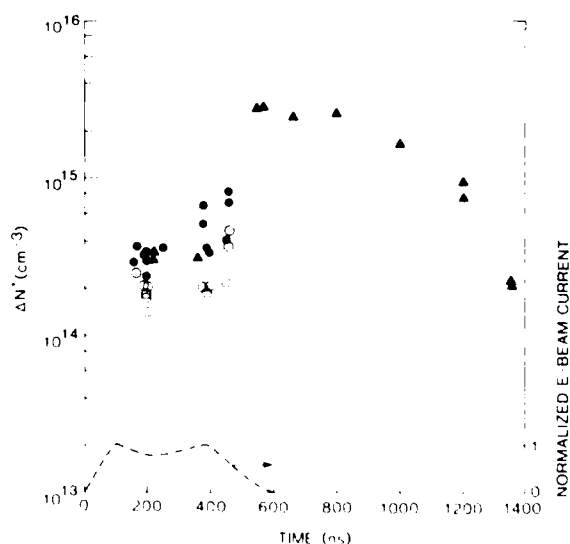his may be related to the model's underprediction of HCl depletion.[4] The model also does not predict the long Xe* density lifetime observed after the end of the e-beam pulse for lean HCl mixtures. This lifetime appears correlated with the electron density,[3] and is sensitive to the NeXe* and NeXe[+] formation rates, which may mean that an improved estimation of these rates[15] is needed. Hence, the Xe* density measurements demonstrate that our understanding of Xe* formation is good except under conditions when a significant amount of halogen is lost. Additional discussion regarding the implications of these measurements, as well as Xe* and Xe** measurements in XeF, will be presented in another paper.[13]

The authors wish to acknowledge Dr. J. J. Ewing and Dr. S. E. Moody for their helpful discussions. This work was supported by the Office of Naval Research, contract No. N00014-85-C-0843.

tively low initial HCl concentrations of 0.08 and 0.04%, respectively. In these figures, data for ΔN^* (840.9 nm) are also shown, particularly for densities $> 10^{15}$ cm^{-3} where broadening of the transition linewidth obscures the hooks for the 823.2 and 828.0 nm lines. Two interesting Xe* density behaviors are observed. First, although higher Xe* densities are expected for lower HCl concentrations, densities measured during the first 200 ns are nearly the same as given in Fig. 4. Second, at low HCl concentrations, the ΔN^* density dramatically increases at a certain point during the e-beam pulse. As the initial HCl concentration is reduced, the ΔN^* density begins to increase at earlier times. A peak ΔN^* (840.9 nm) density of 4.5×10^{15} cm^{-3} is measured for the 0.04% HCl mixture. The abrupt increase in ΔN^* densities is likely caused by exhaustion of HCl during the pump pulse, which leads to an abrupt increase in the secondary electron density[3] and results in an increase in electron-dimer ion recombination.

Measurements also show that the Xe* density increases with increasing initial xenon concentration. At 150 ns into the e-beam pulse, ΔN^* (823.2 nm) densities of 2.0×10^{14} and 4.5×10^{14} cm^{-3} are obtained for 0.5% and 3.0% Xe, respectively, with HCl fixed at 0.16%.

[1] D. L. Huestis, 39th Annual Gaseous Electronics Conference, Madison, WI, Oct. 7-10, 1986, paper N-4 (unpublished).

[2] Workshop on XeCl Kinetics, SRI International, Menlo Park, CA, Dec. 19, 1985, SRI Report No. MP 86-044.

[3] W. D. Kimura, D. R. Guyer, S. E. Moody, J. F. Seamans, and D. H. Ford, Appl. Phys. Lett. 49, 1569 (1986).

[4] D. R. Guyer, W. D. Kimura, and S. E. Moody, in Proceedings of the International Conference on Lasers '86, Orlando, FL, Nov. 3-7, 1986, edited by R. W. McMillan (STS, McLean, 1987), p. 589.

[5] J. K. Ku and D. W. Setser, Appl. Phys. Lett. 48, 689 (1986).

[6] R. S. F. Chang, J. Chem. Phys. 76, 2943 (1982).

[7] W. C. Marlow, Appl. Opt. 6, 1715 (1967).

[8] S. A. Kopff and G. Breit, Rev. Mod. Phys. 4, 471 (1932).

[9] V. R. Lazovskaya and G. K. Tumakaev, Sov. Phys. Tech. Phys. 24, 328 (1979).

[10] H. A. Hyman, Phys. Rev. A 18, 441 (1978).

[11] G. Inoue, J. K. Ku, and D. W. Setser, J. Chem. Phys. 81, 5760 (1984).

[12] F. Kannari, W. D. Kimura, and E. T. Salesky, Conference on Lasers and Electro-Optics (CLEO), Baltimore, MD, Apr. 26-May 1, 1987, paper WR4 (unpublished).

[13] F. Kannari, W. D. Kimura, J. F. Seamans, and D. R. Guyer (unpublished).

[14] F. Kannari, A. Suda, M. Obara, and T. Fujioka, IEEE J. Quantum Electron. QE-19, 1587 (1983).

[15] L. A. Levin, S. E. Moody, E. L. Klosterman, R. E. Center, and J. J. Ewing, IEEE J. Quantum Electron. QE-17, 2282 (1981).

Diagnostic techniques for studying excimer laser kinetics

W.D. Kimura, F. Kannari, J.F. Seamans, and D.R. Guyer

Spectra Technology, Inc.
2755 Northup Way, Bellevue, Washington 98004-1495

ABSTRACT

Several novel diagnostic techniques have been used to analyze the laser kinetics occurring in electron-beam pumped excimer lasers. Described are a quadrature interferometer for measuring time-dependent electron densities, an overtone absorption technique for measuring the HCl concentration, a broadband dye laser system for measuring the spectrally resolved gain in XeF, and a hook interferometer for measuring time-dependent excited state densities. These techniques can also be applied to other non-excimer lasers.

1. INTRODUCTION

Further advancement of excimer laser technology relies on the further advancement of our understanding of the laser kinetics. Models of the laser performance, which are used for example to scale these devices to large sizes, are only as good as our understanding. Our confidence in these models is only as good as the data available to validate the models. Hence, there is a need to apply appropriate diagnostic measurements on these lasers to reveal fundamental characteristics of the laser medium.

Usual diagnostics that measure parameters such as the laser output energy, efficiency, pulse shape, and lasing spectrum, only provide macroscopic information regarding the laser medium characteristics. The data cannot easily reveal details about the gas kinetics because they represent essentially the net result of many complex processes occurring simultaneously. Gain, absorption, and sidelight fluorescence measurements reveal more details, but they are still the net affect of a complicated molecular chemistry occurring within the laser plasma. Therefore, to understand the kinetics on a fundamental level, it is necessary to measure specific quantities on a molecular level. It is at this molecular level that the kinetics models are based, and it is at this level that critical data is lacking.

This paper discusses diagnostic techniques used at Spectra Technology, Inc. (STI) on an electron-beam (e-beam) pumped excimer laser[1] to measure various characteristics of the laser active medium. The first diagnostic is an infrared quadrature interferometer to measure the electron density in XeCl,[2] XeF,[3] and KrF;[3] the second is a Raman-shifted Nd:YAG pumped dye laser to measure the HCl depletion in XeCl;[4] the third is an excimer pumped broadband dye laser system to measure spectrally resolved small signal gain in XeF;[5] and the fourth is a hook interferometer to determine the Xe excited state densities in XeCl[6,7] and XeF.[7]

2. DESCRIPTION OF E-BEAM PUMPED LASER

The laser (Tahoma) during all these measurements has been used extensively in the past for lasing experiments on XeCl,[1] XeF,[8] KrF,[9] and other excimers. Details of the laser system can be found in the aforementioned references. However, all the measurements described in this paper are performed under nonlasing conditions (that is the normal laser mirrors are removed). The measurements can also be performed under lasing conditions, with the various probe laser beams introduced off-axis to the active volume, and, indeed, this would be very useful to perform at some future time.

The nominal gain length is 70 cm, but it can be shorten by blocking the ends of the e-beam with baffles. This ability to shorten the gain length and thereby tune the sensitivity

of the measurement is important because occasionally the changes induced on the probe laser beams can be beyond the dynamic range of the detectors.

The e-beam pulse length is variable from ≈100 ns to 1 μs. Generally, the time-dependence of the quantity of interest relative to the e-beam pulse shape is desired. However, rather than perform all measurements at the longest e-beam pulse length, measurements are also done at ≈0.5 μs. This is because the optimum halogen concentration for lasing tends to increase with energy loading (pump rate times e-beam pulse length); however, higher halogen concentration also increases the amount of halogen quenching. Therefore, for a fixed pump rate and halogen concentration, it is necessary to vary the e-beam pulse length in order to investigate other operating regimes of interest.

Timing of the various lasers and detectors used in the diagnostics is controlled by separate digital delay generators triggered by a computer program that primes and fires the laser, and acquires the data. A video frame store unit in the computer system captures the output from the vidicon camera used during some of the experiments, and provides a convenient method for storing data for later analysis.

3. ELECTRON DENSITY MEASUREMENT USING QUADRATURE INTERFEROMETRY

Figure 1 is a schematic of the quadrature interferometer system used to measure the time-dependent electron density.[2,3] The quadrature interferometer[10] uses a single mode, cw CO_2 laser to probe the active volume of the laser chamber positioned in one branch of a Michelson interferometer. Double use of the interferometer central beamsplitter together with a λ/4 plate provide two output beams that are 90° out of phase with one another. The "cat's eye" retro-reflectors permit the incident and reflected beams to be offset from one another, while at the same time not disturbing the polarization.
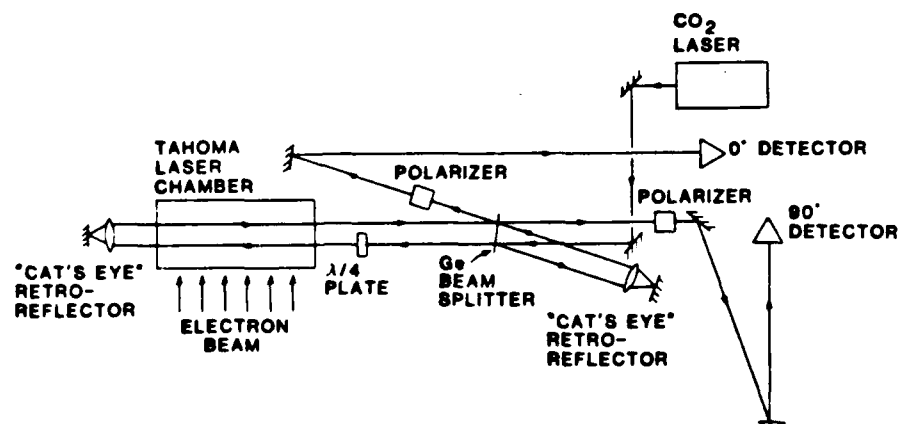
Figure 1. Schematic of quadrature interferometer system for measuring the time-dependent electron density.

Liquid nitrogen-cooled HgCdTe detectors measure the 10.6 μm signals. Due to infrared emission from the laser chamber, the detectors are placed ≈18 m away to eliminate any false signals. (Narrowband filters centered at 10.6 μm would have also solved this problem.)

The electron density is determined by measuring the fringe shifts occurring during the e-beam excitation and calculating the density using the plasma dispersion relationship.[2] For this experiment, because of the fairly high electron density and, therefore, large number of fringe shifts, the e-beam is baffled to 35 cm in length so that the CO_2 laser beam travels through 70 cm of active medium. One fringe shift then corresponds to an electron density of 3×10^{14} cm^{-3}.

An example of the two detector outputs is shown in Fig. 2. Note the rapid fluctuations of the signal during the beginning, indicating a rapid increase of electron density. The signal varies more slowly after ≈100 ns, indicating a more constant density, and then ends

DETECTOR OUTPUT

PHASE

0°

90°

TIME (50 ns/div)
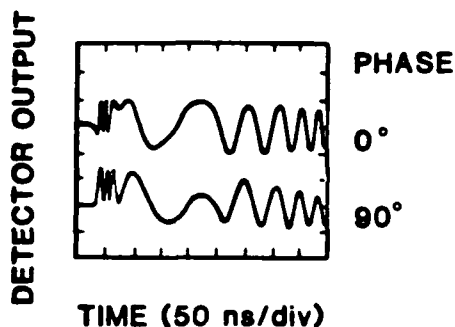
Figure 2. Oscilloscope traces from the HgCdTe detectors. The top trace is 90° out of phase with the bottom one. The gas mixture is 98.4% Ne/1.5% Xe/0.08% HCl at 3000 Torr total pressure and an e-beam deposition rate of ≈180 kW/cm^{-3}.

with a relatively steady variation indicating, in this case, a steady increase of density. Although all the phase information can be ascertained from only one detector, the second detector eliminates the ambiguity that can arise when the first detector signal passes through an extremum. At an extremum, the sign of the phase shift is unknown; however, by examining the other detector, which will be at its maximum differential sensitivity, the direction of the phase shift is known. An example of the electron density results for XeCl are given in Fig. 3.
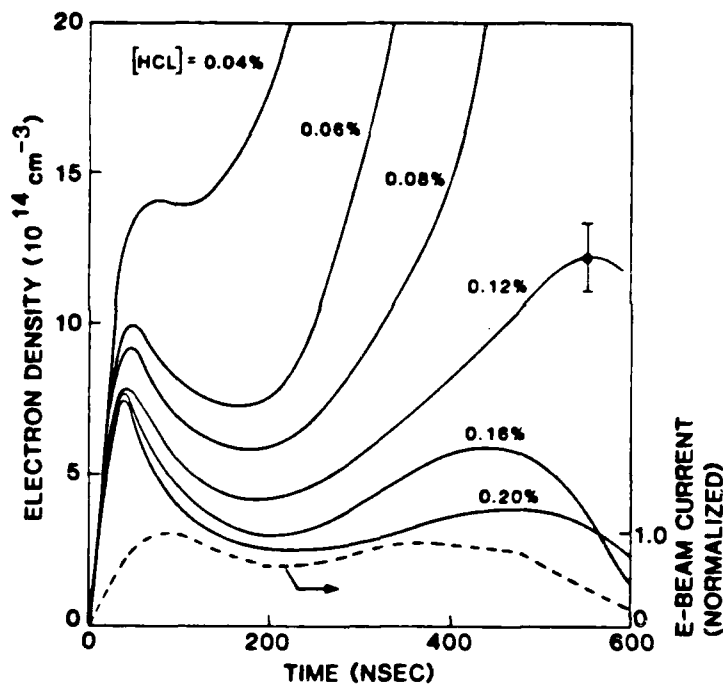

Figure 3. Typical electron densities of XeCl mixtures (1.5% Xe, balance Ne to 3000 Torr) with the e-beam deposition ≈180 kW/cm^{3}. The dashed curve is a normalized trace of a typical electron beam current waveform. Data points are not shown; however, a representative error bar is indicated.

4. HCl DEPLETION MEASUREMENT USING OVERTONE ABSORPTION

Halogen depletion in excimer lasers during the pump pulse is a critical issue. To measure the HCl concentration, the technique chosen is direct absorption measurements on the first vibrational overtone of v"=0, 1, and 2 at ≈1.8 μm.[4] This is because HCl absorbs too strongly on the v'=1 ← v"=0 transition to permit convenient measurement over the length of the active volume. All measurements are made on the P(3) rotational transition and rotational equilibration at a final gas temperature of ≈400 K is assumed.

Figure 4 is schematic of the halogen depletion measurement system. The laser medium is probed by a Nd:YAG pumped dye laser whose output is Raman-shifted to 1.8 μm in a high pressure H$_2$ cell. Ratioing the signals from the reference and probe pyroelectric detectors gives the relative amount of absorption. For these measurements, the gain length is 70 cm.

RATIOMETER

REFERENCE   PROBE

Nd:YAG PUMPED
DYE LASER

H_2 RAMAN CELL

TAHOMA
LASER CHAMBER

50% BEAM
SPLITTER

↑↑↑↑↑↑↑↑
ELECTRON BEAM

Figure 4. Schematic of HCl depletion measurement system using vibrational overtone absorption.

Due to other infrared absorption that occurs during the e-beam pumping (possibly due to Xe_2^+), measurements are obtained ≈2 µs after termination of the e-beam pulse, and indicate the remaining HCl concentration. Hence, direct time-dependent HCl depletion measurements are not possible with this technique; however, by either keeping the e-beam pulse length fixed and varying the initial HCl concentration or keeping the initial HCl concentration fixed and varying the e-beam pulse length, it is possible to indirectly infer the rate of halogen depletion. In our case, the former approach was taken, and the results for HCl(v''=0) are shown in Fig. 5.

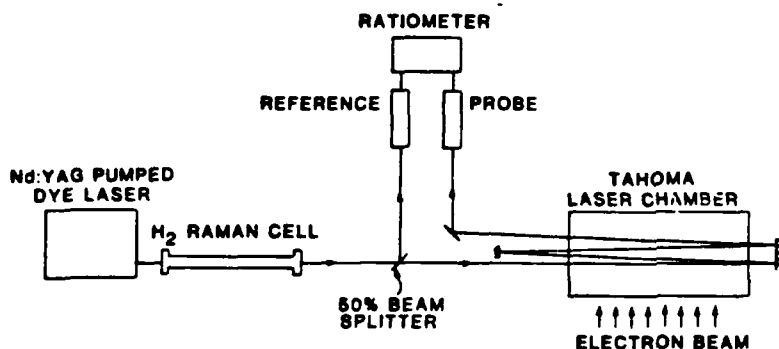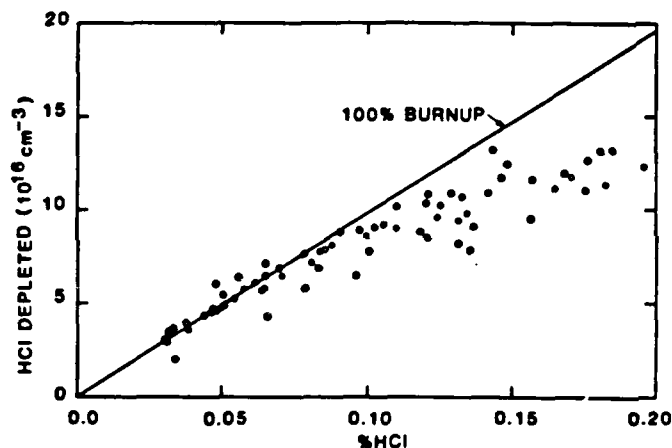**Figure 5.** Measured HCl(v''=0) loss after firing the e-beam for various initial HCl concentrations. Other parameters are the same as in Fig. 3. The straight line indicates 100% consumption of the HCl present.

Since vibrational excitation of HCl to states higher than v''=0 is possible, these higher states were also measured using the overtone absorption technique. Higher vibrational states are only observed at the higher HCl concentrations. For 0.2% HCl, the HCl(v''=1) population is <2.4% of the HCl added; the HCl(v''=2) population is negligible.

5. SINGLE SHOT FULL SPECTRUM GAIN MEASUREMENT IN XeF

An excimer pumped dye laser (TMQ dye), operating broadband (≈50 Å wide) and centered at around 350 nm, is used to obtain the full spectrum, small signal gain of e-beam excited XeF during a single shot. To our knowledge, this is the first time the spectrally resolved gain spectrum has been measured in XeF. Although, as mentioned earlier, gain measurements are not usually simply related to basic gas kinetic quantities, being able to examine the entire gain spectrum does reveal information regarding the degree of vibrational and rotational coupling in the XeF manifold. Such information is particularly important when attempting to understand the narrowband extraction characteristics of XeF.[6]

A schematic of the gain measurement system is shown in Fig. 6. The dye laser output is split into a probe and reference beam. Within the laser chamber, the probe intensity averaged over the entire XeF gain band is <50 kW/cm². The dye laser pulse length is <5 ns; hence, by varying the time delay of the dye laser with respect to the e-beam, the temporal dependence of the gain during the e-beam pumping can be obtained.
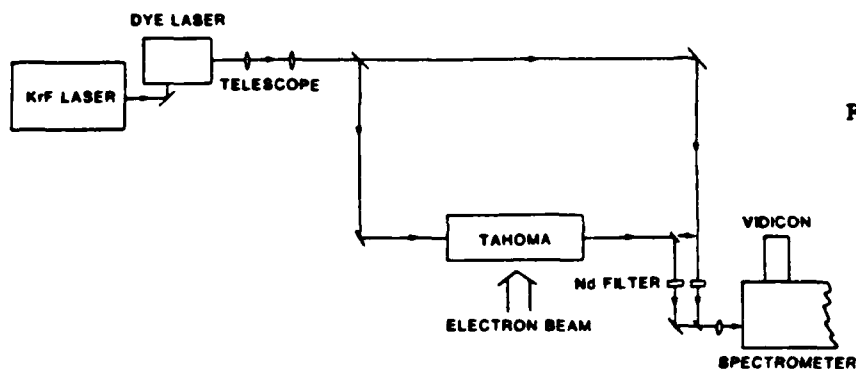
Figure 6. Schematic of gain measurement system for obtaining spectrally resolved gain in XeF.

The probe and reference beams are sent through calibrated neutral density filters and are vertically displaced across the entrance slit to a 1 m spectrometer. Hence, at the output of the spectrometer (used without an exit slit) are two bands of light, one above the other, that correspond to the dye laser spectrum. The probe beam is amplified by the excited XeF medium; taking the ratio of the probe to the reference then yields the gain.

A UV vidicon camera detects both the probe and reference spectra simultaneously. This is shown schematically in Fig. 7. A computer-controlled video frame store unit captures the frame with the spectra and stores the data in computer memory. By aligning the camera with its raster lines oriented along the dispersion direction of the spectra, the raster lines within a band of light can be averaged pixel-to-pixel, thereby improving the signal-to-noise of the data. This method of data collection provides a convenient means to acquire and analyze spectral data.
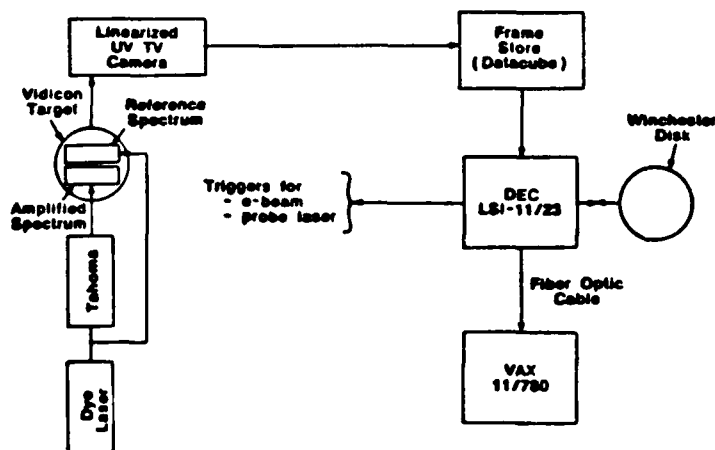
Figure 7. Data acquisition system for collecting output from the gain spectrometer shown in Fig. 6.

A typical example of the small signal gain measured is given in Fig. 8. The two dips in the gain spectrum at 351.52 and 352.05 nm correspond to neon absorption lines[11] and are used to provide an accurate absolute wavelength calibration of the spectra.

6. XENON EXCITED STATE MEASUREMENTS USING HOOK INTERFEROMETRY

Hook interferometry[12] is a method by which excited state population densities can be measured. It has been used on lasers before[13] but, to our knowledge, this is the first time it has been applied to e-beam pumped excimer lasers.[6,7]
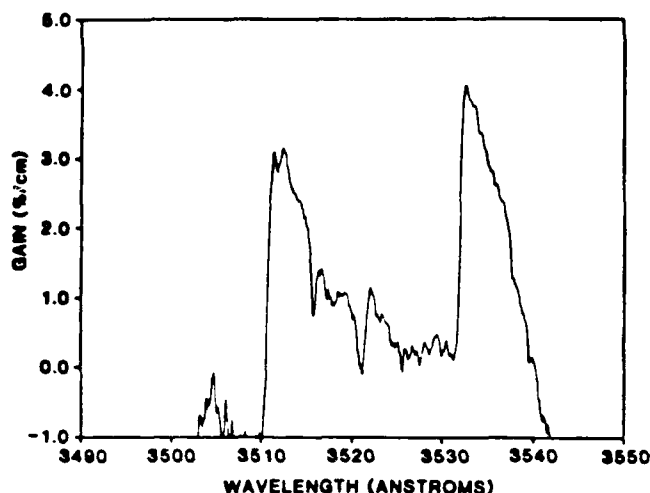
Figure 8. Typical small signal gain spectrum of XeF for an e-beam deposition of ≈ 180 kW/cm^3 and a gas mixture of 99.4% Ne/0.5% Xe/0.1% F$_2$ at 3.5 amagats.

A schematic of the hook interferometer system is shown in Fig. 9. A short pulse, broadband dye laser, centered at ≈ 830 nm, (LDS 821 dye in DMSO + 10% methanol) feeds a Michelson interferometer in which the laser chamber is in one branch. The output from the interferometer is analyzed by a spectrometer whose output is detected by a vidicon camera. Due to anomalous dispersion occurring around an atomic resonance transition, "hooks" form in the interference pattern seen by the camera. The separation of these hooks is directly
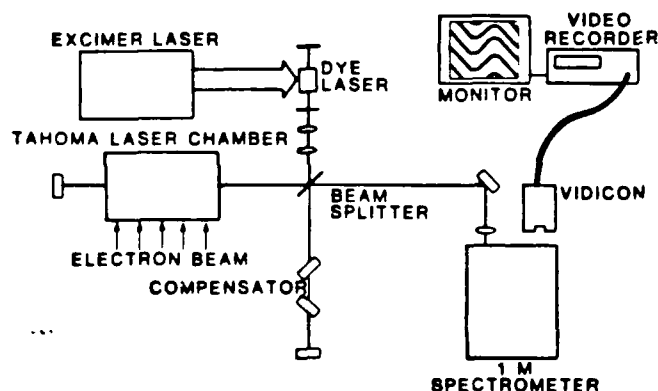
Figure 9. Schematic of hook interferometer system for measuring xenon excited state densities.

proportional to the excited state population difference of the transition. If the transition oscillator strength and the active medium length are known, the absolute value of the excited state population difference can be determined.

An example of the hook spectra obtained during the experiment for XeCl is given in Fig. 10. Visible are the xenon transition lines at 823.2 nm ($6s[3/2]_2^o - 6p[3/2]_2$) and 828.0 nm ($6s[3/2]_1^o - 6p[1/2]_0$). (The line at 826.6 nm corresponds to Xe ($6s'[1/2]_1^o - 6p'[1/2]_1$) and was not examined during this experiment).

828.0 nm   826.6 nm   823.2 nm
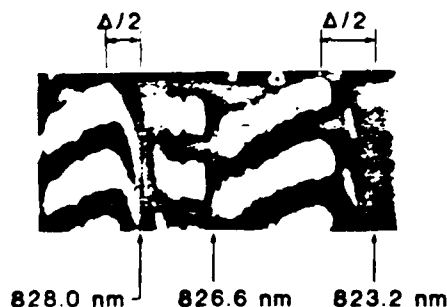
Figure 10. Typical hook spectra obtained from the system shown in Fig. 9. The hook separation is represented by Δ.

Figure 11 shows typical xenon excited state density results for XeCl. This type of information is important because of the role excited state xenon plays in the formation of XeCl. The Xe* density is also affected by the consumption of the halogen gas.

This same technique is applicable to other excimer lasers, such as KrF, where measurements of the krypton excited states densities is possible.
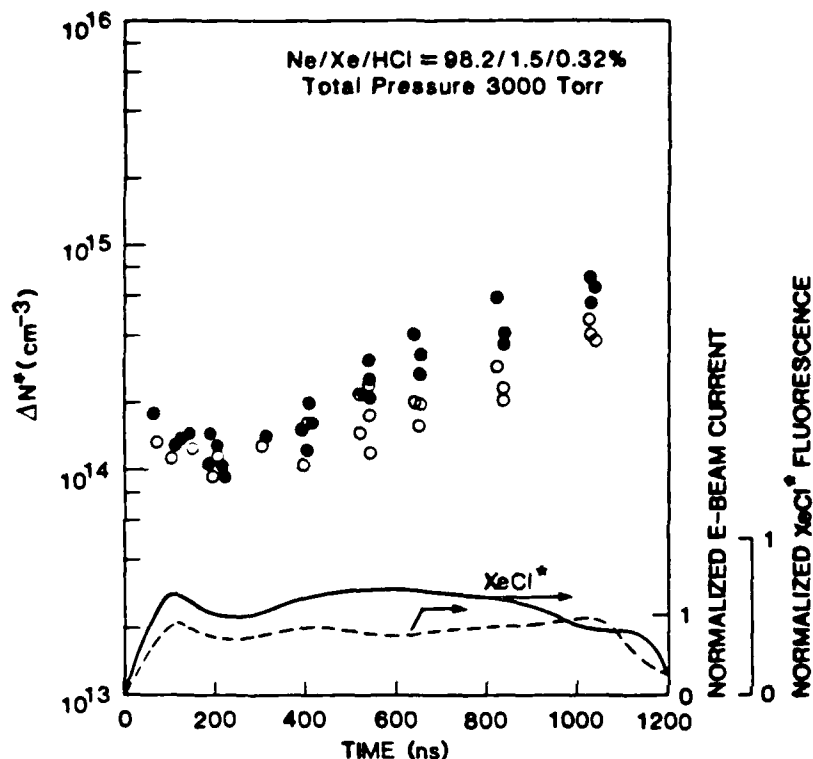
Figure 11. Typical xenon excited state density results for XeCl (98.2% Ne/1.5% Xe/0.32% HCl at 3000 Torr). The e-beam deposition is ≈250 kW/cm^3; a normalized trace of the e-beam current pulse is shown at the bottom of the figure. Solid and open circles correspond to density differences of the 823.2 and 828.0 nm transitions, respectively.

7. CONCLUSIONS

Measurements of fundamental quantities, such as time-dependent electron and excited state densities, has helped improve our understanding of the complex kinetics occurring in e-beam excited excimer lasers. It has also provided important data for validating models of these lasers. Unlike typical data used to anchor the models, this data tests the models on a basic level.

The techniques described are applicable to other types of lasers, for example discharge excited excimer and other gas lasers.

8. ACKNOWLEDGMENTS

The authors would like to acknowledge the helpful advice of Dr. J.J. Ewing and Dr. S.E. Moody, and the assistance of D.H. Ford, F.P. Braun, D.F. Kroeker, J.E. Kenyon, and J.W. Evenson during the development of these techniques.

9. REFERENCES

1. S.E. Moody, L.A. Levin, R.E. Center, J.J. Ewing, and E.L. Klosterman, "Measurements of lasing performance and efficiency of e-beam pumped xenon chloride," IEEE J. Quantum Electron., QE-17(9), 1856-1861 (1981).
2. W.D. Kimura, D.R. Guyer, S.E. Moody, J.F. Seamans, and D.H. Ford, "Electron density measurements of electron-beam pumped XeCl laser mixtures," Appl. Phys. Lett., 49(23), 1569-1571 (1986).

3. W.D. Kimura, D.R. Guyer, S.E. Moody, J.F. Seamans, and D.H. Ford, "Electron density measurements of electron-beam pumped XeF and KrF laser mixtures," Appl. Phys. Lett., 50(2), 60-62 (1987).

4. D.R. Guyer, W.D. Kimura, and S.E. Moody, "HCl burnup and electron densities in e-beam pumped XeCl," in Proceedings of the International Conference on Lasers '86, R.W. McMillan, ed., pp. 589-593, STS Press, McLean, (1987).

5. W.D. Kimura, S.E. Moody, and J.F. Seamans, "Narrowband extraction in XeF lasers," Conference on Lasers and Electro-Optics (CLEO), Baltimore, MD, Apr. 27-May 1, 1987.

6. F. Kannari, W.D. Kimura, J.F. Seamans, and D.R. Guyer, "Xenon excited state density measurements in electron-beam pumped XeCl laser mixtures," to be published in Applied Physics Letters, Dec. 14, 1987.

7. F. Kannari, W.D. Kimura, J.F. Seamans, and D.R. Guyer, "Xenon excited state densities in electron-beam pumped XeCl and XeF," submitted to Journal of Applied Physics.

8. W.D. Kimura, S.E. Moody, and J.F. Seamans, "F_2 fuel performance in XeF lasers at ambient and elevated temperatures," Appl. Phys. Lett., 49(5), 255-256 (1986).

9. E.T. Salesky and W.D. Kimura, "Electron-beam pumped KrF laser extraction measurements for high Kr concentration gas mixtures," IEEE J. Quantum Electron., QE-21(11), 1761-1765 (1985).

10. C.J. Buchenauer and A.R. Jacobson, "Quadrature interferometer for plasma density measurements," Rev. Sci. Inst., 48(7), 769-774 (1977).

11. S.E. Moody and W.D. Kimura, "The role of atomic absorbers in e-beam pumped XeF lasers," in Proceedings of the International Conference on Lasers '85, C.P. Wang, ed., pp. 423-428, STS Press, McLean (1986).

12. W.C. Marlow, Appl. Optics, 6(10), 1715-1724 (1967).

13. I. Smilanski and L.A. Levin, Optics Lett., 5(3), 93-95 (1980).

Xenon Excited State Densities
in Electron-Beam Pumped XeCl and XeF

F. Kannari, W.D. Kimura, J.F. Seamans, and Dean R. Guyer

Spectra Technology, Inc.

2755 Northup Way

Bellevue, WA 98004-1495

ABSTRACT

Understanding of the neutral channel formation kinetics in excimer laser gas mixtures has been limited by the lack of data on the pertinent excited state populations in these mixtures. Presented are time-dependent measurements of the lower level xenon excited state densities in electron-beam (e-beam) pumped XeCl and XeF laser mixtures (neon diluent). Measurements are obtained using hook interferometry under nonlasing conditions at an average excitation rate of ≈ 250 kW/cm^3 and e-beam pulse lengths of 0.4 and 1 μs. The population differences, ΔN^*, between four different electronic transitions [three in the Xe*(6s)-Xe**(6p) manifold, and one in the Xe**(6s')-Xe***(6p') manifold] are examined as a function of halogen concentration. For both XeCl and XeF at high initial halogen concentrations (>4 Torr), the ΔN^* densities of the Xe*(6s) and Xe**(6s') transitions are relatively constant during the 0.4 μs e-beam pulse [For ΔN^*(6s-6p): $\approx 4 \times 10^{14}$ cm^{-3} for XeCl, and $\approx 1.5 \times 10^{14}$ cm^{-3} for XeF]. At lower initial halogen concentrations, the ΔN^* densities of

6s-6p and 6s'-6p' start at the beginning of the pulse at approximately the same densities as the richer halogen mixtures, but at a certain point during the pulse, the ΔN^* densities abruptly increase. This increase can be >10 times for very lean halogen mixtures (1-2 Torr), and occurs at earlier times as the initial halogen concentration is reduced. From other measurements, this increase appears related to the depletion of the halogen. The observed lifetime of the $Xe^*(6s)$ densities is ≈ 2 μs for the low initial halogen concentration mixtures. Additional density data for halogen-free Ne/Xe and Ar/Xe mixtures are also presented.

I. INTRODUCTION

XeCl and XeF lasers have been operated with electron beam (e-beam) pumping for more than ten years[1,2]; however, many questions remain regarding the chemical kinetics and dynamical behavior of the laser media. In particular for XeCl lasers, the formation of XeCl* in e-beam pumped lasers has been the topic of considerable debate[3,4]. In general, there has been a lack of data on fundamental quantities that are directly related to the media kinetics. This paper presents experimental results on the lower level xenon excited state densities (more precisely, population differences) in e-beam pumped XeCl and XeF laser mixtures (nonlasing). As will be shown, the results have demonstrated some unexpected behaviors and revealed gaps in our understanding of the neutral channel kinetics. The measurements have also provided useful data to help validate computer models of these excimer lasers.

For XeCl, reaction of the first excitation state of xenon ($5p^56s$) with HCl(ν=0) is nearly thermoneutral (i.e. the branching ratio is nearly zero) with respect to XeCl* formation. Either higher xenon excited states or vibrationally hot HCl are necessary to efficiently form XeCl* through the harpoon reaction[5]. Recently, quenching rate constants and branching fractions for XeCl* formation generated by reaction of various xenon excited states with halogen donors have been measured using a tunable UV synchrotron source[6] and by laser induced fluorescence[7]. These results showed that HCl(ν=0) gives high XeCl* formation yield only for the 6p, 5d, 7s, and presumably higher

excitation states of xenon. Enhancement of $XeCl^*$ formation yield from $Xe^*(6s)$ with vibrationally excited HCl has also been observed[8]. It has been assumed in the past that the population in higher xenon excited states is minimal, that the role of excited state kinetics is less important in XeCl than in other rare-gas halide lasers, such as KrF^*, and that $XeCl^*$ is predominantly formed through Xe^+-Cl^- recombination[9,10].

In Ne/Xe mixtures (without HCl), neon ions and excited states, produced by the primary electrons of the e-beam and by high energy secondary electrons, produce xenon ions through three-body charge transfer reactions and Penning ionization. Xenon excited states are then produced through recombination reactions of xenon-based dimer ions (Xe_2^+, $NeXe_2^+$). The fraction of xenon excited states formed directly by electron collisions is negligible due to the low density of xenon compared to neon gas in these laser mixtures (typically Xe is 0.5-1.5% of the total mixture). With HCl in the mixture, as long as the Cl^- concentration is high, the Xe^+-Cl^- recombination reaction is fast and the xenon excited state formation channels are effectively intercepted preventing the formation of xenon excited states. Hence, measurement of the time-dependent xenon excited state densities provides an important check of our understanding of not only the neutral channel kinetics, but also the ion channel kinetics. For example, if the measured xenon excited state densities are reasonably low, this is indirect evidence of high Cl^- ions density; however, the dominant source of Cl^- is dissociative attachment from vibrationally excited HCl[10] and there are experimental results indicating that the density of vibrationally excited HCl is low[11-12]. In conjunction with our

4

previous measurements on the secondary electron density[13,14] and on HCl depletion[15], the xenon excited state density measurements related herein can significantly help improve our understanding of the complex rare-gas halogen kinetics.

In this paper, the Racah notation will be used to specify a given state of xenon. Specific xenon excited states are divided to three groups according to their energy levels. The symbol Xe^*, Xe^{**}, and Xe^{***} denotes $Xe(6s)$, $Xe(6s', 6p, \text{ and } 5d)$, and $Xe(\text{higher than } 5d)$ states, respectively.

II. EXPERIMENTAL TECHNIQUE

Xenon excited state densities are measured using hook interferometry[16]. This technique has been used before in gas lasers[17], but this is the first application in e-beam pumped excimer lasers. The experimental apparatus is described in detail elsewhere[18]; a schematic is shown in Fig. 1. The total optical path of the excited laser medium is 70 cm, and the e-beam excitation rate is ≈ 250 kW/cm^3, which is higher than during the earlier electron density measurements[13,14].

The basic principle of hook interferometry relies on the anomalous dispersion occurring around an atomic resonance transition; the strength of that dispersion is directly proportional to the population difference of that transition. By placing the laser medium in a Michelson interferometer and

5

analyzing the interference pattern with a spectrometer, the anomalous dispersion manifests itself in the form of "hooks" in the interference pattern at the output of the spectrometer.

Near an isolated transition at a wavelength λ_{ij} (where i and j are the lower and upper levels, respectively), but outside the core of the spectral line, the refractive index n is given by[19]

$$n(\lambda)-1 = \frac{r_o}{4\pi} \frac{f_{ij}\lambda_{ij}^3 N_i}{\lambda-\lambda_{ij}} \left[1 - \frac{g_i N_j}{g_j N_i}\right] \qquad [1]$$

where r_o is the classical electron radius, f_{ij} is the oscillator strength of the transition, $N_{i,j}$ are the population densities, and $g_{i,j}$ are the statistical weights of each level. The wavelength separation, Δ, between the hooks in the interference pattern is directly proportional to the square root of the population density difference between the two states and is given by:

$$\Delta N^* \equiv N_i \left[1 - \frac{g_i N_j}{g_j N_i}\right] = \frac{\pi K}{r_o \lambda_{ij}^3 \ell f_{ij}} \Delta^2 \qquad [2]$$

where ℓ is the length of the medium and K is a constant that can be determined from an undistorted interference pattern. If the oscillator strength for a particular transition is known, then the population difference, ΔN^*, can be determined from the hook spectra.

An energy level diagram showing the xenon transitions examined during the experiment is given in Fig. 2. Four particularly strong transitions are

6

examined: 1) 823.2 nm $(6s[3/2]_2^o - 6p[3/2]_2)$; 2) 828.0 nm $(6s[3/2]_1^o - 6p[1/2]_o)$; 3) 834.7 nm $(6s'[1/2]_1^o - 6p'[3/2]_2)$; and 4) 840.9 nm $(6s[3/2]_2^o - 6p[3/2]_1)$. Measured oscillator strengths for these lines are 0.23, 0.12, 0.37, and 0.012, respectively[20]. In this paper, the measured population density differences corresponding to each of the transitions are referred to as $\Delta N^*(823.2$ nm$)$, $\Delta N^*(828.0$ nm$)$, $\Delta N^*(834.7$ nm$)$, and $\Delta N^*(840.9$ nm$)$, respectively.

The value of K in Eq. (2) is typically $\approx 1.5 \times 10^3$ during the experiments. Thus, on our system a hook separation of 1 nm at 823.2 nm corresponds to a ΔN^* density of $\approx 7 \times 10^{13}$ cm^{-3}. Because the 823.2 nm and 828.0 nm lines are close to one another and they have relatively large oscillator strengths, the hook patterns about these lines can overlap each other at high xenon excited state densities. This can be avoided in principle by reducing the active length of the medium (i.e. ℓ); however, this was not convenient to do during the experiment. Hence, most of the xenon excited state densities greater than 10^{15} cm^{-3} are measured during the experiment by examining the 840.9 nm transition, because of its smaller oscillator strength, rather than the 823.2 and 828.0 nm lines.

Some of the transitions examined have a spectral line nearby that can interfere with the hooks formed on the side of the transition nearest the spectral line[18]. Two relatively strong transitions are observed at 826.6 and 822.1 nm near the 828.0 and 823.2 nm transitions. The transition at 826.6 nm corresponds to Xe $(6s'[1/2]_1^o - 6p'[1/2]_1)$. The transition at 822.1 nm has not

been positively identified, but it is probably from Ne_2^*, because it is also observed in pure neon mixtures. These lines disturb the hook formation on the short wavelength side of the 828.0 and 823.2 nm transitions, while the effects on the long wavelength side of the transitions are negligible.

For an isolated transition, the hook separation is symmetric about the transition wavelength. The quadratic Stark effect can displace the hooks towards long wavelengths[20], but because the electron density is relatively low[13,14] ($\approx 10^{15}$ cm^{-3}), this effect can be ignored. Therefore, during analysis of the data, it is assumed the total hook separation can be calculated by doubling the distance between the hook on the long wavelength side and line center. The experimental uncertainty of the data presented in this paper is $\approx \pm 10\%$.

Because hook interferometry gives the density <u>difference</u> between two states, to obtain the absolute density of the lower state requires the upper state population to be either negligibly small or estimable through other means. As explained in the following section, we believe the upper state populations for our experimental conditions are significant; however, estimating the populations, even by comparing the data gathered for different transitions, is difficult. Therefore, in order to avoid biasing the data with an assumption of the upper state densities, all the data presented in this paper represent the population difference, ΔN^*, between the upper and lower state of the transition examined.

III. RESULTS AND DISCUSSION

Before presenting the experimental results, it is helpful to review the important processes affecting the xenon excited state population distributions. In high pressure gas mixtures excited by an e-beam at a relatively high excitation rate, the population distributions in excited state manifolds are primarily defined by seven different processes: 1) The initial distribution as a result of formation by dimer ion recombinations[21]; 2) two-body collisional redistributions with rare gases; 3) three-body collisional deactivations (e.g. dimer molecule formations); 4) radiative deactivations; 5) excitations and de-excitations with secondary electrons; 6) quenching with the halogen gas; and 7) ionization of high level excited states.

If the collisional mixing by either neutral species or electrons is fast, the initial formation distribution will be quickly reduced to a steady-state distribution. The nature of this distribution will depend on the relative rates of neutral and electron energy transfer collisions. The collisional deactivation rate constants measured by Inoue et al.[22] for Ne and Ar show that two-body deactivations redistribute xenon densities between excited states separated by <5000 cm^{-1} with rate constants ranging from 0.2 to 36 x 10^{-11} $cm^3 s^{-1}$. Radiative lifetimes measured by Inoue et al.[22] range from 30 to 150 ns for xenon states located above $6p[1/2]_1$. Since the secondary electron number density is typically 10^{14}-10^{15} cm^{-3} in the excited gas mixture and their energy is $\approx$1-2 eV[23], it is reasonable to expect that stepwise excitation in the xenon excited state manifold will effectively compete with

two-body collisional deactivation. If the distribution in the xenon excited state manifold is characterized by a secondary electron temperature of 1.5 eV, which is a typical average electron temperature predicted by our model[10,23] for our experimental conditions, the upper state density of the probed transitions would be 23%, 12%, and 36% of the lower state density for the 823.2, 828.0, and 840.9 nm transitions, respectively. This represents an upper limit for the higher state populations since other heating sources do not exist. Moderation of this distribution will be governed by interaction with the ≈300 K gas. Moreover, ionization processes of higher Xe excited states tend to decrease the population of upper states.

At high pressures, three-body relaxations are also important. Xe^{***} and Xe^{**} form unstable Xe_2^{***} and Xe_2^{**} dimers, respectively, that can eventually predissociate into lower xenon excited state states. If the contribution of these three-body collisional deactivations is significant, the characteristic temperature defining the distribution between Xe^* and Xe^{**} can be lower than the electron temperature. Consequently, the fraction of upper state densities can be lower than those estimated in the previous paragraph. The issue of the xenon manifold temperature is discussed in more detail later.

Figures 3 and 4 show typical experimental results obtained at the 828.0, 823.2, and 834.7 nm transitions, for XeCl laser mixtures with an initial HCl concentration of 0.32% and 0.16%, respectively. The XeCl laser mixture is 1.5% Xe in Ne diluent at a total gas pressure of 3000 Torr. A normalized e-beam current pulse shape [400 ns full width at half maximum (FWHM)] is shown

10

at the bottom of the figures. As can be seen in Figs. 3 and 4, the density differences of ΔN^*(823.2 nm) and ΔN^*(828.0 nm) are relatively constant during the e-beam pumping, and decay rapidly at the termination of the e-beam pulse.

As noted before, excited xenon is produced primarily by recombination of dimer ions with secondary electrons rather than direct excitations of ground state Xe by high energy electrons. At high HCl concentrations, secondary electrons are efficiently removed by dissociative attachment reactions with vibrationally excited HCl. The Cl^- ions produced reduce the dimer ion populations through ion-ion recombination reactions. Therefore, as long as dissociative attachment dominates the electron loss process, the Xe^* density will decrease with increasing initial HCl concentration. In fact, as seen in Figs. 3 and 4, experimental results for 0.32% HCl of ΔN^*(823.2 nm) are ≈47% of the 0.16% HCl mixture. These Xe^* densities agree with model predictions[23] which assume high dissociative attachment rate constants for vibrationally excited HCl as reported by Allan and Wong[24].

Figures 5-8 show time-dependent ΔN^* densities for lower initial HCl concentrations from 0.12 to 0.04%. Two unexpected xenon excited state density behaviors are observed. First, although higher Xe^* densities are expected at the beginning of the pulse for lower HCl concentrations and, in fact, the ΔN^* measured during the first 200 ns does increase when the initial HCl concentration is reduced to 0.09%, the ΔN^* densities actually tend to <u>decrease</u> as the HCl concentration is reduced to 0.08 and 0.04%. The ΔN^*(834.7 nm) density of 0.08% HCl is also smaller than that of the 0.16% HCl mixture during

the e-beam pulse. Second, at low HCl concentrations, the ΔN^* densities dramatically increase at a well defined point during the e-beam pulse. As the initial HCl concentration is reduced, the ΔN^* density begins to increase at earlier times. This increase is so rapid that it appears to indicate some type of threshold effect. For the particular energy loading and pulse duration used in Figs. 3-8, this increase occurs at the very end of the e-beam pulse for the 0.12% HCl mixture, and the ΔN^* density decays rapidly after termination of the e-beam. However, for HCl concentrations <0.12%, the ΔN^* density does not decay immediately after termination of the e-beam pulse, but instead the decay time becomes progressively longer with decreasing initial HCl concentration. This will be discussed in more detail later.

Also shown in Fig. 7 are results of measuring the ΔN^* density of <u>neon</u> excited state for the $(3p[5/2]_3 - 3d[7/2]_4^0)$ transition at 837.8 nm. It is interesting that the neon excited state density does not increase abruptly like the xenon densities, but rather follows the e-beam pumping. The abrupt increase of the xenon excited state density appears to be caused by destruction of the reaction balance between ion-ion and electron-dimer ion recombination processes, as a result of HCl consumption. Since neon excited states are mainly produced by high energy electron excitations, they are not affected by the HCl consumption. During the electron density measurements[13,14], the electron densities also tended to increase abruptly at a certain point during the e-beam pumping. This point also tends to occur at earlier times as the initial HCl concentration is lowered. The consumption of HCl during the pump pulse increases the secondary electrons and reduces Cl^-

ions resulting in an increase in electron-dimer ion recombinations.

The model[23] predicts these abrupt increases only when additional dissociation of HCl to neutrals is included at effective rates larger than commonly accepted. In other words, the HCl burn-up rate appears to be underestimated, especially at low initial HCl concentrations. Additional HCl destruction channels at low HCl concentrations may still not be identified yet and will be discussed later.

At low HCl concentrations, the ΔN^*(840.9 nm) density decays slowly after termination of the e-beam pulse. In high pressure pure rare gas mixtures excited by an e-beam, electrons are controlled by recombinations with dimer ions. The rare gas excited states formed by recombination processes produce dimer molecules through three-body collisions, and the inner energy of the total xenon system decays mainly through radiative deactivations of dimer molecules. Therefore, as long as the three-body dimer molecule formation is fast, rare gas excited states cannot survive for very long after the e-beam termination even after the HCl is completely consumed. During the secondary electron density measurements, a long electron density lifetime was also observed at low HCl concentrations[13,14]. To conserve charge balance, the secondary electron density must be balanced with some positive ions. Therefore, the long xenon excited state lifetime may be caused by relatively long deactivation processes, and by some feeding processes such as recombinations of dimer ions even after the e-beam excitation. Energy transfer processes from excited Cl atoms are another possible path to form

xenon excited states. Comparing Figs. 6 and 7, it is interesting to note how sensitive this lifetime is to small changes in the initial halogen concentration.

To eliminate the effects of the halogen, Ne/Xe and Ar/Xe mixtures were also examined using the hook interferometry system. The results for the binary mixtures are shown in Fig. 9. The Xe^* lifetime is surprisingly long, and its decay behavior is not purely exponential.

To help interpret the binary mixtures results, Fig. 10 depicts the key kinetics pathways in an e-beam excited Ne/Xe gas mixture. The major dimer ion species in Ne/Xe mixtures are believed to be $NeXe^+$ and Xe_2^+.[9,10] In neon gas containing a trace of xenon, Xe_2^+ is formed mainly from $NeXe^+$ rather than directly from Xe^+. Similarly, the major dimer molecules in Ne/Xe mixtures are thought to be $NeXe^*$ and Xe_2^*. However, the heteronuclear species $NeXe^+$ and $NeXe^*$ are bound very weakly (<0.05 eV), so that the reverse reaction to produce Xe^+ and Xe^* from these heteronuclear species should be very fast[25]. If these reverse reactions are fast enough that the effective densities of heteronuclear species are negligibly small, and if the formation reactions of molecular species of Xe_2^+ and Xe_2^* with neon as a third-body species are significantly slower than expected, viz. the reactions:

$$Xe^+ + Xe + Ne \rightarrow Xe_2^+ + Ne \qquad [3]$$

$$Xe^* + Xe + Ne \rightarrow Xe_2^* + Ne, \qquad [4]$$
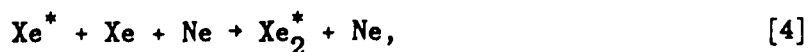
then the total rates of formation of Xe_2^+ and Xe_2^* will be much less than those
for the corresponding rare gas dimer species in pure xenon. In fact, the
rates used in the model are estimated or extrapolated from results for
collision species other than neon[26-28]. Consequently, the densities of Xe-
based molecular species are much smaller than would be expected considering
the total pressure. If the preceding assumptions are correct, then the
dominant ion in the Ne/Xe mixture is Xe^+, and the electron loss mechanism by
electron-dimer recombination is slow, with the result that the electron
density in the Ne/Xe mixture remains high after the termination of e-beam
pumping. Penning ionization processes can also help feed the electron density
population. This is one noteworthy difference between a pure rare gas and a
rare gas containing a trace of xenon. Therefore, even after termination of e-
beam pumping, the recombination process producing xenon excited states
continues at a low rate, some of the excited species are ionized back to Xe^+
through Penning ionization, and the total xenon excited state system decays
through the relatively slow Xe_2^* formation process. If the electron
temperature remains high enough, the produced Xe_2^* is excited to unstable Xe_2^{**}
states, which again produce Xe^*.[29]

Figure 11 shows the fluorescence time history of the Ne/Xe mixture
obtained with a VUV photodiode (ITT F4115, 120 nm<λ<320 nm). The major
contribution is dimer emission of Xe_2^*. Surprisingly, the fluorescence
continues to increase after termination of the e-beam pulse and peaks at
$\approx$1.25 μs after the pulse. This fluorescence behavior of Xe_2^* is caused by a
decrease of Xe_2^{**} formation by secondary electrons due to the drop of the

15

electron temperature after the e-beam ends[29].

In Fig. 9, ΔN^* (823.2 nm, and 828.0 nm) measured for an Ar/Xe mixture are also shown. The decay time of the xenon excited state system is much faster than in the Ne/Xe mixture. This is because the binding energies of $ArXe^+$ and $ArXe^*$ are relatively large compared to those of $NeXe^+$ and $NeXe^*$, respectively, and a larger amount of dimer molecules exist in Ar-based mixtures[30]. Xe_2^+ and Xe_2^* formation reactions with argon as a third-body species are also faster than with neon[26-28]. Therefore, the recombination and deactivation processes for xenon excited state are faster than those in Ne-based mixtures.

Figures 12 and 13 shows time-dependent ΔN^* densities obtained under extended (1 μs) e-beam excitation for an initial HCl concentration of 0.32 and 0.16%, respectively. Sidelight fluorescence of $XeCl^*$(B-X) is shown at the bottom of each figure with the normalized e-beam current pulse. For 0.32% HCl, the ΔN^* density does not stay constant, but gradually increases towards the end of the e-beam pulse. This gradual increase may be caused by an increase in the gas temperature during the e-beam pumping which leads to a decrease in the ion-ion recombination rates[31]. For 0.16% HCl, the ΔN^* density increases abruptly at $\approx$600 ns into the e-beam pulse. The sidelight fluorescence for the 0.16% HCl mixture begins to decrease at approximately the same time as the increase of the ΔN^* density. Since the increase of ΔN^* density also suggests a corresponding increase of the Xe^{**} and Xe^{***} densities, photoionizations of these higher excited states should increase the absorption losses in a laser and tend to reduce the laser output. This may be part of the reason for the premature laser pulse termination observed in some

experiments[32].

Measurements also show that the Xe^* density increases with increasing
initial xenon concentration. With 0.16% HCl and at 150 ns into the e-beam
pulse, ΔN^*(823.2 nm) densities of $\approx 2.0 \times 10^{14}$ and $\approx 4.5 \times 10^{14}$ cm^{-3} are
obtained for 0.5% and 3.0% Xe, respectively.

It is interesting to examine whether the abrupt increase of xenon
excited state density is a common behavior when using different halogen
species. Results of ΔN^* density measurements performed for XeF laser mixtures
are shown in Figs. 14-16. The XeF laser mixture is 0.5% Xe in Ne diluent to a
total gas pressure of 2888 Torr.

One must be careful when comparing the ΔN^* results for F_2 with HCl
because of the different dissociative attachment rate constants between ground
state HCl and F_2. The rate constants, however, actually become comparable to
one another once the HCl is vibrationally excited. Although the 0.1% F_2
mixture (Fig. 15) and the 0.09% HCl mixture (Fig. 6) start out with similar
amounts of halogen and the rapid increase in ΔN^* density occurs approximately
at the same time, the lifetime after e-beam termination of the xenon excited
states is much longer for the 0.1% F_2 case. Based on the earlier discussion
regarding the long lifetimes observed in the binary rare gas mixtures, this
seems to imply that more of the F_2 has been consumed than in the HCl case.
The estimated effective lifetime of the xenon ΔN^* excited state for the 0.05%
F_2 mixture is ≈ 2 μs, which agrees well with the value for the XeCl laser

mixture.

From the ΔN^* density results for HCl and F_2 halogens, it is confirmed that regardless of which halogen gas is used, the halogen burn-up causes an abrupt change in the energy flow of the dimer ion recombination channel and increases the xenon excited state density. In the Ne-based mixture with a trace of xenon, the main ion species is Xe^+, and recombination processes are relatively slow. Therefore, the decay rates of the secondary electron and xenon excited state densities are very long.

The xenon excited state density results, besides demonstrating the interdependence on the halogen concentration, also provide an opportunity to examine part of the xenon excited state distribution and therefore estimate indirectly the manifold temperature. However, to perform such an analysis requires some assumption regarding the form of the distribution (e.g. Boltzmann versus non-Boltzmann). Because of this and because the experiment only examined a limited portion of the xenon manifold and did not measure absolute level densities, the following temperature analysis is intended to illustrate only one possible interpretation of the data. It should be emphasized that the experiment was not designed to measure the manifold temperature.

The analysis is further complicated by the fact that at least part of the xenon manifold must be in nonequilibrium as evidenced by the existence of infrared xenon lasers. Lasing occurs between the 5d and 6p xenon excited states when mixtures of Ar/Xe or Ne/Xe at >1 atm are excited by e-beams or e-

beam sustained discharges[33-35]. If, however, we assume the levels examined in this experiment are roughly in equilibrium, then one approach for analyzing the data is to assume a simple model where the xenon excited state manifold is characterized by a single temperature. It is possible to estimate such a temperature by assuming a Boltzmann distribution for the entire xenon excited state manifold between the 6s and 6p' levels (see Fig. 2). For example, comparing the ΔN^*(834.7 nm) data to the ΔN^*(823.2 nm) or ΔN^*(828.0 nm) results given in Fig. 4 for 0.16% HCl would indicate that the excitation temperature in the Xe^* manifold is $\approx$0.8 eV. This is comparable to the predicted electron temperature of 1.5 eV mentioned earlier and supports the hypothesis that electron mixing is significant in the lower excited state manifolds for this experiment.

As another example of the application of this simple analysis to the data, the calculated excitation temperature from the ΔN^*(840.9 nm) and ΔN^*(834.7 nm) data for a 0.08% HCl mixture is $\approx$0.9 eV during the e-beam pumping. The excitation temperature decreases after the e-beam termination to $\approx$0.3-0.4 eV. For a Ne/Xe mixture, the excitation temperature decreases from 0.5 eV at 400 ns into the e-beam pulse to 0.4 eV at 1.4 μs after the e-beam pulse. Comparing both mixtures, the halogen gas tends to increase the excitation temperature, but the excitation temperatures without any initial halogen or after the halogen has been depleted are very similar. This trend is expected if the excitation temperature is a positive function of average electron temperature. With the halogen gas, low energy electrons are removed through dissociative attachment reactions and the average electron temperature

is raised; indeed, this is predicted by the model[23].

If indeed the excitation temperature of Xe^{**} state is comparable to the estimated secondary electron temperature, then considering the large degeneracies of the high excitation states, the total xenon excited state densities above the first excitation state (6s) would appear to be significant. For example, assuming the entire xenon excited state manifold is governed by a Boltzmann distribution, one would predict, for a 1 eV excitation temperature, an effective degeneracy for Xe^{**} of order 50 and for Xe^{***} a value 30 times greater than that. Relative to Xe^{*}, this implies the Xe^{**} and Xe^{***} densities are considerably larger than the Xe^{*} density. However, due to the high ionization rates of the high level xenon states, it is more likely that the excitation temperature of Xe^{***} is smaller than that of Xe^{**}. Nonetheless, even if the densities of the high level xenon states are only comparable to the Xe^{*} density, the impact on the kinetics is significant. Xe^{***} can produce $XeCl^{*}$ through reactions with ground state HCl at a branching ratio of nearly one[6]. Assuming the total Xe^{**} and Xe^{***} densities are the same as the Xe^{*} density, and using a Xe^{*} density of 5×10^{13} cm^{-3} obtained from our experiment for a 0.16% HCl mixture, an estimated $XeCl^{*}$ formation efficiency through the harpoon reactions with higher excited states of xenon is 7%, which is approximately half of the formation efficiency estimated from the small-signal gain of a XeCl laser[10]. This $XeCl^{*}$ formation is also an additional HCl burn-up channel. Moreover, since the higher excited states of xenon are easily ionized by electrons or photons, they are a source of extra secondary electrons which tend to accelerate the HCl burn-up.

20

The preceding analysis relies on the distribution being approximately Boltzmann. If in reality it is significantly non-Boltzmann, then it is not possible, without additional measurements of the higher xenon excited state level densities, to infer the manifold temperature from our data.

IV. CONCLUSIONS

The time-dependent excited state density measurements of xenon in e-beam pumped Ne/Xe/HCl and Ne/Xe/F$_2$ laser mixtures as a function of halogen concentration have yielded important new insights into the neutral and ionic kinetics occurring in these plasmas.

For both laser mixtures, as long as the halogen density is high, secondary electrons and xenon ions are controlled by dissociative attachment reactions with the halogen and ion-ion recombination reactions, respectively. In addition, the amount of electron-dimer ion recombination is relatively small, which results in low xenon excited state densities. When a certain amount of halogen is consumed, the energy flow channel is very rapidly switched to the dimer recombination channel and the excited state density of xenon abruptly increases. This increase of the xenon excited state population is coincident with a similar increase of the secondary electrons. Although the kinetics model can qualitatively predict these trends, the HCl depletion is, thus far, underpredicted especially for low initial HCl concentrations. A population increase of the higher level xenon excited states is also observed

21

as the halogen is burned up; this presumably results in an increase of photoionization at the laser wavelength. This may contribute to the premature termination of the XeCl laser output under high energy loading conditions.

In binary mixtures of neon with a trace of xenon, the major positive ion species is xenon ion, and the electron loss mechanism by dissociative recombination is slow, with the result that the electron density in the Ne/Xe mixture remains high after the termination of e-beam pumping. Penning ionization processes with Xe^* also help maintain the electron density. The densities of xenon-based molecules such as $NeXe^+$, Xe_2^+, $NeXe^*$, and Xe_2^*, are low because of the relatively small binding energy of the heteronuclear molecules, and the low rate constants for three body collisional reactions with neon as a third-body species. Therefore, even after the termination of e-beam pulse, the recombination processes producing xenon excited states still continue at a slow rate, and the total xenon excited state system decays through the relatively slow Xe_2^* formation process. A xenon excited state $Xe^*(6s)$ lifetime of ≈ 2 μs is observed for the Ne/Xe mixture and also for mixtures with lean halogen concentrations. This is a noteworthy difference from pure rare gases.

Assuming a Boltzmann distribution for the xenon manifold, the excitation temperature during e-beam pumping estimated from the data for the lower Xe manifolds is ≈ 1 eV, which is very close to the predicted electron temperature of 1.5 eV by the model. If most of the distribution of the xenon excitation manifolds are characterized by this high temperature, a significant population

of xenon excited states exists above the first excitation level of $Xe^*(6s)$ due to the large degeneracy of the higher excitation levels. The higher state xenon excited states can produce $XeCl^*$ with a high formation yield, and are also easily ionized by the electrons and photons at the laser wavelength. These reactions are additional HCl depletion mechanisms, and will produce extra electrons which can also dissociatively attach to HCl.

A detail modeling of the xenon manifolds is needed to fully understand the experimental results, and at the same time it must be able to predict the nonequilibrium distributions observed in xenon infrared lasers. Additional xenon excited state density measurements, particularly for the high level xenon manifolds, would also be very useful for estimating the characteristic distribution temperatures and to provide feedback to the theoretical model.

ACKNOWLEDGMENTS

REFERENCES

1. J.J. Ewing and C.A. Brau, Appl. Phys. Lett., 27, 350 (1975).

2. E.R. Ault, R.S. Bradford, Jr., and M.L. Bhaumik, Appl. Phys. Lett., 27, 413 (1975).

3. D.L. Huestis, 39th Annual Gaseous Electronics Conference, Madison, WI, Oct. 7-10, 1986.

4. Workshop on XeCl Kinetics, SRI International, Menlo Park, CA, Dec. 19, 1985, SRI Report No. MP 86-044.

5. R.C. Sze, IEEE J. Quantum Electron., QE-15, 1338 (1979).

6. D.C. Lorents, in Proceedings of the International Conference on Lasers '84, Nov. 26-30, 1984 (STS Press, McLean, 1985), p. 575.

7. J.K. Ku and D.W. Setser, Appl. Phys. Lett., 48, 689 (1986).

8. R.S.F. Chang, J. Chem. Phys., 76, 2943 (1982).

9. L.A. Levin, S.E. Moody, E.L. Klosterman, R.E. Center, and J.J. Ewing, IEEE J. Quantum. Electron., QE-17, 2282 (1981).

10. F. Kannari, A. Suda, M. Obara, and T. Fujioka, IEEE J. Quantum Electron., QE-19, 1587 (1983).

11. D. Kligler, Z. Rozenberg, and M. Rokni, Appl. Phys. Lett., 39, 319 (1981).

12. R.E. Center, J.H. Jacob, M. Rokni, and Z. Rozenberg, Appl. Phys. Lett., 41, 116 (1982).

13. W.D. Kimura, D.R. Guyer, S.E. Moody, J.F. Seamans, and D.H. Ford, Appl. Phys. Lett., 49, 1569 (1986).

14. W.D. Kimura, D.R. Guyer, S.E. Moody, J.F.Seamans, and D.H. Ford, Appl. Phys. Lett., 50, 60 (1987).

15. D.R. Guyer, W.D. Kimura, and S.E. Moody, in Proceedings of the International Conference on Lasers '86, Orlando, FL, Nov. 3-7, 1986 R.W. McMillan, Editor (STS Press, McLean, 1987), p. 589.

16. W.C. Marlow, Appl. Opt., 6, 1715 (1967).

17. I. Smilanski and L.A. Levin, Optics Lett., 5, 93 (1980).

18. F. Kannari, W.D. Kimura, J.F. Seamans, and D.R. Guyer, "Xenon Excited State Density Measurements in Electron-Beam Pumped XeCl Laser Mixtures,"

to be published in Applied Physics Letters, Dec. 14, 1987 (Ms. #L-0083).

19. S.A. Kopff and G. Breit, Rev. Mod. Phys., $\underline{4}$, 471 (1932).

20. V.R. Lazovskaya and G.K. Tumakaev, Sov. Phys. Tech. Phys., $\underline{24}$, 328 (1979).

21. Y-J. Shiu, M.A. Biondi, and D.P. Sipler, Phys. Rev. A, $\underline{15}$, 494 (1977).

22. G. Inoue, J.K. Ku, and D.W. Setser, J. Chem. Phys., $\underline{81}$, 5760 (1984).

23. F. Kannari, W. D. Kimura and E. T. Salesky, Conference on Lasers and Electro-Optics (CLEO), April 26 - May 1, 1987, Baltimore, ML, (unpublished).

24. M. Allan, and S.F. Wong, J. Chem. Phys., $\underline{74}$, 1687 (1981).

25. H.L. Kramer, J.A. Herce, and E.E. Muschlitz. Jr., J. Chem. Phys., $\underline{56}$, 4166 (1972).

26. J.K. Rice and A.W. Johnson, J. Chem. Phys., $\underline{63}$, 5235 (1975).

27. P.K. Leichner, K.F. Palmer, J.D. Cook, and M. Thieneman, Phys. Rev., $\underline{A13}$, 1787 (1976).

28. A.P. Vitols and H.J. Oskam, Phys. Rev., $\underline{A8}$, 1860 (1973).

29. C. Duzy, and J. Boness, IEEE J. Quantum Electron., $\underline{QE-16}$, 640 (1980).

30. Y. Nachshon, F.K. Tittel, and W.L. Wilson, Jr., J. Appl. Phys., $\underline{56}$, 36 (1984).

31. J.M. Hoffman and J.B. Moreno, Sandia National Laboratory, Albuquerque, NM, 1980, Report No. SAND 80-1486, (unpublished).

32. L. Litzenberger, R. Slater, and D. Trainer, in Proceedings of the International Conference on Lasers '85, Las Vegas, NV, Dec. 2-6, 1985, C.P. Wang, Editor (STS Press, McLean, 1986), p. 573.

33. L.A. Newman and T.A. DeTemple, Appl. Phys. Lett., $\underline{27}$, 678 (1975).

34. S.A. Lawton, J.B. Richards, L.A. Newman, L. Specht, and T.A. DeTemple, J. Appl. Phys., $\underline{50}$, 3888 (1979).

35. N.G. Basov, A. Y. Chugunov, V.A. Danilychev, I.V. Kholin, and M.N. Ustinovsky, IEEE Quantum Electron., $\underline{QE-19}$, 126 (1983).

FIGURE CAPTIONS

Fig. 1.   Schematic of xenon excited state density measurement system.

Fig. 2.   Energy level diagram for Xe from 65000 to 90000 cm^{-1}. The 5d, 7p,
and 6d states are not shown. The four transitions measured during
the experiment are indicated.

Fig. 3.   Time-dependent ΔN^* densities of a XeCl mixture (1.5% Xe, balance Ne
to 3000 torr, temperature 294 K) for an initial HCl concentration of
0.32%. Solid and open circles correspond to ΔN^*(823.2 nm) and
ΔN^*(828.0 nm), respectively. The dashed curve is a normalized trace
of the e-beam current waveform (400 ns FWHM).

Fig. 4.   Time-dependent ΔN^* densities of a XeCl mixture for an initial HCl
concentration of 0.16%. Other gas parameters and plot parameters are
the same as in Fig. 3, except open triangles correspond to ΔN^*(834.7
nm) and solid squares correspond to ΔN^* of the neon excited state
$(3p[5/2]_3 - 3d[7/2]_4^o)$ transition at 837.8 nm. The ΔN^* of the neon
excited state is scaled by a factor of 10.

Fig. 5.   Time-dependent ΔN^* densities of a XeCl mixture for an initial HCl
concentration of 0.12%. Other gas parameters are the same as in
Fig. 3. Solid triangles correspond to ΔN^*(840.9 nm).

Fig. 6. Time-dependent ΔN^* densities of a XeCl mixture for an initial HCl
concentration of 0.09%. Other gas parameters are the same as in
Fig. 3. Plot parameters are the same as in Fig. 5.

Fig. 7. Time-dependent ΔN^* densities of a XeCl mixture for an initial HCl
concentration of 0.08%. Other gas parameters are the same as in
Fig. 3. Plot parameters are the same as in Figs. 3-5.

Fig. 8. Time-dependent ΔN^* densities of a XeCl mixture for an initial HCl
concentration of 0.04%. Other gas parameters are the same as in
Fig. 3. Plot parameters are the same as in Figs. 3 and 5.

Fig. 9. Time-dependent ΔN^* densities of a Ne/Xe mixtures (1.5 % Xe, balance
Ne to 3000 torr, temperature 294 K). Plot parameters are the same as
in Figs. 4 and 5. Dotted lines with solid and open circles are
ΔN^*(823.2 nm) and ΔN^* (828.0 nm), respectively, measured for an Ar/Xe
mixture (1.5% Xe, balanced Ar to 1500 torr, temperature 294 K).

Fig. 10. Block diagram showing key kinetics paths in the Ne/Xe rare gas
system.

Fig. 11. Fluorescence time history in the wavelength region of 120<λ<320 nm,
obtained from a Ne/Xe mixture (1.5 % Xe, balance Ne to 3000 torr,
temperature 294 K). The dashed curve is a normalized trace of the e-
beam current waveform (400 ns FWHM).

29

Fig. 12. Time-dependent ΔN^* densities of a XeCl mixture for an initial HCl concentration of 0.32%. Other gas parameters and plot parameters are the same as in Fig. 3. The dashed curve is a normalized trace of the e-beam current waveform (1 μs FWHM). The solid curve is a normalized trace of the XeCl* sidelight fluorescence waveform.

Fig. 13. Time-dependent ΔN^* densities of a XeCl mixture for an initial HCl concentration of 0.16%. Other gas parameters are the same as in Fig. 3. Plot parameters are the same as in Figs. 3 and 5. The dashed curve is a normalized trace of the electron beam current waveform (1 μs FWHM). The solid curve is a normalized trace of the XeCl* sidelight fluorescence waveform.

Fig. 14. Time-dependent ΔN^* densities of a XeF mixture (0.5% Xe, balance Ne to 2888 torr, temperature 294 K) for initial F_2 concentration of 0.15%. The dashed curve is a normalized trace of the e-beam current waveform (400 ns FWHM). Plot parameters are the same as in Figs. 3 and 4.

Fig. 15. Time-dependent ΔN^* densities of a XeF mixture for initial F_2 concentration of 0.10%. Other gas parameters are the same as in Fig. 14. The dashed curve is a normalized trace of the e-beam current waveform (400 ns FWHM). Plot parameters are the same as in Figs. 3-5.

Fig. 16. Time-dependent ΔN^* densities of a XeF mixture for initial F_2

30

concentration of 0.05%. Other gas parameters are the same as in Fig. 14. The dashed curve is a normalized trace of the e-beam current waveform (400 ns FWHM). Plot parameters are the same as in Figs. 3-5.

.

Fig. 1

Figure 2

Ne/Xe/HCl=98.2/1.5/0.32%
Total Pressure 3000 Torr

ΔN^* (cm^{-3})

NORMALIZED E-BEAM CURRENT

10^{15}

10^{14}

10^{13}

0   200   400   600   800   1000   1200

TIME (ns)
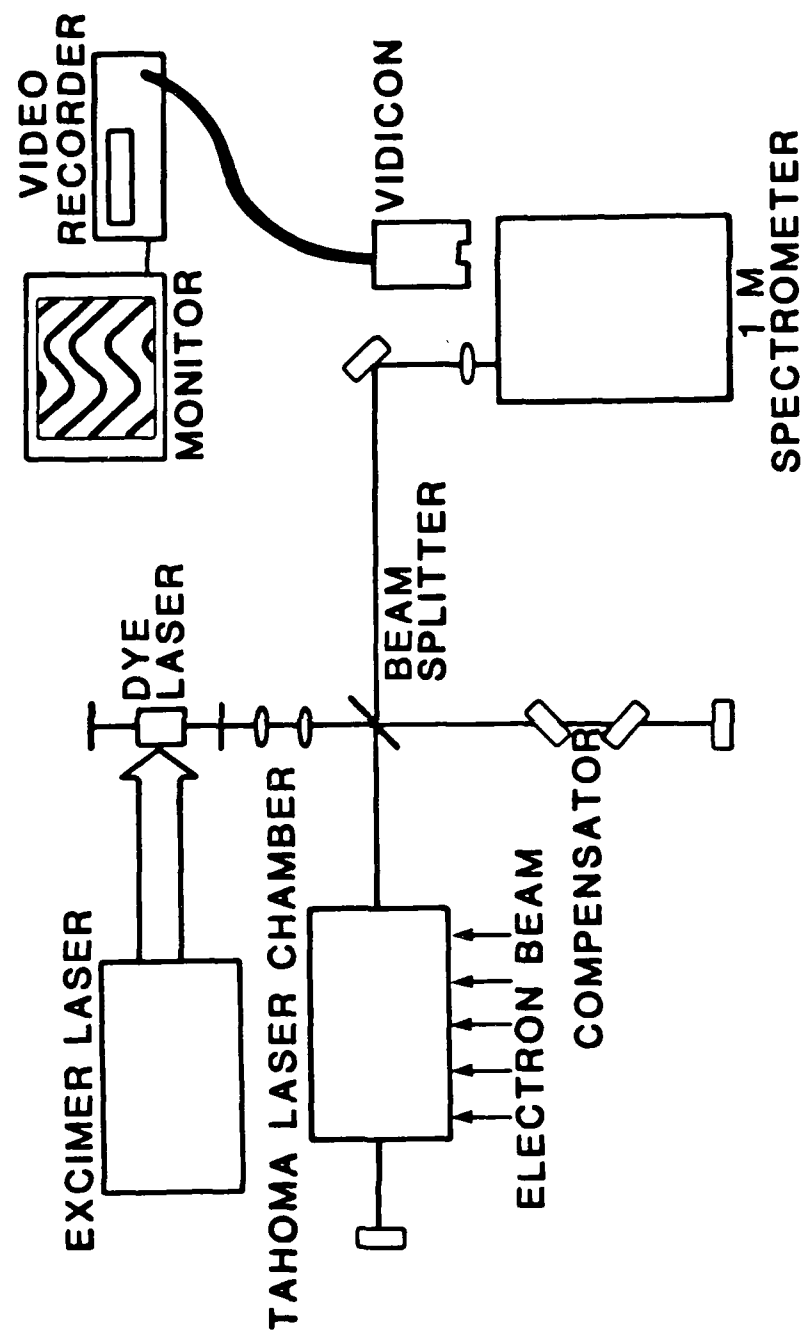
Figure 3

Figure 4

Figure 5

Figure 6

37

Figure 7

38

Figure 8

39

10^{16}

10^{15}

$\Delta N^* \, (cm^{-3})$

10^{14}

10^{13}

Ne**(x10)

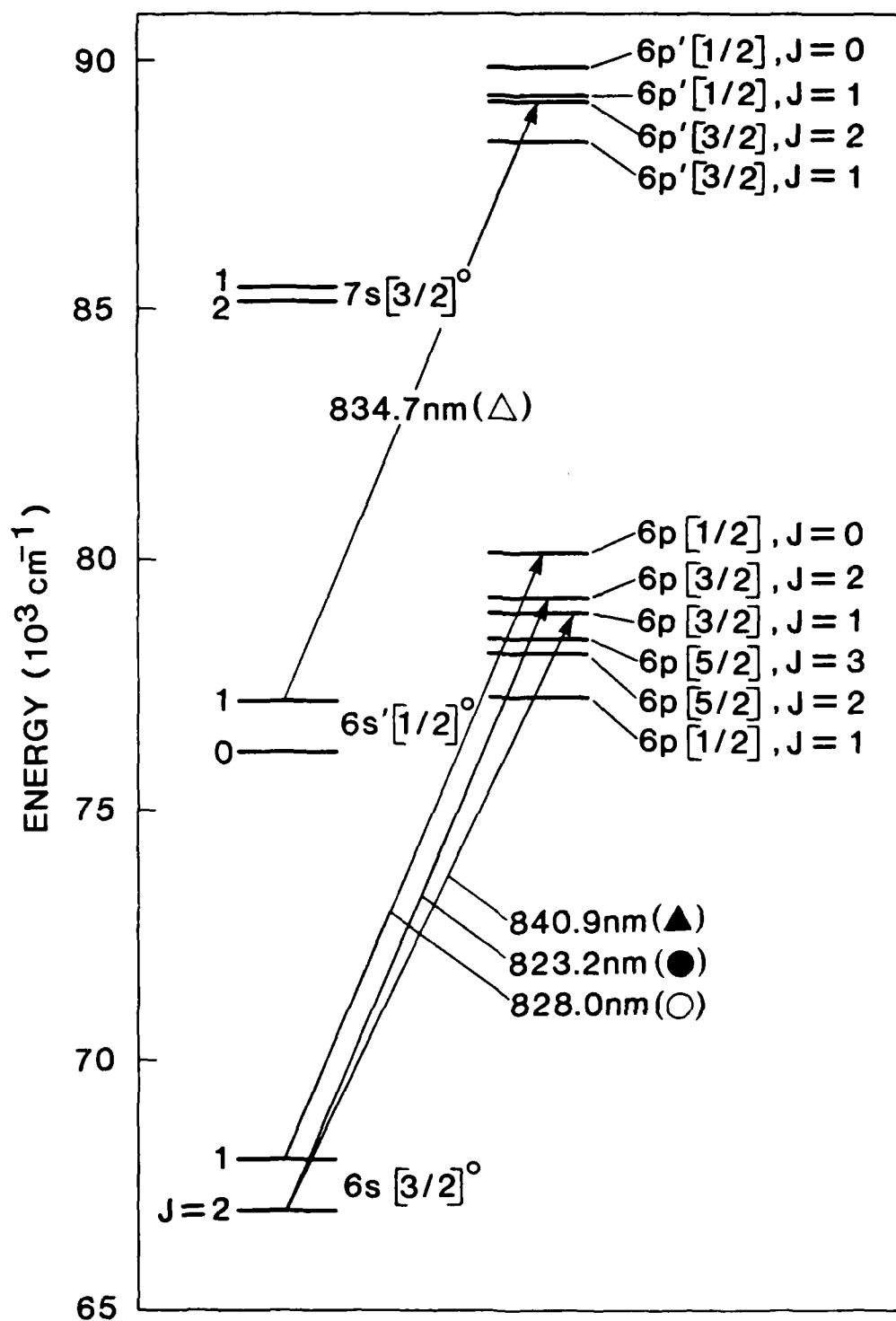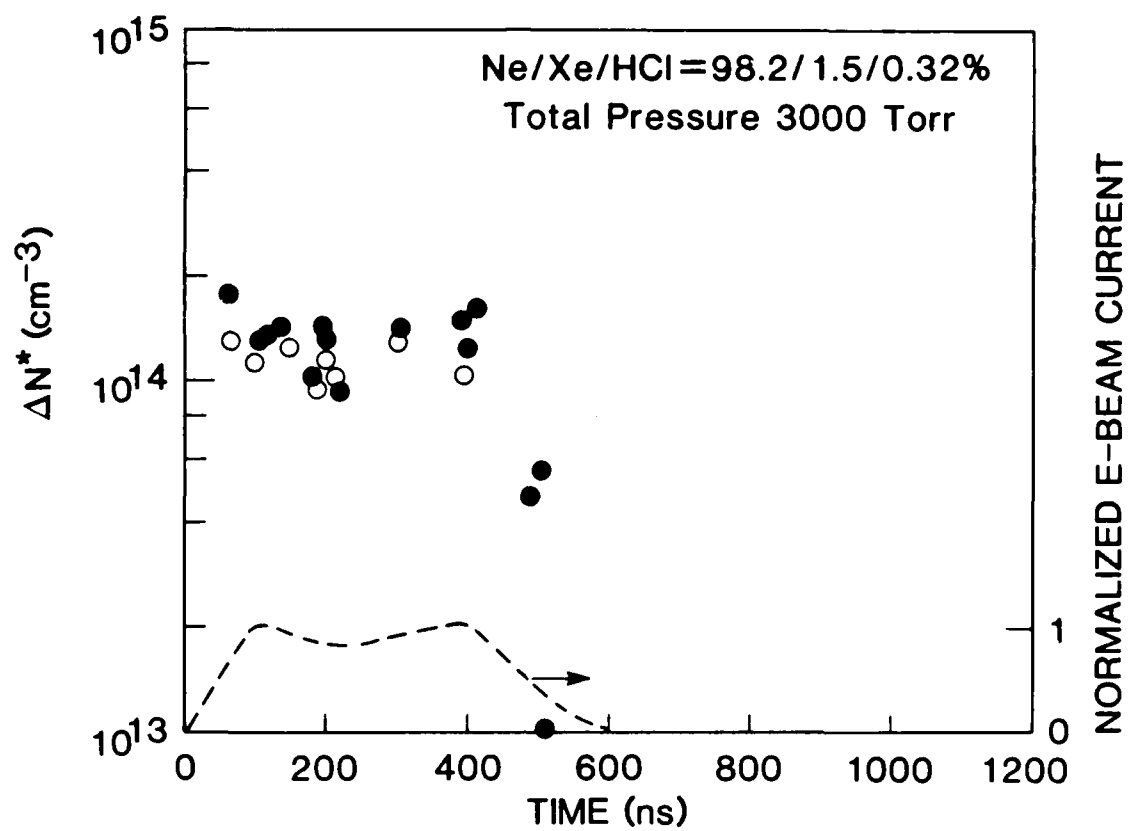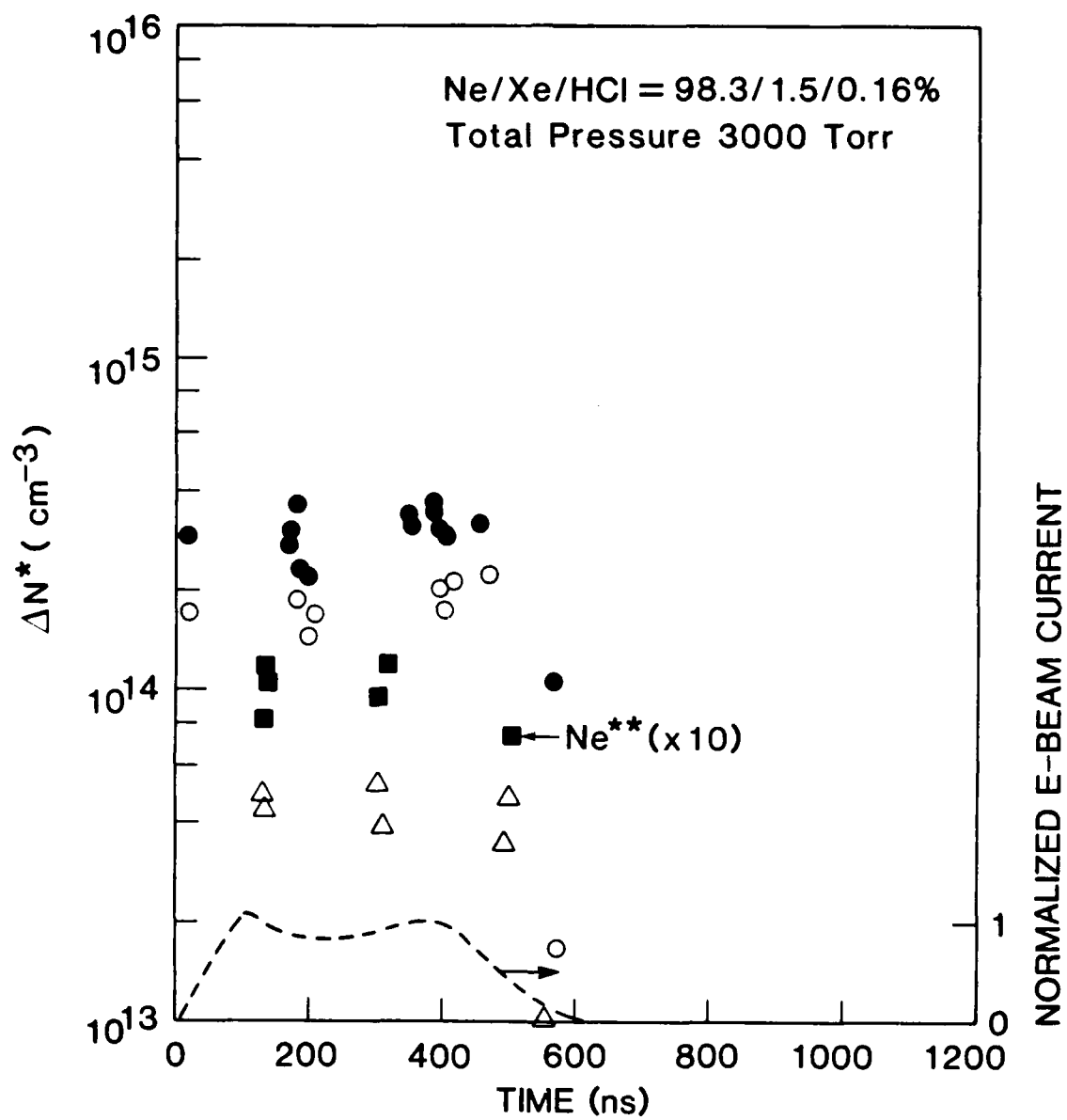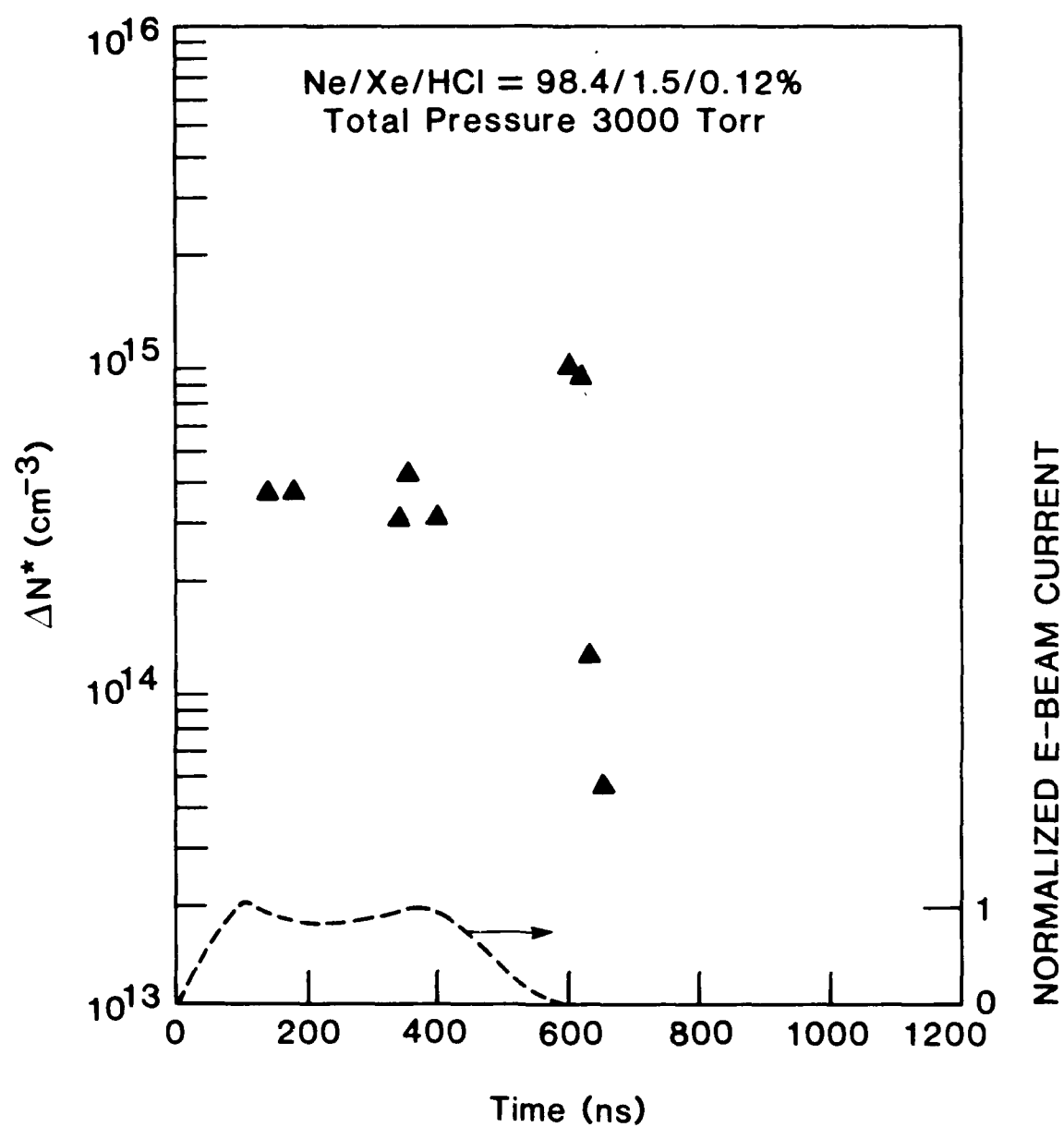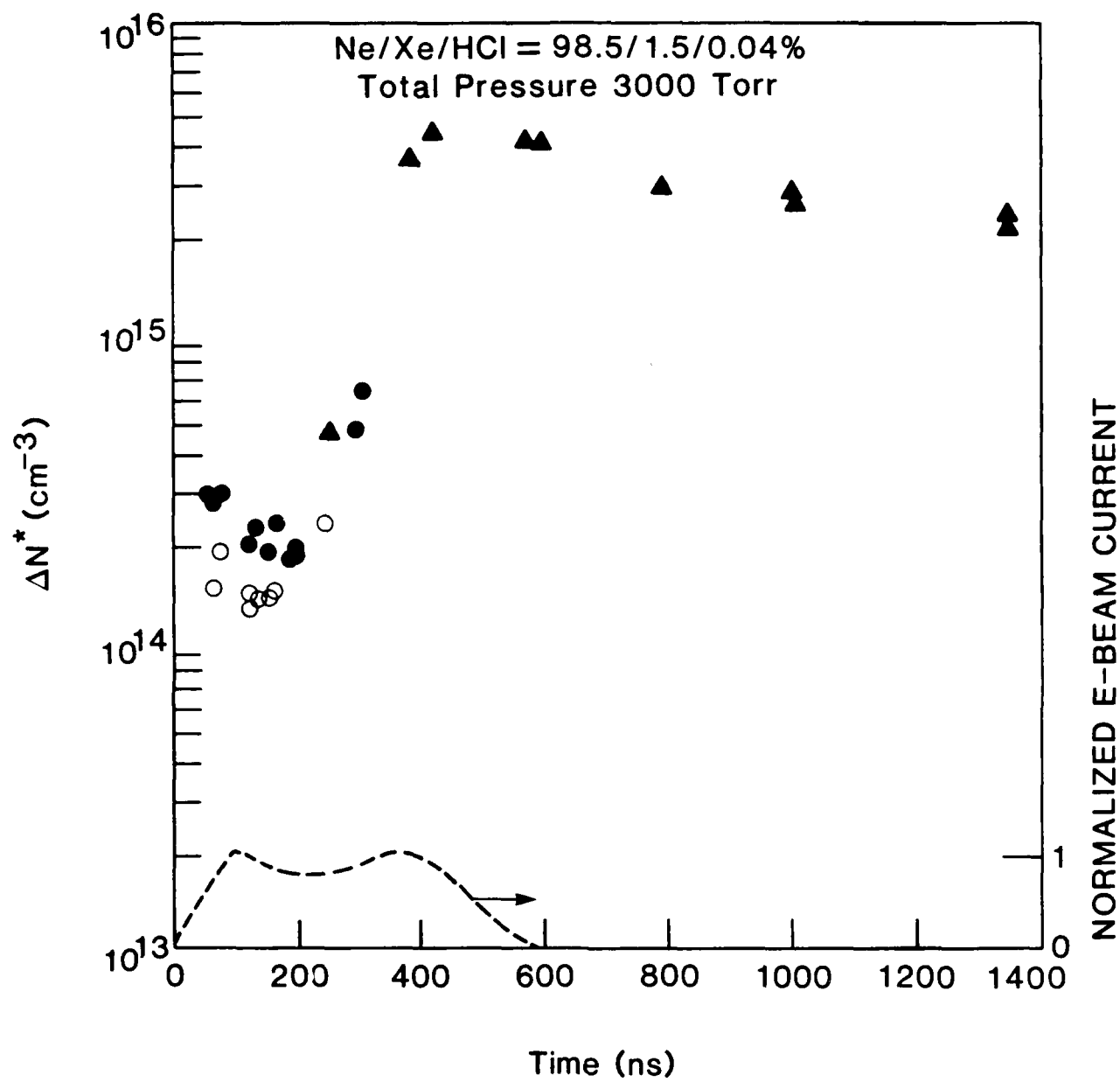NORMALIZED E-BEAM CURRENT

1

0

0   1   2   3

TIME (μs)
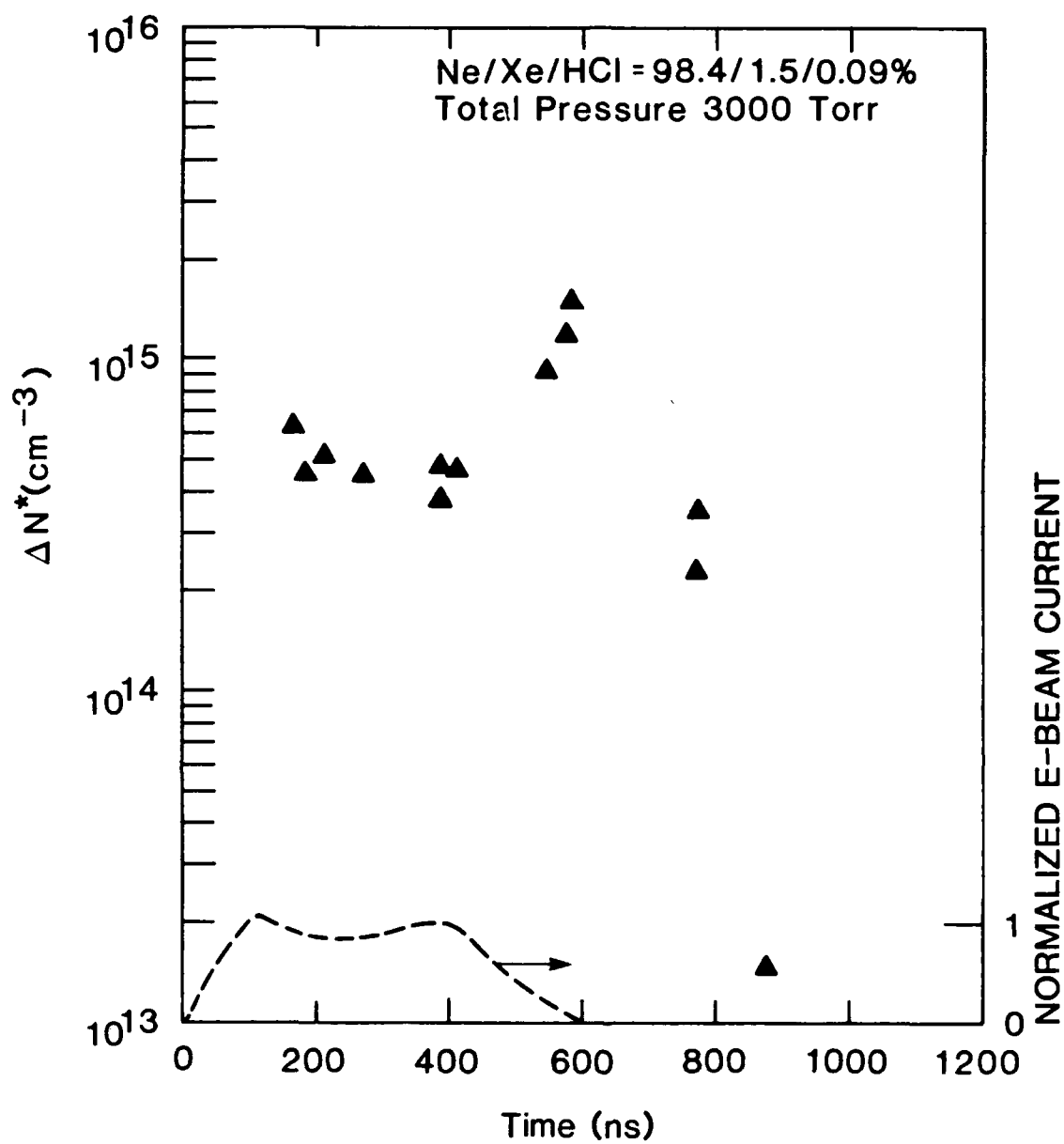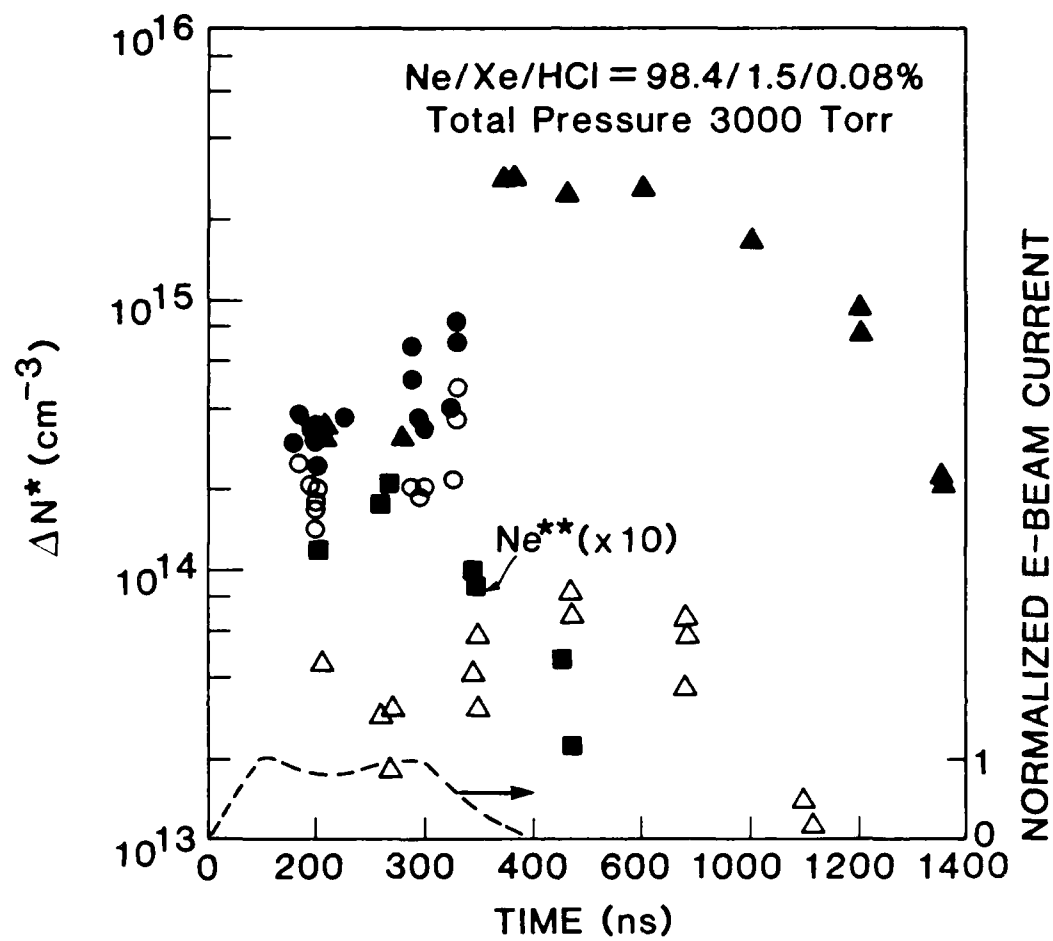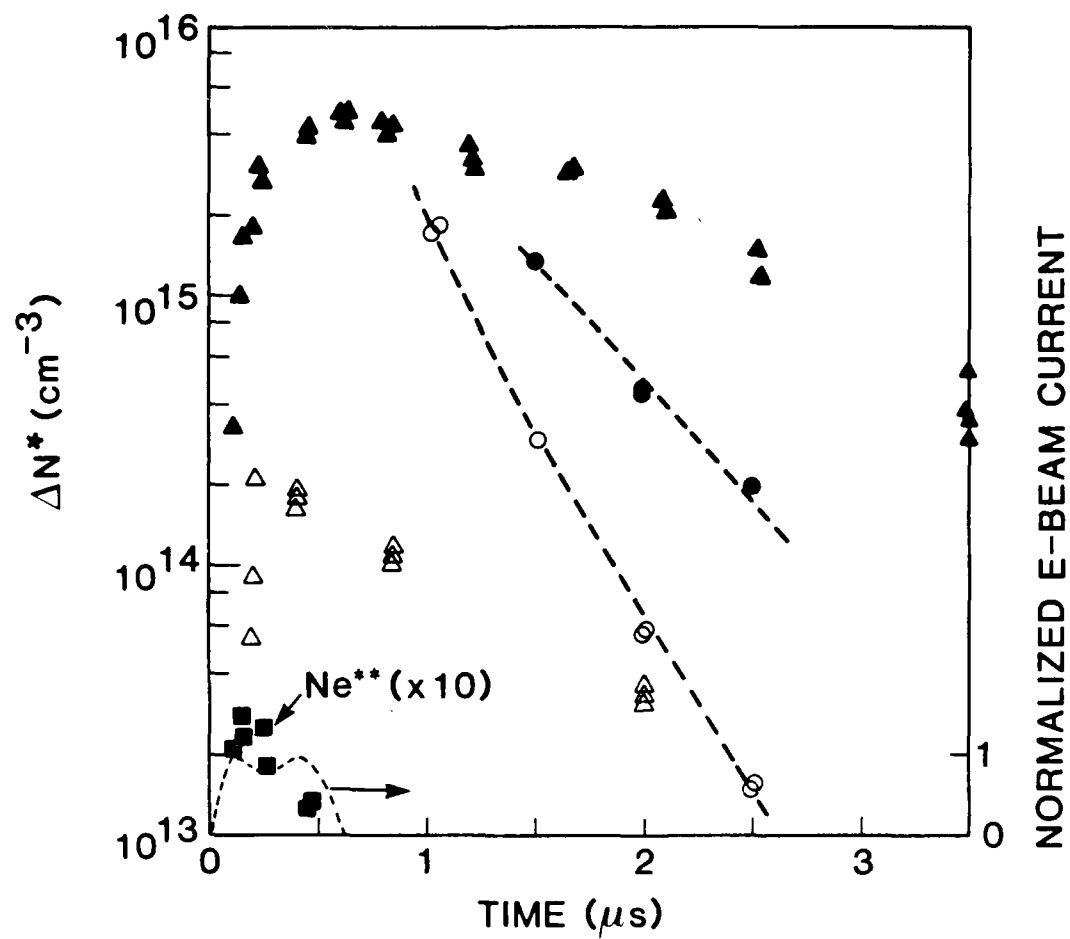
07 15649
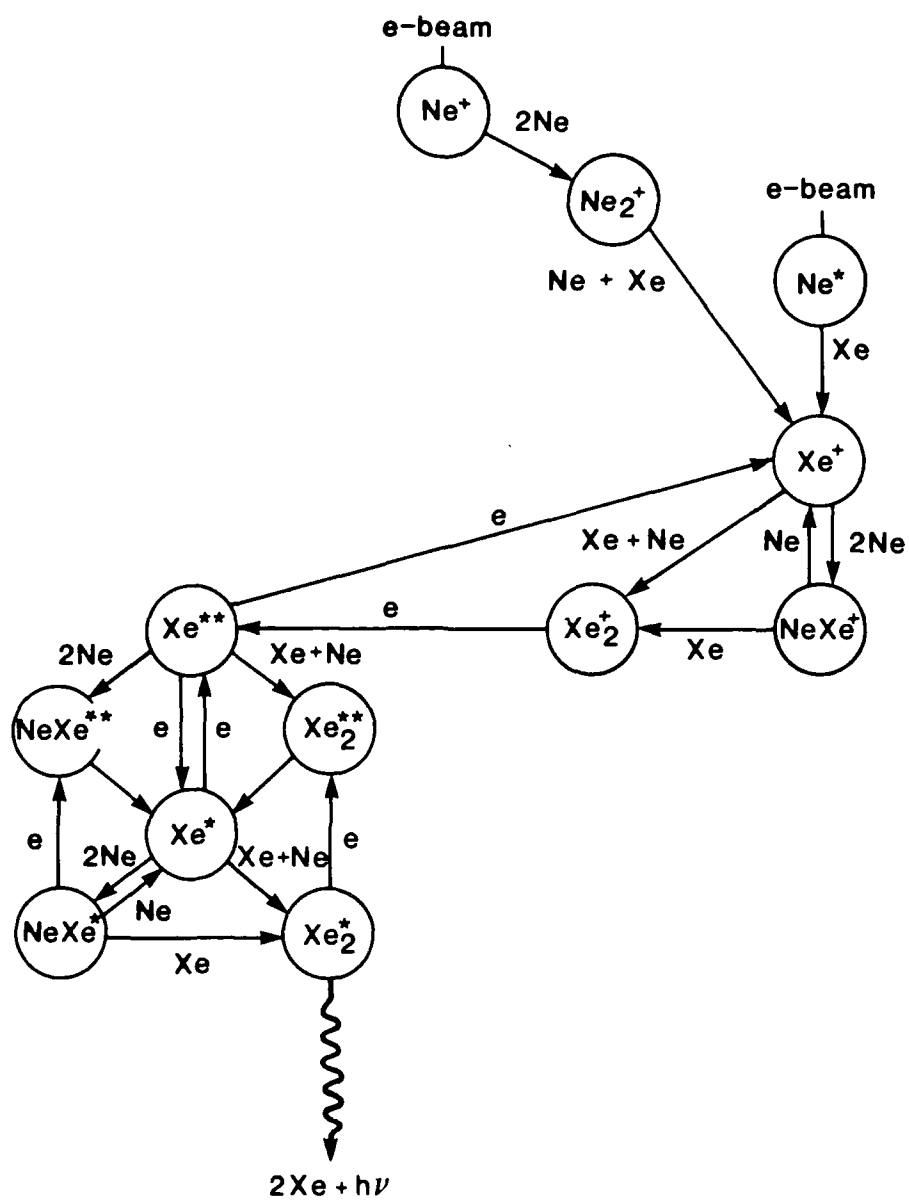
Figure 9

Figure 10
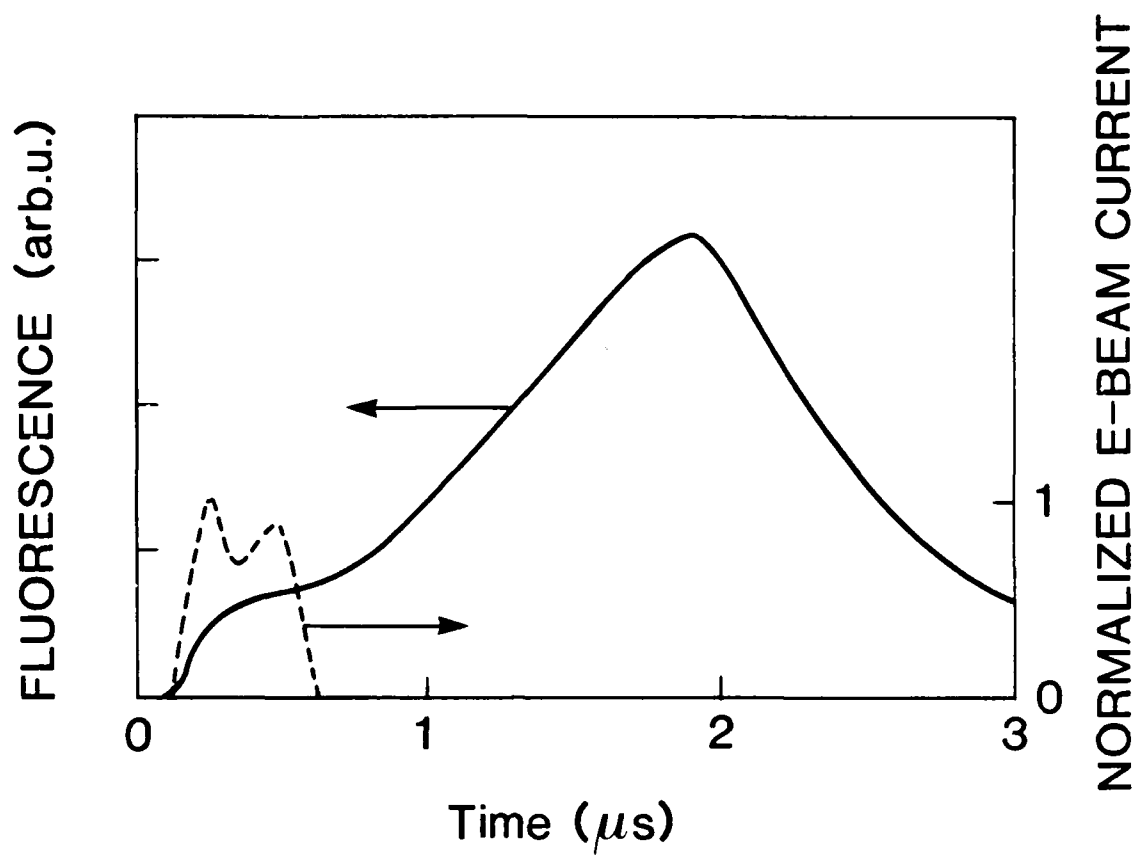
Figure 11
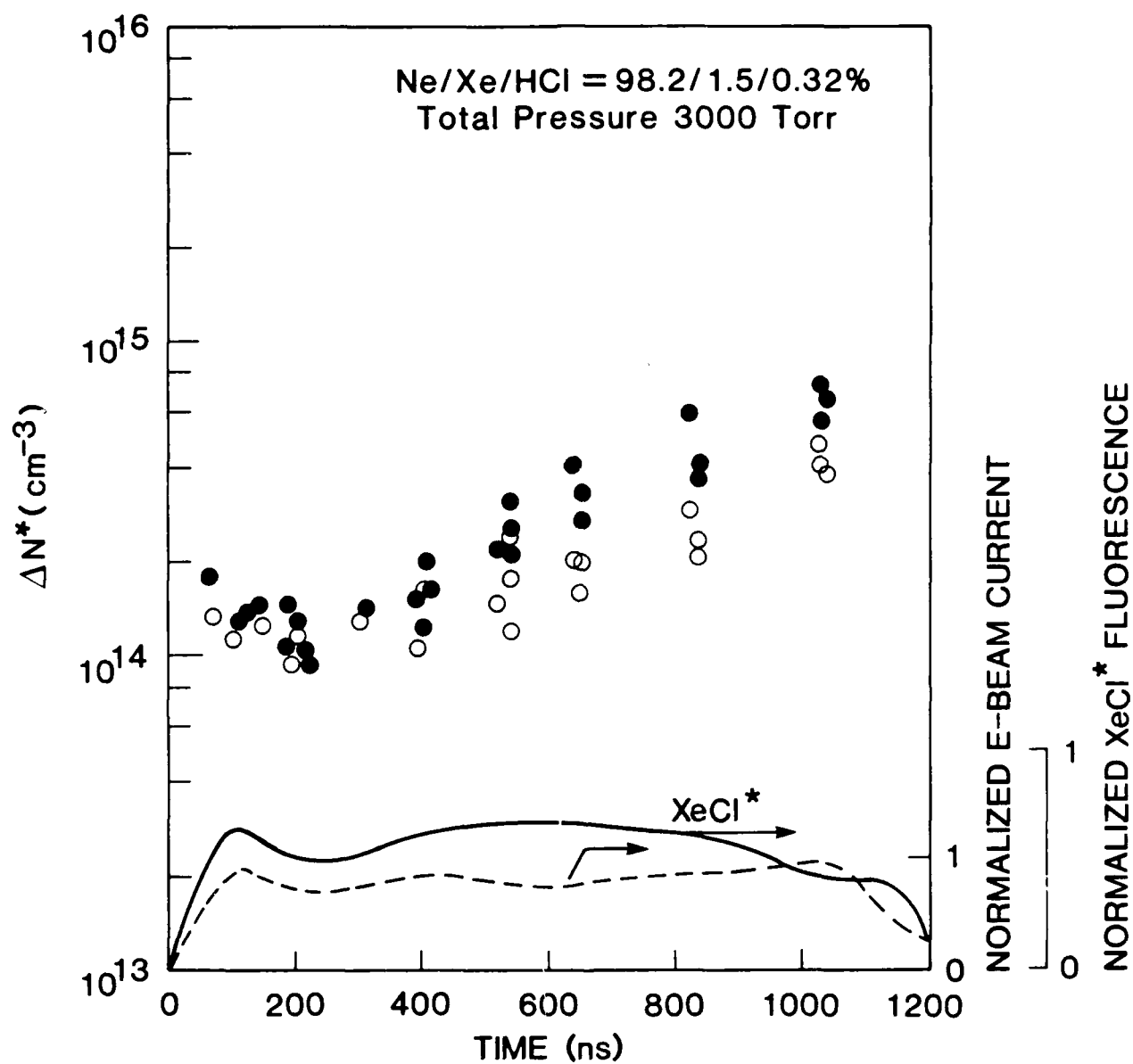
Figure 12
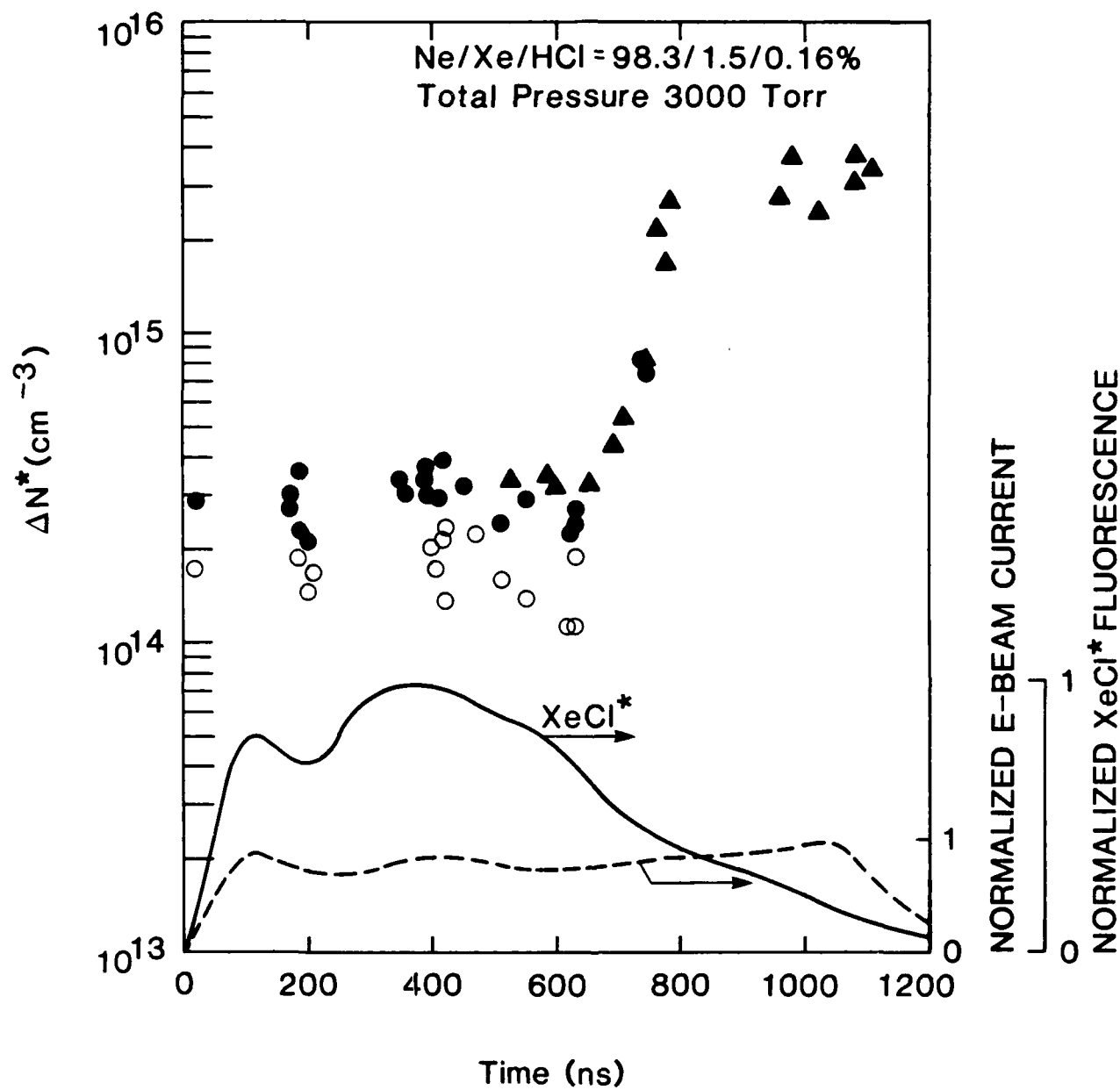
Figure 13
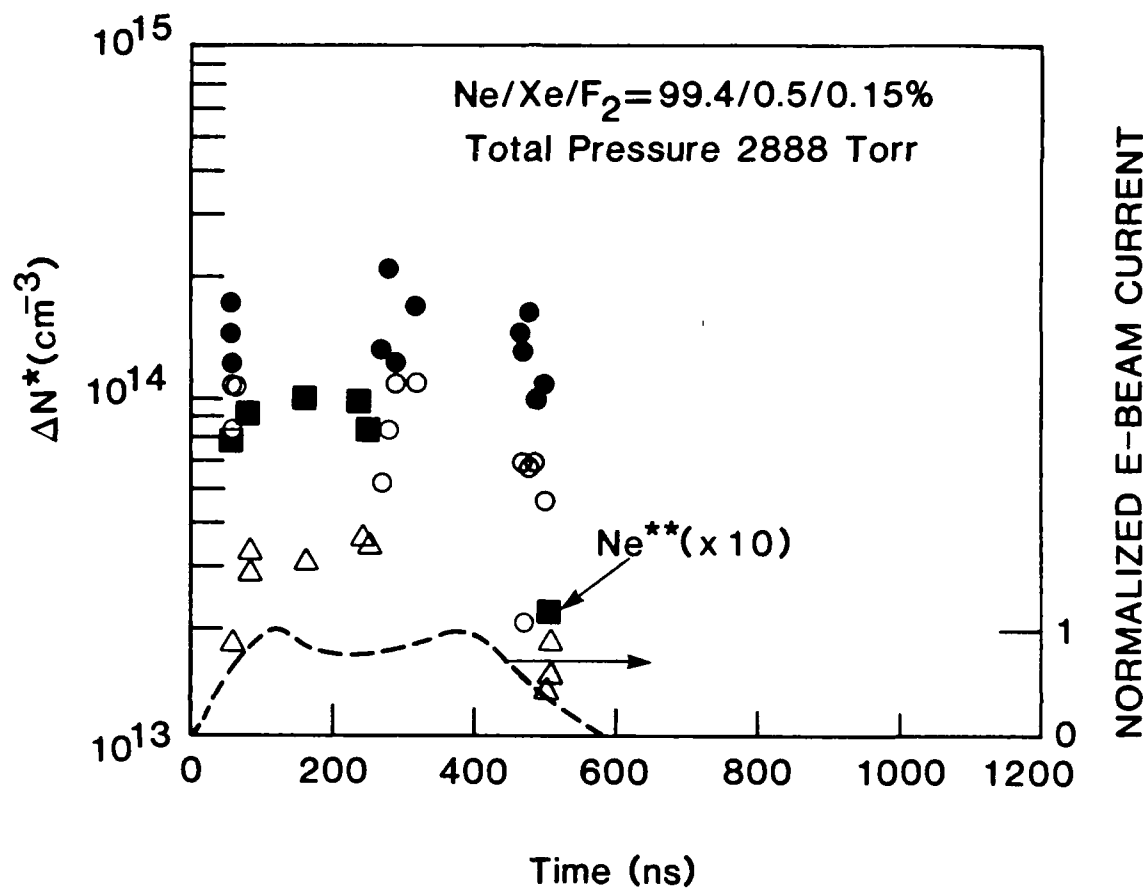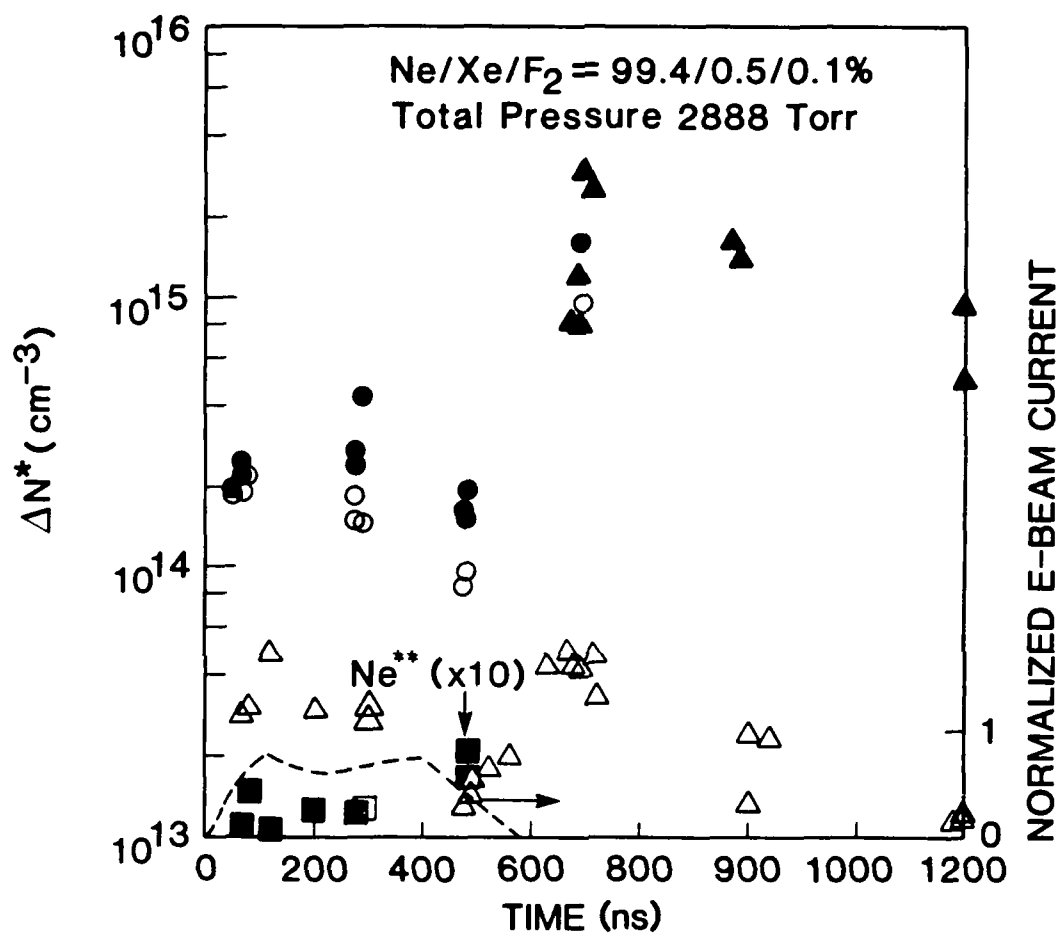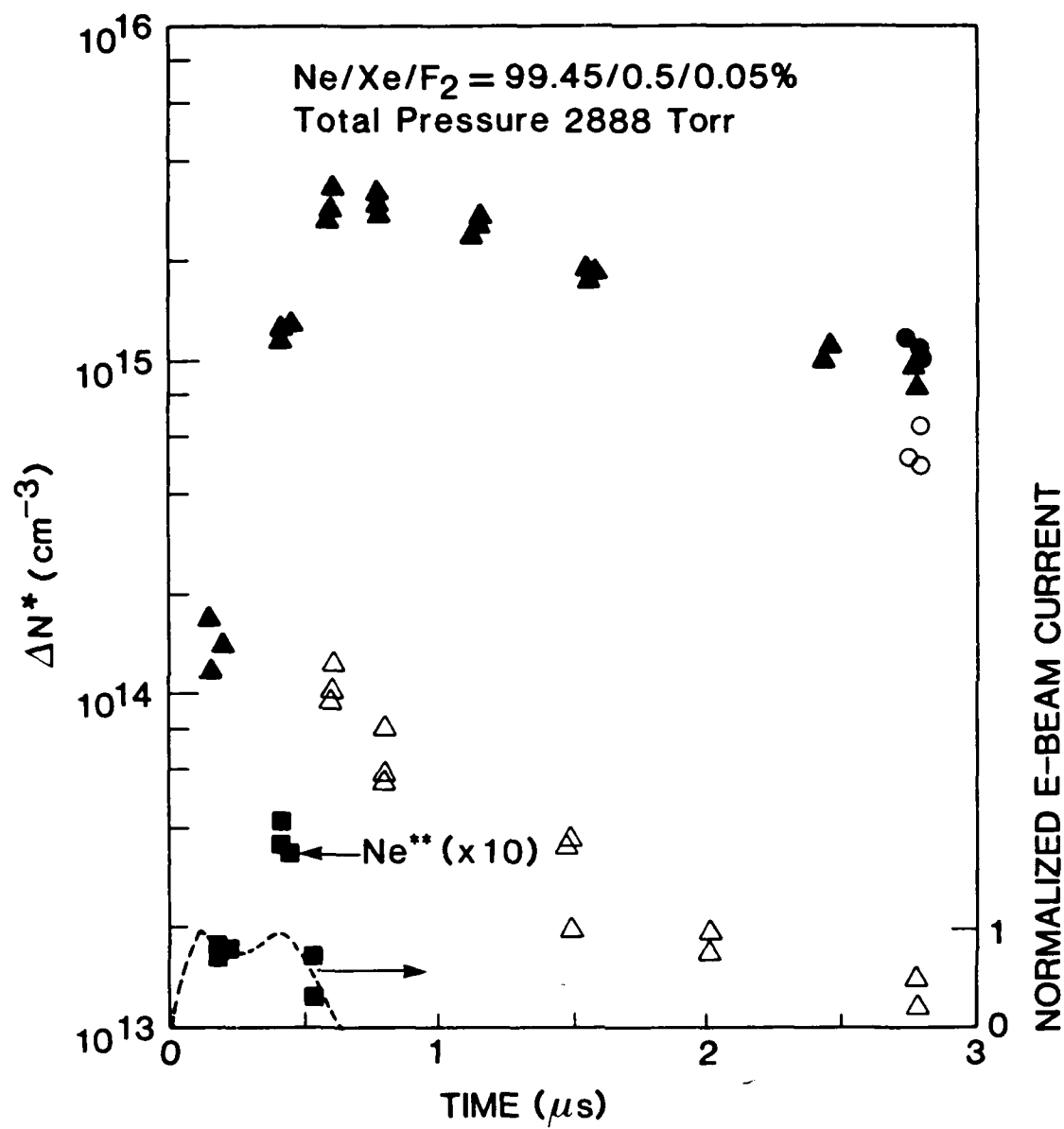
44

Figure 14

Figure 15

Figure 16

47

High-Energy Electron Distribution

in

Electron-Beam Excited Ar/Kr and Ne/Xe Mixtures

F. Kannari and W. D. Kimura

Spectra Technology, Inc.

2755 Northup Way

Bellevue, Washington 98004-1495

ABSTRACT

The electron energy distribution in electron-beam (e-beam) excited Ar/Kr and Ne/Xe gas mixtures is examined in detail. The binary rare gas mixtures are similar to those used in excimer lasers. Cooling processes for the secondary electrons generated in the gas mixture plasma by the e-beam are calculated using a reduced Boltzmann equation in which elastic and electron-electron collisions for electron energy distributions above the first excitation threshold of the rare gas are ignored. During the calculations for the Ar/Kr and Ne/Xe mixtures, all electron related reactions and the interaction between the two different rare gases in the mixture are simultaneously considered. The high energy secondary electrons produce a steady-state distribution within a very short time; however, it is found that the distribution is not Maxwellian. W-values [eV/electron-ion pair] and

yields of rare-gas excited states calculated from the steady-state high-energy
electron distribution show a dependence on the mixture composition, especially
for mixtures with low concentrations of the minor rare gas. This implies that
the practice in excimer kinetics models of using the W-values determined from
pure rare gases is not entirely accurate.

I. INTRODUCTION

Most of the ions and excited species in electron-beam (e-beam) generated plasmas are formed either directly by the primary and hot secondary electrons, or by dissociative recombination of electrons with molecular ions or attaching species. Therefore, for e-beam pumped gas lasers, the kinetics role of both the electrons and the heavy particles are very important with regard to understanding the plasma physics.

The motivation of this paper arises from recent measurements of the time-dependent electron density in e-beam pumped rare-gas halide lasers[1-2]. The results show considerably higher electron densities than that estimated[3] using a typical value for the rate constant for dissociative attachment by a halogen, and using a typical rare gas W-value (the energy expended to form an electron-ion pair). A detailed model calculation[4], assuming a Maxwellian distribution for the secondary electrons in conjunction with an energy balance equation, also gives lower electron densities. To help understand these differences requires a more careful examination of the electron energy distribution. The objective of this work is to describe in detail the electron distribution characteristics in these laser plasmas.

To understand the issues related to the usual development of the kinetic models, it is helpful to review the energy flow channels for the electrons in an e-beam pumped laser mixture. First, the primary electrons from the e-beam directly produce ions, secondary electrons, and excited molecules. This

process is usually accounted for in the models by using a stopping power constant for the gases.[5] The hot secondary electrons are cooled by collisions with gas molecules and produce more ions and excited states. This process is typically modeled by using W-values and the yield of excited states relative to the ion formation.[6-7] The W-value is generally higher (typically a factor of 1.7-1.8) than the ionization potential of the atom. The primary electrons from the e-beam and the hot secondary electrons are usually treated collectively as the e-beam source. Because the preceding two processes are very fast (<100 ps for typical rare-gas halide laser mixtures), the formation of the ions and excited states by the e-beam source has been treated as an instantaneous process by simply using gross macroscopic values for the stopping power constant and W-values.

The cold secondary electrons redistribute their energy through slow electron reactions such as dissociative attachment with the halogen, excitation and ionization of excited states, recombination with positive ions, elastic collisions with neutral gases, superelastic collisions, and electron-electron collisions. This redistribution can be calculated by solving the Boltzmann transport equation, as is usually done for discharge pumped lasers. However, in models of e-beam pumped lasers, the distribution of the secondary electrons is many times either ignored or assumed to be Maxwellian. This may lead to an inaccurate estimation of the attachment reaction rate of the halogen gas, and the ionization rates by the hot secondary electrons in populations above the ionization threshold energy.

4

This paper concentrates primarily on the high-energy part of the electron distribution function. The high-energy electron distribution is the effective driving term of the Boltzmann equation for the low-energy electron distribution. Calculations of the high-energy electron distributions have been made by Elliot and Green[8], and Bretagne, *et al.*,[9] but these calculations were limited to pure rare gases of argon or xenon. Since most rare-gas halide lasers use a mixture of different rare gases with a trace of halogen, the calculations need to include the distributions of inelastic collision cross-sections for each of the rare gases as a function of energy. Because competition among the inelastic collision processes (to be explained later) between different rare gases can be accounted for only through a simultaneous calculation, the electron energy distributions and the W-values of mixtures cannot be estimated simply from the results of pure rare gases. This paper presents calculations for mixtures of Ar/Kr and Ne/Xe, which are typical rare gas combinations for e-beam excited KrF (248 nm), and XeCl (308 nm) or XeF (353 nm) lasers, respectively.

Section II gives a brief description of our model. Section III presents the calculated results of the high-energy electron distributions for pure rare gases of Ar, Kr, Ne, Xe, and for mixtures of Ar/Kr and Ne/Xe. W-values are calculated for mixtures and compared with those of pure rare gases. The yields of excited species and their dependence on the mixture are calculated. Also presented are the formation rates of various ions and excited species produced either by direct e-beam processes or by the steady-state high-energy

electron distribution. Conclusions are given in Section IV.

II. MODELING AND DERIVATION OF RATE CONSTANTS

Our model development begins by using the same basic calculation
procedure as presented by Bretagne, *et al.*[9] The distribution of electron
energy is derived from a reduced Boltzmann equation with no elastic and
electron-electron collisions:

$$\frac{\partial f(\epsilon,t)}{\partial t} = \left[\frac{\partial f}{\partial t}\right]_{in} + I(t)S\left(\epsilon_p,\epsilon\right), \qquad [1]$$

where $f(\epsilon,t)$ is the electron energy distribution function of energy ϵ at a
time t. The first term on the right-hand side corresponds to the production
and removal of electrons with energy ϵ by inelastic collisions (ionization,
and excitation), recombination, and superelastic de-excitation; and the second
term corresponds to the production rate of secondary electrons with energy ϵ
by primary electrons in the e-beam with energy ϵ_p. $S(\epsilon_p,\epsilon)$ is the
corresponding differential ionization cross-section, and I(t) is a value which
is proportional to the current density of the e-beam.

The effects of electron-electron collisions can be neglected as long as
the collisional rates of the inelastic reactions are much higher than the
electron-electron collision rate. The value $\Phi(\epsilon)$ is defined by the ratio of
the electron-electron collision rate to the inelastic collision rate:[9]

6

$$\Phi(\epsilon) = \frac{(\partial f/\partial t)_{ee}}{(\partial f/\partial t)_{in}}$$

$$= \frac{n_e}{n_o} \frac{\pi e^4 \ln \Lambda}{\epsilon^2 \; Q_{in}(\epsilon)}, \tag{2}$$

where n_e is the secondary electron density, n_o is the rare gas density, Q_{in} is the inelastic collision cross-section, and Λ is the Spitzer parameter.[9] The value of $\Phi(\epsilon)$ is less than 10^{-3} for electrons whose energies are higher than the first excitation threshold of the major gas constituent. Therefore, as long as the minimum energy considered is higher than the first excitation threshold, the influence of electron-electron collisions can be neglected. However, if the concentration of the minor rare gas is extremely low, then the formation of its ion and excited states can be affected by electron-electron collisions. Hence, the electron cooling processes involving inelastic collisions with the minor rare gas must be treated as a slow process if the rare gas concentration is low (e.g. <1%). This will be discussed later. In this work, the energy distribution above the first excitation threshold of the major rare gas is calculated as a steady-state high-energy electron distribution function.

Similarly, the elastic collision term can be neglected as seen by evaluating the function $\theta(\epsilon)$:

$$\theta(\epsilon) = \frac{(\partial f/\partial t)_{el}}{(\partial f/\partial t)_{in}}$$

7

$$= 2 \left(m_e/M \right) \frac{Q_{el}(\epsilon)}{Q_{in}(\epsilon)} \quad (\ll 1), \qquad\qquad [3]$$

where m_e/M is the electron to rare gas mass ratio and Q_{el} is the elastic collision cross-section. Contributions of inelastic collisions involving excited molecules are ignored, due to the relatively low density of these molecules, during the calculation of the high-energy secondary electron distribution.

The energy distribution of the secondary electrons is calculated using differential ionization cross-sections. Peterson and Allen[10], Green and Sawada[11], and Bretagne, *et al.*[9] have proposed empirical formulas for M-shell ionization of argon gas. For other rare gases, the formulas given by Green and Sawada[11] are available. The results of calculating the total ionization cross-sections and energy losses for various incident electron energies using the different empirical formulas for argon gas are shown in Table I. Although the three different formulas give similar values for the total ionization cross-sections over a wide range of incident electron energies, the energy loss values calculated by Peterson and Allen's formula are significantly larger than the others. This is because their formula predicts larger differential ionization cross-sections for the high energy secondary electrons which leads to a greater energy loss. For comparison, the energy loss values calculated using Bethe's stopping power theory[5], which provides a macroscopic calculation of energy loss values for high energy electrons, are also listed in Table I. Even the values calculated from Peterson and Allen's formula are lower than those obtained from Bethe's theory.

8
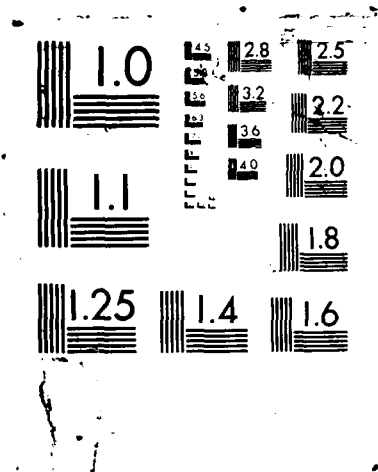
The discrepancy between the values calculated by Bethe's formula and those of the empirical differential ionization cross-sections can be explained as a result of energy loss caused by inner shell ionizations. The L-shell ionization loss calculated from an empirical differential ionization cross-section proposed by Peterson and Allen[10] is ≈ 0.5 eV-$\mathring{A}^2$ for a 10^4 eV primary energy, which is 6% of the M-shell ionization loss given in Table I. Recently, Bretagne, *et al.*[12] have also reported an empirical differential ionization cross-section for the L-shell of argon, and an energy loss of 3 eV-$\mathring{A}^2$ is obtained from their formula for a 10^4 eV primary energy. Combining this L-shell ionization loss with the M-shell ionization loss of 5 eV-$\mathring{A}^2$, listed in Table I for Bretagne, *et al.*, yields a total ionization loss of ≈ 8 eV-$\mathring{A}^2$. This is close to the value calculated from Peterson's formula (see Table I), but still $\approx 20\%$ lower than Bethe's loss value.

Bethe's formula calculates the energy loss directly and is generally in good agreement with experiments; whereas the method using the empirical formulas for the differential ionization cross-sections is an indirect approach and is sensitive to the values of the cross-sections at high secondary electron energies. The empirical formulas all tend to underpredict the differential ionization cross-sections for secondary electron energies $\gtrsim 100$ eV.[9] This leads to an underprediction of the stopping power.

These disagreements regarding the stopping power obtained from the empirical differential ionization cross-sections become more pronounced for Kr and Xe. When the empirical formulas proposed by Green and Sawada[11] are used,

the calculated energy loss, at a 10^4 eV primary energy, is lower than Bethe's value by ≈46% and ≈44% for Xe and Kr, respectively. This is because the inner shell ionization rate becomes larger for high Z atoms. The total ionization cross-section for inner shell ionization is very small compared with the outer shell; however, its contribution to the stopping power is significant due to its high ionization energy. Unfortunately, to our knowledge, differential ionization cross-sections for Kr and Xe are not available.

Although the empirical formulas for the differential ionization cross-section suffer from inaccuracies at high secondary electron energies, they are still useful for estimating the W-value of a gas. The W-value is given by the ratio of the rare gas ion density divided by the stopping energy for electrons in the gas. The empirical formulas tend to underpredict the stopping power, but they also tend to underpredict the ion density by approximately the same amount. This is because the ion density prediction initially uses the electron distribution calculated for the primary electrons, but this same distribution relies on the stopping power prediction. Peterson, *et al.*[10] and Bretagne, *et al.*[9,13] have found that the net formation efficiencies of ions and excited states are nearly constant for initial electron energies greater than ≈50 eV [net formation efficiency is defined here as the ratio of the ionization (excitation) energy divided by the total energy loss per ion (excited state) formed]. This implies that the ion or excited state formation efficiency is relatively independent of the shape of the electron distribution during the continuous process of energy cooling. Hence, the ratio of the ion density to the stopping power using the empirical formulas is approximately

equal to the ratio of the real ion density to the real stopping power.

This assumption was validated by computing the W-value using the three different empirical formulas: 1) Peterson and Allen[10], 2) Bretagne, *et al.*[9] without L-shell ionization, and 3) Bretagne, *et al.*[12] with L-shell ionization. The obtained W-values for pure argon are 29, 25, and 27 eV, respectively. Hence, despite the large differences among values for stopping power (of order 50%), the predicted W-values are within 15% of each other. Moreover, the formation efficiencies of the excited species are also approximately equal for all three cases. In this paper, it is assumed that the other rare gases also follow this general trend.

In order to estimate the secondary electron density in a pure rare gas, it is necessary to correct the density calculated using the energy loss result from the empirical formulas by multiplying the density by the ratio of the stopping power predicted by Bethe's formula over the stopping power predicted by the empirical formulas. For this method of correction to be valid it is necessary that the electron energy distribution be independent of the excitation or deposition rate. This is true when the effects of electron-electron collisions can be neglected, which, as was discussed earlier, is true for the cases studied here.

As mentioned, the preceding method for calculating the secondary electron density and energy distribution is applicable to the case of a pure rare gas. When the medium consists of a mixture of gases, the situation

11

becomes considerably more complex because the energy losses predicted by both Bethe's formula and the empirical ones depend on the type of gas.

The low total ionization cross-section of the inner shell means that the density of inner shell ions is very low compared to outer shell ions. However, the inner shell ions can eject Auger electrons with high enough energy to produce additional excitations and ionizations.[14-15] Therefore, the inner shell ionization process effectively corresponds to the production of Auger electrons at a rate defined by the inner shell total ionization cross-section. The produced Auger electrons are cooled through the formation of ions and excited atoms at probabilities given by the reaction rates at the energy of the Auger electrons. The ratios of the ionization cross-sections for Ar and Kr at 10^4 eV (primary electron energy) and 200 eV (approximate Auger electron energy in Ar) are similar. Hence, Auger electrons produce Ar^+ and Kr^+ at approximately the same probability as the primary electrons. It is therefore possible to account for the effects of Auger electrons by increasing the effective total cross-section of the primary electrons.

In this paper, rather than attempt to compensate for the ionization cross-section differences at the high energy part of the electron distribution, by assuming an empirical differential ionization cross-section for the inner shell, a simpler approach is taken. The total ionization cross-sections given by the empirical formulas and the excitation cross-sections for each of the rare gas species are multiplied by a constant factor such that the resultant energy loss agrees with Bethe's theory for rare gas mixtures.

12

The preceding procedure is performed only on the differential ionization cross-sections for the primary electrons. Thereafter, this compensation procedure does not have to be applied to the hot secondaries and their cooler offspring. Instead, the uncorrected empirical formulas are used to predict the energy loss within a computational cell of the medium as the hot secondaries produce additional but cooler electrons. Since the electron energy is conserved within the cell, the error in the energy loss prediction does not cause an error in the energy balance within the cell.

The total ionization cross-sections obtained from the empirical differential ionization cross-sections for the outer shell agree well with experimental values.[16] Therefore, minimal error is introduced by ignoring the inner shell ionizations when calculating the ionizations and excitations occurring in mixtures of rare gases, except for the error caused by the change in the secondary electron distribution during the continuous process of energy cooling. Since, as was shown for pure argon, this latter error tends to be very small in a pure rare gas, it is assumed in this paper that this trend is also true for rare gas mixtures. This last assumption, however, has not been validated.

For the excitation cross-sections, the expressions given by Peterson and Allen[10] for argon gas are used. For neon, krypton, and xenon, the empirical cross-sections of Ganas and Green[17] and the formula proposed by Vriens and Smeets[18] are used for optically allowed transitions. At sufficiently large electron energies, the cross-section of optically allowed excitations

$Q_{allow}(\epsilon)$ approaches the form :

$$Q_{allow}(\epsilon) \approx K_1 \frac{\ln(\epsilon)}{\epsilon}, \qquad [4]$$

where K_1 is a constant. Since there is no data available (except for argon), the cross-section for the optically forbidden np-(n+1)p transitions are assumed to be of the form:

$$Q_{forbid}(\epsilon) = K_2 \frac{1 - \epsilon_{th}/\epsilon}{\epsilon}, \qquad [5]$$

where K_2 is a constant, and ϵ_{th} is the threshold energy for the excitation. At sufficiently high energy, Eq.(5) approaches K_2/ϵ. During calculations in pure rare gases, the values of K_2 for neon, krypton, and xenon are adjusted so as to yield W-values consistent with the experimentally determined values.[6,7] The cross-section distributions for inelastic collisions used during the calculations are shown in Figs. 1 and 2 for Ar/Kr and Ne/Xe mixtures, respectively. The electronic classifications and their energy levels which are included in the model are listed in Table II.

The results presented in this paper are for a fixed primary electron energy of 10 keV. Of course in real laser systems the e-beam energy is typically 100's of keV to several MeV. Nonetheless, calculations of the energy dependence to create ions and excited states from that part of the distribution above 10 keV yield similar results even at 1 MeV energy levels.[9,10,13] Thus, the assumption can be made that the ionization and excitation efficiencies for primary electron energies above 10 keV is constant

and equal to those obtained at 10 keV. This approximation allows the number of secondary energy segments considered in the model to be minimized, thereby reducing the computation time.

The results presented in this paper are for a constant excitation rate. Changes in the current density affect the overall magnitude of the distribution function [$\#/cm^3$ eV] without affecting the overall shape of the high energy region. During the calculations presented next, the system represented by Eq.(1) is simultaneously integrated over ≈ 250 energy segments using a fourth-degree Runge-Kutta method. A provision for increasing the widths of the energy intervals with increasing energy is introduced to reduce the number of segments required and to keep the accuracy high during calculations at the lower energy levels.

III. RESULTS AND DISCUSSION

A. Distribution of High-Energy Secondary Electrons

Depicted in Fig. 3 is the temporal evolution of the electron energy distribution calculated for a 3000 Torr pure neon case. The absolute number density of the secondary electrons shown in this figure has already been adjusted to account for the error in stopping power given by the empirical formulas for the differential ionization cross-sections against that calculated by Bethe's theory. The calculation continued until the electron

15

densities around 20 eV and greater reached constant values. This final distribution represents the steady-state distribution. The electron densities tend to reach steady-state values from the direction of the higher energy side. This is because the densities at each energy are achieved by a balance between a formation term, which includes direct formation by the primary electrons and by electrons at high energies, and a loss term due to inelastic collisions by neutrals and electrons.

Note how in Fig. 3 the steady-state distributions rapidly decrease beyond the threshold of the first excitation (16.7 eV) of neon. Densities lower than ≈17 eV are plotted by a dashed line to indicate an uncertainty in the calculation for this part of the curve. This is because the densities at these lower energies are sensitive to slow electron reactions (e.g., recombination, electron-electron collisions, ionization and excitation of excited molecules, and superelastic de-excitations), which have not been included in the calculation yet. Detailed results for the low-energy electron distribution are reported elsewhere.[19] When calculating the distribution function for the lower energy part, the previously obtained steady-state distribution of the high energy part ($\epsilon > 17$ eV) is used as the effective e-beam source (i.e., the driving term in the Boltzmann equation for the low-energy electrons). Formation rates of ionized or excited species and of lower energy electrons are calculated from this e-beam source, and are discussed in more detail in Section III(B).

The normalized steady-state distribution of the high energy tail for 3000 Torr neon is shown in Fig. 4. This is compared with a Maxwellian distribution at a characteristic temperature kT_e (= 2/3 $<\epsilon>$) of 4.6 eV, which corresponds to the average energy of the steady-state distribution. The steady-state distribution has a considerably larger number of electrons at energies >40 eV.

The mean energy required for the formation of an ion-electron pair can be estimated from the ion formation rate, calculated using the steady-state distribution, ratioed to the e-beam deposition rate. This value effectively corresponds to the W-value. The energies required for the formation of various excited states (also referred to as the W-values for excited states) are obtained in the same manner. The formation of a neon ion-electron pair requires 38 eV, and Ne^*, Ne^{**}, Ne^{***}, and Ne^{****} require 1.6×10^2, 1.3×10^2, 1.5×10^3, and 9.0×10^3 eV for formation, respectively (see Table III). This calculated W-value of 38 eV is very close to the reported value of 36.6 eV.[20] The yield of total excited states created during the formation of one ion-electron pair is ≈0.56. This value is significantly higher than the value of 0.33 reported by Blauer, et al.[21] They obtained this value from the ratio of excitation and ionization cross-sections, and ignored the highly excited states (Ne^{**}, Ne^{***}, Ne^{****}). Jancaitis[22] obtained a ratio of 0.47 by solving the Fowler equation[23,24] including several excitation levels. The energies required for the formation of ions or excited states calculated from the Fowler equation were obtained during the cooling processes. This means Jancaitis' calculation used a slightly different definition from our model.

However, it is clear that a considerable number of excited states at higher levels are created together with the excited state at the first excitation level. If collisions with neutral particles efficiently deactivates higher level excited states to the first or second excitation levels, this would significantly impact the laser kinetics.

The calculated secondary electron distributions for 760 Torr xenon are shown in Fig. 5. Because of xenon's larger cross-section for inelastic collisions, the steady-state distribution is achieved in a shorter time than the 3000 Torr neon case, even at low pressures. The distribution is, again, truncated near the threshold of xenon excitation and a large population of electrons reside in the high energy tail. The calculated W-value is 22 eV, which is in good agreement with the reported value of 21.7 eV.[20] Energies required for the formation of excited states are 1.3×10^2, 1.2×10^2, and 9.1×10^2 eV for Xe^*, Xe^{**}, and Xe^{***}, respectively (see Table III). The total yield of excited states during the formation of an ion-electron pair is 0.38.

Results calculated for neon gas containing 0.5% xenon at a total pressure of 3000 Torr are given in Fig. 6. The distribution has been calculated up to 100 ps; however, the distribution near the excitation threshold of Xe has not reached steady-state yet. Calculations beyond ≈100 ps require the inclusion of slow, low energy electron reactions, such as electron-electron collisions and superelastic collisions that can form hot electrons from excited states. These reactions have not been included in this

part of the calculation. Two shoulders in the shape of the distribution function can be seen near the excitation thresholds of neon and xenon. The distributions beyond about 17 eV where neon dominates have reached a steady-state and are about the same as those of pure neon shown in Fig. 4. Hence, accurate estimations of the electron energy distribution lower than the first excitation threshold of neon need to be calculated separately, with the distributions for the high energy electrons still valid using the preceding technique. This is particularly true for mixtures with low concentrations of the minor rare gas. If the partial pressure of the minor rare-gas is high (e.g., greater than a few percent), the lowest boundary of the high-energy electron distribution can be set near the excitation threshold of the minor rare gas. An example of this is demonstrated by the dotted curve in Fig. 6, which is for 5% Xe in neon at 3000 Torr.

Electron cooling in these e-beam pumped plasmas involve the following processes. Primary electrons produce neon ions and hot secondary electrons (<100 eV). These are estimated using the distributions and magnitudes of the inelastic collision cross-sections. The hot secondary electrons continue to create neon ions, thermalize in energy, and then create neon excited states and warm electrons (<17 eV). The very small concentration of xenon means the effective formation of xenon ions and excited states begins after the warm electrons have cooled down to less than the threshold of neon excited state formation. At this point the warm electrons create cool secondary electrons (<8.4 eV) during the formation of xenon ions and excited states. Slow low-energy reactions then create cold electrons (of order few eV) from the cool

19

electrons.

Typically, the ion and excited state formation of different gases in these mixtures are treated in kinetic models as individual pure gases using their respective W-values and excited state yields obtained from measurements or estimations for pure gases. This is particularly true in any of the rare-gas halide laser models excited by an e-beam. However, the secondary electrons created by collisions with different gases cannot be distinguished individually in the mixture. The electron energy distribution established by the major gas acts as an effective primary electron distribution for the minor gas. Therefore, the W-values and excited state yields obtained for mixtures must include the competition among the various inelastic collisions occurring among the different gases. These are included exactly in our calculations. For the 0.5% xenon gas mixture, W-values of 39 and 3.5×10^2 eV, for neon-ion and xenon-ion, respectively are obtained. Since the basis of the W-value calculation is the total deposition rate of the e-beam, xenon at low concentrations will have extremely high W-values.

Although it lacks any physical meaning, it is useful to calculate the W-value normalized by the fraction of e-beam energy deposited in each of the gas constituents. This is referred to as the "effective" W-value in this paper. Values of 6.3 eV and 38 eV are obtained for xenon and neon, respectively. These are the values which should be used in the laser kinetics model instead of the W-values obtained for pure rare gases. However, these values, especially for xenon, strongly depend on the minor gas partial pressure. The

same calculations are repeated for a mixture of Ne/Xe = 2850/150 Torr.

Cooling of the secondary electrons above the first excitation threshold of

xenon becomes accelerated because of the higher density of xenon. The

calculated steady-state distribution is given in Fig. 6 by the dotted curve.

It is very similar to the distribution for pure xenon despite the low xenon

pressure. For this mixture, the normalized W-value with the partitioned

deposition energy for xenon increases to 13 eV, but this is still 9 eV smaller

than the value for pure xenon. Despite the differences between the W-values,

this does not have a strong influence on the rare-gas halide excimer formation

because the dominant channel of xenon ion formation in the Ne/Xe mixtures at

low xenon concentration is Penning ionization by neon excited states and

charge transfer from neon dimer ions.

The energies required for the formation of each excited state in a 0.5%

Xe mixture are 6.4×10^2, 4.6×10^2, and 6.5×10^3 eV for Xe^*, Xe^{**}, and

Xe^{***}, respectively; and 1.7×10^2, 1.4×10^2, 1.5×10^3, and 9.2×10^3 eV for

Ne^*, Ne^{**}, Ne^{***}, and Ne^{****}, respectively. These are listed in Table III

together with the results for pure rare gases. Efficiencies calculated by the

ratio of the W-value to the ionization or excitation threshold energy are also

listed. The results of calculating the total excited state yields are:

$\sum(Xe^*/Xe^+) = 1.4$, and $\sum(Ne^*/Ne^+) = 5.3 \times 10^{-1}$. While the addition of a small

quantity of xenon to neon has only a slight affect on the total excited state

yield of neon, the total number of xenon excited states created is now larger

than the ion yield. This is because the xenon ionization must compete with

excitation of neon excited states due to the overlap of their cross-sections

in the secondary electron spectrum as shown in Fig. 2. This results in a decrease of xenon ion formation rate. Using these results, the total number of species in a 0.5% Xe mixture created by the e-beam source, which act as the precursors for rare gas halide formation, can be calculated from:

$$39 \text{ eV (LOSS)} \rightarrow 1 \text{ Ne}^+ + 0.76 \text{ Ne}^*_{total} + 0.11 \text{ Xe}^+ + 0.15 \text{ Xe}^*_{total}, \qquad [6]$$

where Ne^*_{total} and Xe^*_{total} correspond to the total population in the various excitation levels. Hence, an e-beam loss of 39 eV yields approximately 2.0 precursors. Increasing the xenon concentration to 5%, the total excited state yield of xenon relative to the ion formation decreases to 0.91 because the formation efficiency of xenon ion improves. In this case, an e-beam loss of 45 eV results in the formation of 2.5 precursors. It should be mentioned that increasing the xenon concentration tends to degrade the laser performance due to formation of triatomics.

It is difficult to accurately estimate the W-values of the minor rare gas excited states, in this case xenon, due to the fact that the distribution function near the first threshold of xenon cannot be accurately calculated by considering only the fast reactions with hot electrons. (Although the error in the values listed in this paper is negligible (<1%), the degree of error increases with decreasing concentration of the minor rare gas.) The root of the problem lies in the definition of the W-value itself. As described earlier, the cooling process that the hot secondary electrons undergo does not occur in well-defined discrete step, but is a continuous process with no clear boundary between the fast reactions occurring with hot electrons and the slow

reactions occurring with cool electrons. As an example, for the minor rare gas, the excited state formation is affected by slow reactions, such as electron-electron and superelastic collisions, which can cause a redistribution of the hot secondary electrons whose energy are larger than the excitation threshold. In this manner, the W-value of excited state formation and their relative yield are a function of the e-beam deposition rate, particularly for the minor rare gas.

Since the total electron and excited state densities, and the rate of electron-electron collision and superelastic collision are affected by the deposition rate, it should be again emphasized that the W-values and excited state yields for the minor gas in the mixture cannot be accurately determined and are obviously different from the values for a pure gas. The overall magnitude of the values calculated in this paper, however, are still valid. This observation regarding W-values suggests that the usual method for calculating the formation of ions and excited states for the minor gases in a mixture by simply using W-values and relative yields is limited by an inherent inaccuracy.

Similar calculations are repeated for 1020 Torr pure argon, 760 Torr pure krypton (Fig. 7), and various mixtures of Ar/Kr (Fig. 8). Table IV lists the calculated effective W-values and excited state yields. The overall characteristics of the distribution functions are very similar to those for neon and xenon gases. The major difference with the neon and xenon mixture is that all the threshold energies for ionization and excitation of argon and

23

krypton are very close to one another. They are located between about 10 and 16 eV. Hence, only one shoulder is seen in the distribution functions of the Ar/Kr mixtures. Since not only the cross-section for krypton ionization, but also the excitation of krypton share the same secondary electron spectrum with the excitation and ionization cross-sections for argon, the excited state yield of Kr obtained from a mixture of Ar/Kr = 1020/114 Torr is only slightly higher than that obtained in pure krypton. The number of precursors created by the e-beam source for this particular mixture is 1.7 with an e-beam loss of 29 eV.

KrF laser performance has been investigated with mixtures at high krypton concentrations.[25-29] It would be very useful from a laser kinetics modeling viewpoint to analyze the W-value and excited state yield as a function of krypton concentration. Figures 9 and 10 show calculated W-values, normalized by the partitioned deposition energy for Ar and Kr, and excitation yields of individual states relative to the ion formation as a function of the Ar and Kr concentration, respectively. The nature of the competition between the elastic collision reactions which share the same secondary electron energy spectrum change with mixture composition; hence, both the W-value and excited state yield are not unique constants, but depend on the mixture composition. Again, the accuracy of the estimations for the excited state yields drops as the minor gas concentration decreases.

B. Formation Rates of Low-energy Electrons and Various Species

As described earlier, a full Boltzmann code calculation is necessary to calculate the low energy distribution of the secondary electrons in order to obtain accurate rate constants for the secondary electron reactions. This is especially true with regard to dissociative attachment by halogen gases, which can affect the low energy part of the electron distribution.[30] The effective role of the high-energy electron distribution function is as the ionization and excitation source (referred to in this paper as the e-beam source) in the Boltzmann equation. Calculated are the formation rates and distribution of the low-energy secondary electrons and the formation rates of various species using the calculated steady-state high-energy electron distribution and the primary electrons in the e-beam. The calculation discussed in this paper used a high-energy electron distribution calculated for mixture containing 0.5% Xe in neon at a total pressure of 3000 Torr.

During the high-energy distribution calculation, the effect of the halogen gas is ignored due to its negligible contribution; however, the formation rates of the halogen ion and the excited halogen molecule are calculated. The approach used in this paper divides the entire secondary electron distribution into a high-energy part and a low-energy part with the division point at 16.7 eV corresponding to the excitation threshold of neon. This means the formation rates of the low-energy electrons and species that are described next are the rates due to the high-energy electrons above 16.7 eV and by the primary electrons.

To calculate the distribution of the low-energy electrons produced by ionization of excited states and halogen molecules, an empirical formula for the differential ionization cross-sections must be used that also gives good agreement with the total ionization cross-sections.[18,31-32] The same basic function proposed by Bretagne, et al.[9] for argon-based excited states is utilized:

$$\sigma\left(\epsilon_p, \epsilon\right) = K \left(E_H/E_i\right)^\alpha \left(E_i/\left(E_i+\epsilon\right)\right)^\alpha \left(E_i/\epsilon_p\right)^\beta \left[1 - \left(\left(E_i+\epsilon\right)/\epsilon_p\right)^\gamma\right], \qquad [7]$$

where $\sigma(\epsilon_p, \epsilon)$ is the differential ionization cross-section (in $\overset{\circ}{A}$) for a primary and secondary electron of energy ϵ_p and ϵ, respectively; E_i is the ionization energy; and E_H is the ionization energy of hydrogen. K, α, β, and γ are fitting parameters. It is found that the values $\alpha=\gamma=3$, $\beta=0.9$, and K=2.49 give fairly good agreement between the integrated total ionization cross-section and the reported values[31] for ionizations of $Ne^*(3s)$, $Ne^{**}(3p)$, $Xe^*(6s)$, and $Xe^{**}(6p)$. These same parameters are applied to Ne_2^*, Xe_2^*, and $NeXe^*$. K=0.5 with the same α, β, and γ given previously yields reasonable agreement for HCl ionization.[33]

The calculated results of the characteristic time constant $[sec^{-1}]$ for various species are listed in Table V for an excitation rate of 1.0 MW/cm^3. The actual formation rates $[sec^{-1}cm^{-3}]$ are obtainable by multiplying the densities of the parental species by these time constants. These formation rates are proportional to the e-beam deposition rate. Therefore, once the high-energy distribution and the formation rates of species has been calculated, these values can be used during the e-beam excitation by

proportionally adjusting the rates to the instantaneous e-beam energy deposition rate. It should be emphasized that during these calculations, the W-values and excited state yields are not the primary parameters needed to predict the secondary electron energy distributions.

As shown elsewhere,[19] calculation of the low-energy electron distribution requires a time-dependent Boltzmann equation, which includes electron-electron collisions, elastic collisions, and all low-energy reactions. This is solved in a manner similar to that reported by Bretagne, et al.[34] for pure argon gas and in conjunction with a detailed heavy particle kinetics code.[4]

The preceding detailed treatment is paramount when modeling the secondary electrons in e-beam produced laser gas mixtures. Not only does the non-Maxwellian distribution of the high-energy electrons affect the predictions, but also the effect of local electron loss in the energy spectrum, caused by dissociative attachment reaction with halogens, can cause significant differences in the transient concentrations of electrons and excited species, halogen consumption, and so on, from those calculated by models that assume a Maxwellian distribution. This is especially true when the e-beam deposition rate is low, and the electrons, now at relatively low density, cannot effectively create a Maxwellian distribution.

IV. CONCLUSIONS

The distribution functions of high-energy electrons in e-beam excited rare gas mixtures are calculated for the first time. The steady-state distributions for energies higher than the first excitation threshold of the major rare gas are quickly established and a relatively large number of electrons are populated in the high-energy tail as compared with a Maxwellian distribution. Competition between the various elastic collisions of the different rare gases in the mixture result in a dependence of the W-values and excited state yields on the mixture composition. Differences in the predictions for the W-values and excited state yields of the minor rare gases can be particularly large when the values for a pure rare gas are used rather than those calculated for a mixture.

REFERENCES

1. W.D. Kimura, D.R. Guyer, S.E. Moody, J.F. Seamans, and D.H. Ford, Appl. Phys. Lett., 49, 1569 (1986).

2. W.D. Kimura, D.R. Guyer, S.E. Moody, J.F. Seamans, and D.H. Ford, Appl. Phys. Lett., 50, 60 (1987).

3. F. Kannari, S.E. Moody, W.D. Kimura, in proceedings of the International Conference on Lasers '86, Orlando, FL, 1986, R.W. McMillan, Ed., (STS Press, McLean, 1987), pp. 446-452.

4. F. Kannari, A. Suda, M. Obara, and T. Fujioka, IEEE J. Quantum Electron., QE-19, 1587 (1983).

5. M.J. Berger, and S.M. Seltzer, National Aeronautics and Space Administration Report NASA SP-3012, 1964 (unpublished).

6. D. Lorents and R.E. Olson, Semi-Annual Report No.1, Stanford Research Institute, 1972 (unpublished).

7. D.C. Lorents, Physica, 82C, 19 (1976).

8. C.J. Elliot and A.E. Green, J. Appl. Phys., 47, 2946 (1976).

9. J. Bretagne, G. Delouya, J. Godart, and V. Puech, J. Phys. D:
    Appl. Phys., 14, 1225 (1981).

10. L.R. Peterson and J.E. Allen, Jr., J. Chem. Phys., 56, 6068 (1972).

11. A.E.S. Green and T. Sawada, J. Atmosph. Terr. Phys., 34, 1719 (1972).

12. J. Bretagne, G. Callede, M. Legentil, and V. Puech, J. Phys. D:
    Appl. Phys., 19, 761 (1986).

13. J. Bretagne, G. Callede, M. Legentil, and V. Puech, J. Phys. D:
    Appl. Phys., 19, 779 (1986).

14. W. Mehlhorn and P. Stalherm, Z. Phys., 217, 294 (1968).

15. J. Vayrynen, R.N. Sodhi, and R.G. Cavell, J. Chem. Phys., 79, 5329
    (1983).

16. C.B. Opal, E.C. Beaty, and W.K. Peterson, JILA Report No. 108, University
    of Colorado, Boulder, CO (1971).

17. P.S. Ganas and A.E.S. Green, Phys. Rev. A, 4, 182 (1971).

18. L. Vriens and A.H.M. Smeets, Phys. Rev. A, 22, 940 (1980).

19. F. Kannari and W.D. Kimura, "Low-Energy Electron Distribution in Electron-Beam Excited XeCl Laser Mixtures," submitted to Applied Physics Letters, Ms. No. L-0780.

20. L.G. Christophorou, <u>Atomic and Molecular Radiation Physics</u> (Wiley, New York, 1971), Chap. 2.

21. J.A. Blauer, T.T. Yang, C.E. Turner, Jr., and D.A. Copeland, Appl. Opt., <u>23</u>, 4352 (1984).

22. K.S. Jancaitis, Lawrence Livermore National Laboratory, UCRL-53465, 1983 (unpublished).

23. R.H. Fowler, Proc. Camb. Philos. Soc., <u>21</u>, 531 (1923).

24. M. Inokuti, Rad. Res., <u>64</u>, 6 (1975).

25. M. Obara, T. Fujioka, F. Kannari, and A. Suda, Proc. Soc. Photo-Opt. Instrum. Eng., <u>270</u>, 6 (1984).

26. E.T. Salesky and W.D. Kimura, Appl. Phys. Lett., <u>46</u>, 927 (1985).

27. E.T. Salesky and W.D. Kimura, IEEE J. Quantum Electron., <u>QE-21</u>, 1761 (1985).

28. F. Kannari, A. Suda, M. Obara, and T. Fujioka, Appl. Phys. Lett., 45, 305 (1984).

29. F. Kannari, M.J. Shaw, and F. O'Neill, J. Appl. Phys., 61, 476 (1987).

30. Z. Rozenberg, M. Lando, and M. Rokni, Phys. Rev. A, 35, 4151 (1987).

31. H.A. Hyman, Phys. Rev. A, 20, 855 (1979).

32. D. Ton-That and M.R. Flannery, Phys. Rev. A, 15, 517 (1977).

33. D.K. Davis (private communication).

34. J. Bretagne, J. Gogart and V. Puech, J. Phys. D; Appl. Phys., 15, 2205 (1982).

TABLE I. Comparisons of total ionization cross-section and energy-loss for argon calculated by empirical formulas and by Bethe's stopping-power theory.

	10^2 eV		10^3 eV		10^4 eV		10^5 eV	
	$\sigma_i(\epsilon)$	$L(\epsilon)$	$\sigma_i(\epsilon)$	$L(\epsilon)$	$\sigma_i(\epsilon)$	$L(\epsilon)$	$\sigma_i(\epsilon)$	$L(\epsilon)$
PETERSON, et al.[a]	3.77	105	0.99	40.3	0.16	8.46	0.021	1.44
GREEN, et al.[b]	3.11	80	0.84	28.3	0.12	4.97	0.016	0.75
BRETAGNE, et al.[c]	3.06	71	0.91	26.3	0.15	5.04	0.020	0.80
BETHE THEORY[d]	--	--	--	--	--	9.68	--	1.91

[a] See Ref. 10

[b] See Ref. 11

[c] See Ref. 9

[d] See Ref. 5

$\sigma_i(\epsilon)$: TOTAL IONIZATION CROSS-SECTION ($\overset{\circ}{A}^2$)

$L(\epsilon)$: ENERGY LOSS (eV x $\overset{\circ}{A}^2$)

TABLE II. Electronic classifications and their energy levels used in the electron distribution calculations.

ARGON	
Ar* (4s)	11.8 eV
Ar** (4p)	13.0
Ar*** (3d, 5s)	14.1
Ar**** (4d, 6s)	15.0
Ar***** (HIGHER)	15.4
Ar$^+$ (M-SHELL)	15.8

NEON	
Ne* (3s)	16.7 eV
Ne** (3p)	18.6
Ne*** (4s, 5s, 3d)	20.1
Ne**** (HIGHER)	21.2
Ne$^+$ (L-SHELL)	21.6

KRYPTON	
Kr* (5s)	10.0 eV
Kr** (5p)	11.5
Kr*** (6s, 4d)	12.2
Kr**** (HIGHER)	12.9
Kr$^+$	14.0

XENON	
Xe* (6s)	8.4 eV
Xe** (6s', 6p, 5d)	9.7
Xe*** (HIGHER)	11.2
Xe$^+$	12.1

34

TABLE III. Calculated W-values and yields of ions and metastables for neon and xenon based gas mixtures. The efficiencies are defined by the ratio of the W-value to the ionization or excitation threshold energy. The number in parenthesis corresponds to the power of 10.

SPECIES	W(eV)	YIELD	EFFICIENCY(%)
Ne = 3000 Torr			
Ne^+	3.8(1)	1	5.6(1)
Ne^*	1.7(2)	2.4(-1)	1.1(1)
Ne^{**}	1.3(2)	2.9(-1)	1.4(1)
Ne^{***}	1.5(3)	2.6(-2)	1.4
Ne^{****}	9.0(3)	4.0(-3)	0.2
Xe = 760 Torr			
Xe^+	2.2(1)	1	5.5(1)
Xe^*	1.3(2)	1.8(-1)	6.7
Xe^{**}	1.2(2)	1.8(-1)	8.1
Xe^{***}	9.1(2)	2.0(-2)	1.2
Ne/Xe = 2985/15 Torr			
Ne^+	3.9(1)	1	5.6(1)
Ne^*	1.7(2)	2.2(-1)	9.6
Ne^{**}	1.4(2)	2.8(-1)	1.3(1)
Ne^{***}	1.5(3)	2.6(-2)	1.3
Ne^{****}	9.2(3)	4.0(-3)	2.3(-1)
Xe^+	3.5(2)	1.1(-1) [1]	3.4
Xe^*	6.4(2)	6.0(-2) [5.5(-1)]	1.3
Xe^{**}	4.6(2)	8.5(-2) [7.7(-1)]	2.1
Xe^{***}	6.5(3)	6.0(-2) [5.0(-2)]	1.7(-1)

TABLE IV. Calculated W-values and yields of ions and metastables for argon and krypton based gas mixtures. The efficiencies are defined by the ratio of the W-value to the ionization or excitation threshold energy. The number in parenthesis corresponds to the power of 10.

SPECIES	W(eV)	YIELD	EFFICIENCY(%)
Ar = 1020 Torr			
Ar^+	2.5(1)	1	6.3(1)
Ar^*	1.9(2)	1.3(-1)	6.1
Ar^{**}	2.7(2)	9.5(-2)	4.9
Ar^{***}	2.9(2)	8.8(-2)	4.9
Ar^{****}	6.6(2)	3.8(-2)	2.3
Ar^{*****}	2.7(2)	9.5(-2)	5.8
Kr = 760 Torr			
Kr^+	2.1(1)	1	4.8(1)
Kr^*	1.1(2)	2.0(-1)	1.1(1)
Kr^{**}	2.0(2)	1.1(-1)	6.1
Kr^{***}	1.5(3)	1.4(-2)	8.8(-1)
Kr^{****}	4.7(3)	4.0(-3)	3.0(-1)

TABLE IV. (cont.)

Ar/Kr = 1020/114 Torr

Ar^+	2.9(1)	1	5.5(1)
Ar^*	2.2(2)	1.3(-1)	5.4
Ar^{**}	3.0(2)	9.6(-2)	4.4
Ar^{***}	3.2(2)	8.9(-2)	4.4
Ar^{****}	7.4(2)	3.9(-2)	2.0
Ar^{*****}	3.0(2)	9.5(-2)	5.2
Kr^+	1.6(2)	1.8(-1) [1]	8.8
Kr^*	6.7(2)	4.3(-2) [2.4(-1)]	1.5
Kr^{**}	1.3(3)	2.2(-2) [1.2(-1)]	8.8(-1)
Kr^{***}	1.2(4)	2.0(-3) [1.4(-2)]	1.1(-1)
Kr^{****}	3.8(4)	8.0(-4) [4.0(-3)]	3.0(-2)

TABLE V. Calculated formation rates of various species created by the e-beam source ($\epsilon > 16.7$ eV) and by 10^4 eV primary electrons for a mixture of Ne/Xe/HCl = 2980/15/4.8 Torr at an excitation rate of 1 MW/cm^3. The number in parenthesis corresponds to the power of 10.

REACTION	TIME CONSTANT (sec^{-1})
$Ne \rightarrow Ne^+$	1.8(3)
$Xe \rightarrow Xe^+$	1.8(4)
$Ne \rightarrow Ne^*$	2.9(2)
$Ne \rightarrow Ne^{**}$	4.4(2)
$Xe \rightarrow Xe^*$	2.7(3)
$Xe \rightarrow Xe^{**}$	2.6(3)
$Xe \rightarrow Xe^{***}$	7.1(2)
$Ne^* \rightarrow Ne^+$	1.0(4)
$Ne^{**} \rightarrow Ne^+$	1.8(4)
$Xe^* \rightarrow Xe^+$	1.4(4)
$Xe^{**} \rightarrow Xe^+$	2.5(4)
$Xe^{***} \rightarrow Xe^+$	1.3(5)
$Ne_2^* \rightarrow Ne_2^+$	1.2(4)
$Xe_2^* \rightarrow Xe_2^+$	1.6(4)
$NeXe^* \rightarrow NeXe^+$	1.5(4)
$Ne^* \rightarrow Ne^{**}$	1.4(5)
$Xe^* \rightarrow Xe^{**}$	2.2(5)
$Xe^* \rightarrow Xe^{***}$	7.7(3)
$Xe^{**} \rightarrow Xe^{***}$	2.2(4)
$HCl \rightarrow HCl^+$	1.2(4)
$HCl \rightarrow HCl^*(B,C)$	3.6(3)

FIGURE CAPTIONS

FIG. 1. Distributions of ionization and excitation cross-sections. Dashed curves are for krypton-based ionization and excitations. Solid curves are argon-based ionization and excitations.

FIG. 2. Distributions of ionization and excitation cross-sections. Dashed curves are xenon-based ionization and excitations. Solid curves are neon-based ionization and excitations.

FIG. 3. Temporal evolution of the high-energy electron distribution calculated for 3000 Torr pure neon at an excitation rate of 0.82 MW/cm^3.

FIG. 4. High energy tail of the steady-state electron distribution calculated for 3000 Torr pure neon. Dashed curve is a Maxwellian distribution at a characteristic temperature kT_e = 4.6 eV.

FIG. 5. Temporal evolution of the high-energy electron distribution calculated for 760 Torr pure xenon at an excitation rate of 0.41 MW/cm^3.

FIG. 6. Temporal evolution of the high-energy electron distribution calculated for a rare gas mixture of Ne/Xe = 2985/15 Torr at an excitation rate of 1 MW/cm^3. Dotted curve is the distribution

obtained at t = 100 ps for a Ne/Xe = 2850/150 Torr mixture at an excitation rate of 1.1 MW/cm^3.

FIG. 7. High-energy electron distribution at 49 ps (approximately steady state) calculated for 1020 Torr pure argon and 760 Torr pure krypton at excitation rates of 0.27 and 0.34 MW/cm^3, respectively.

FIG. 8. Steady state high-energy electron distribution calculated for rare gas mixtures of Ar/Kr = 1020/51, 1020/114, and 1020/510 Torr, at an excitation rate of 0.52, 0.57, and 0.88 MW/cm^3, respectively.

FIG. 9. Plots of W-values normalized by the partitioned deposition energy for the argon ion, and yields of excited states of argon relative to the argon ion formation in Ar/Kr mixtures as a function of argon concentration.

FIG. 10. Plots of W-values normalized by the partitioned deposition energy for the krypton ion, and yields of excited states of krypton relative to the krypton ion formation in Ar/Kr mixtures as a function of krypton concentration.
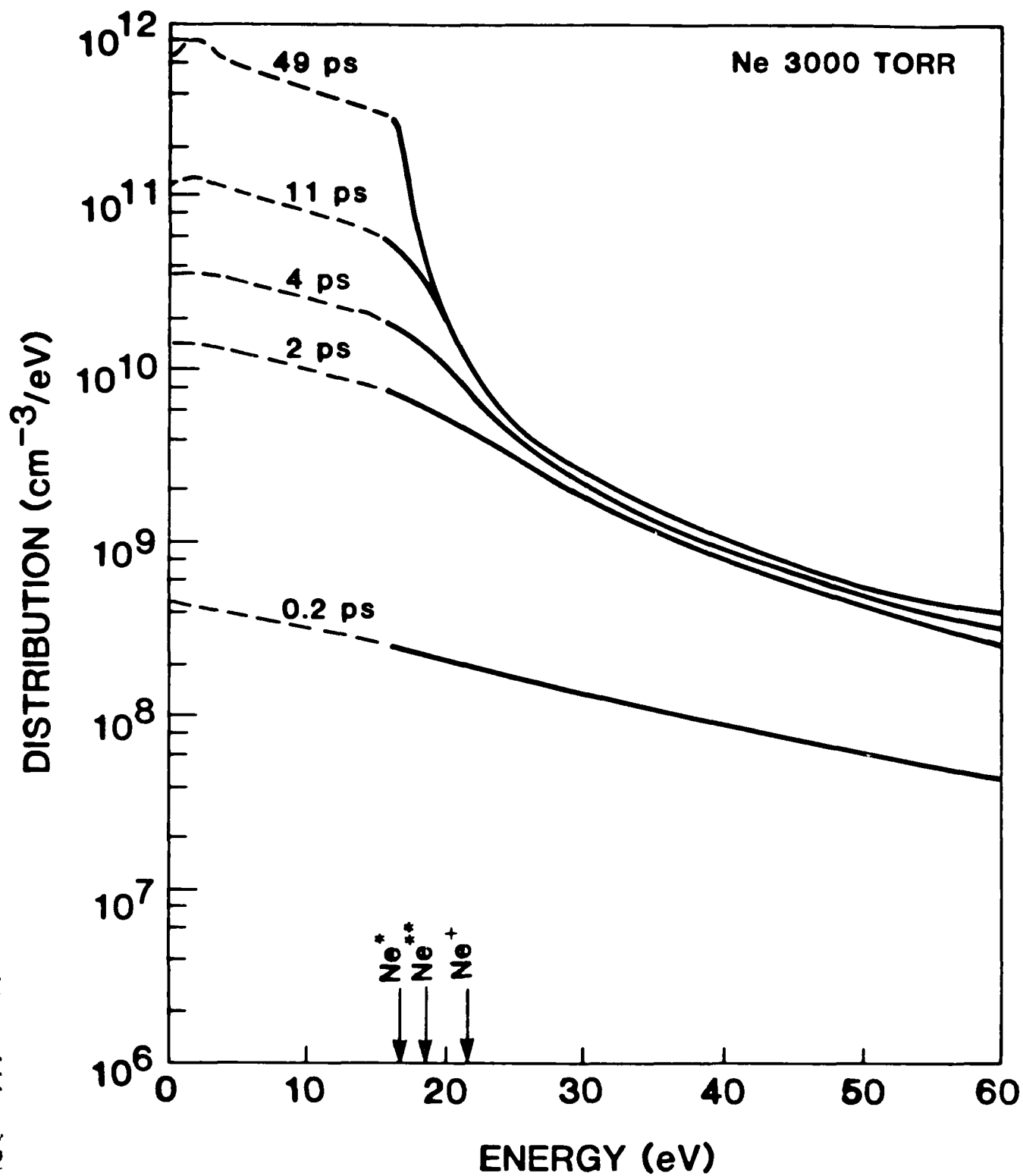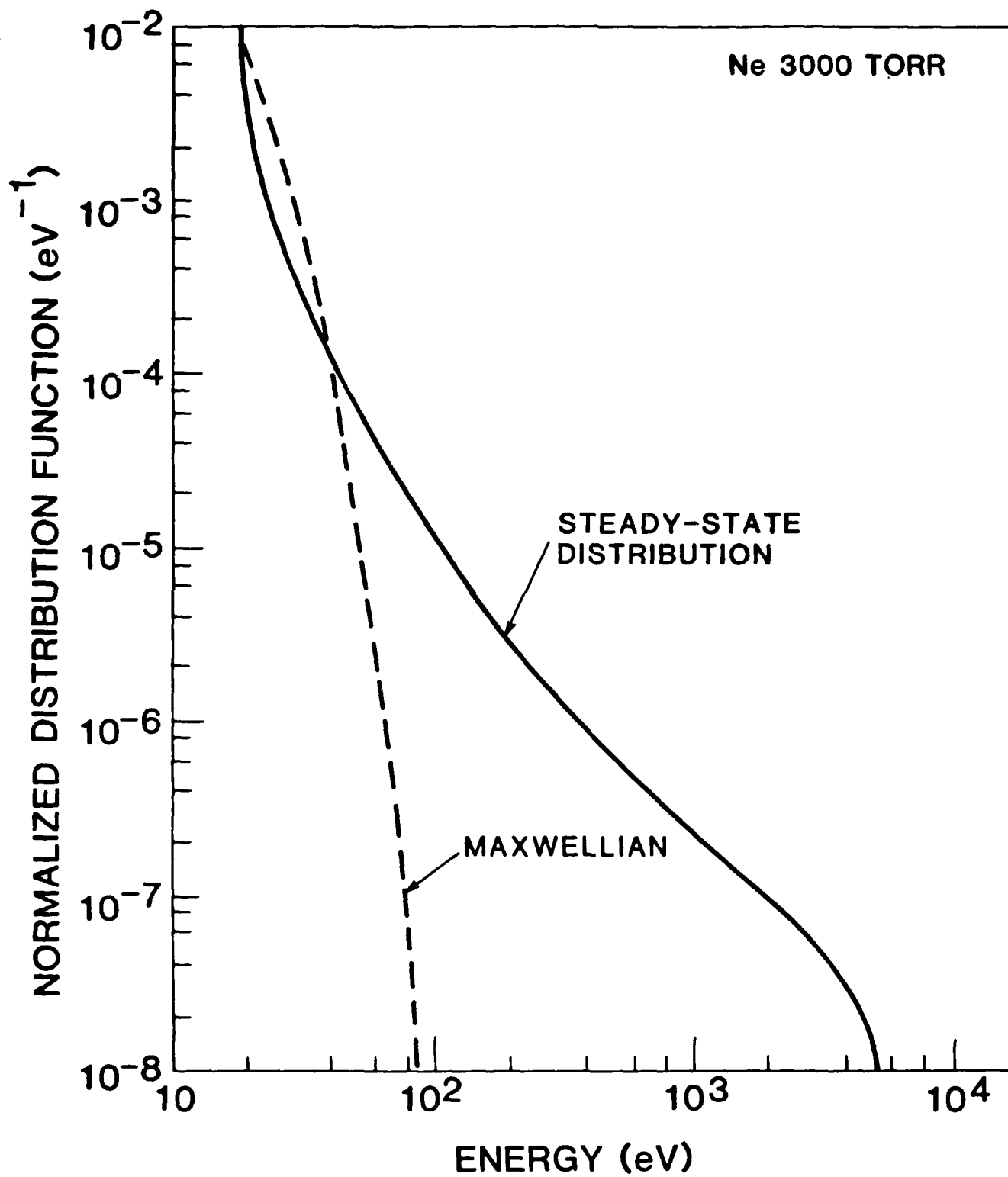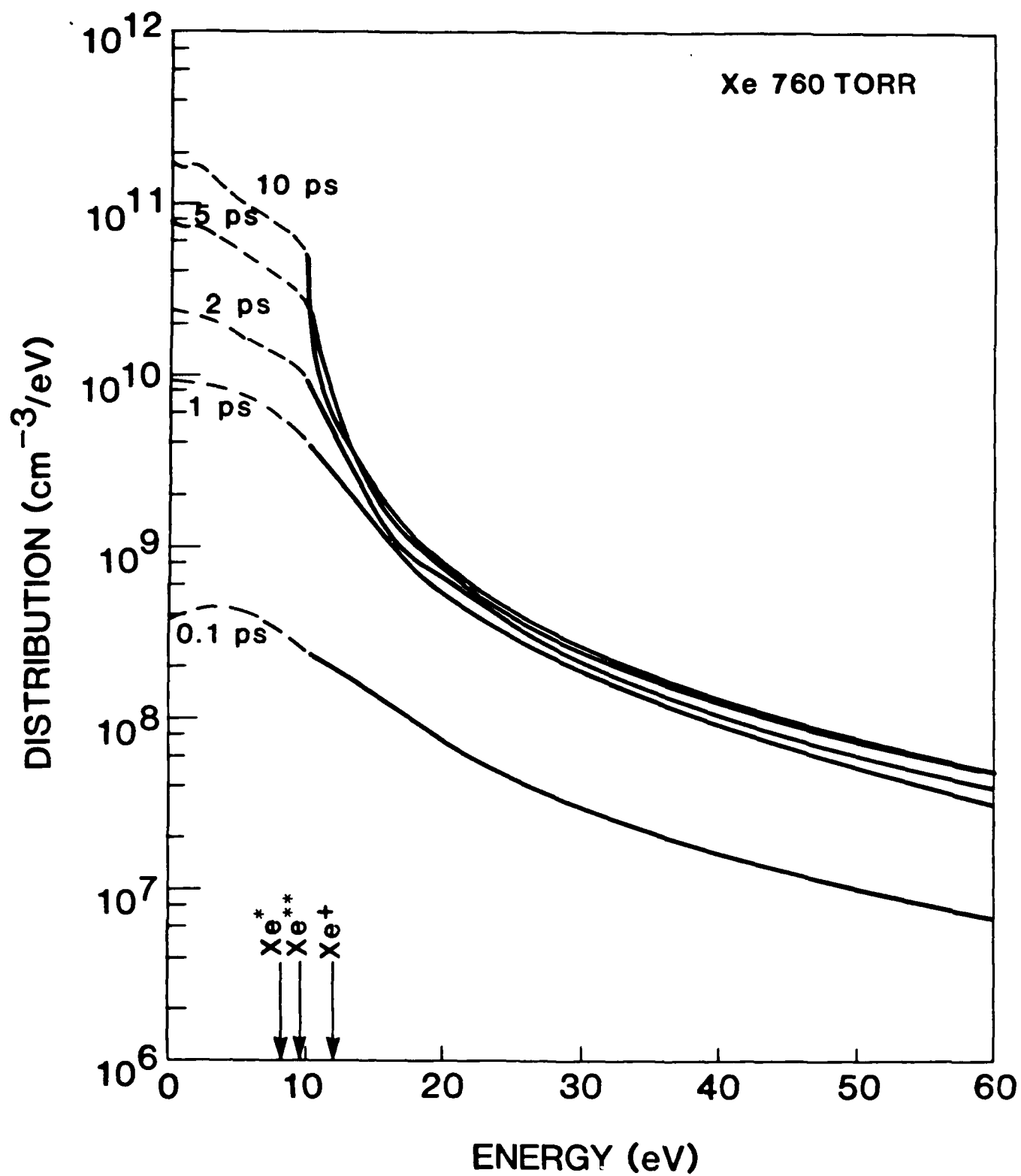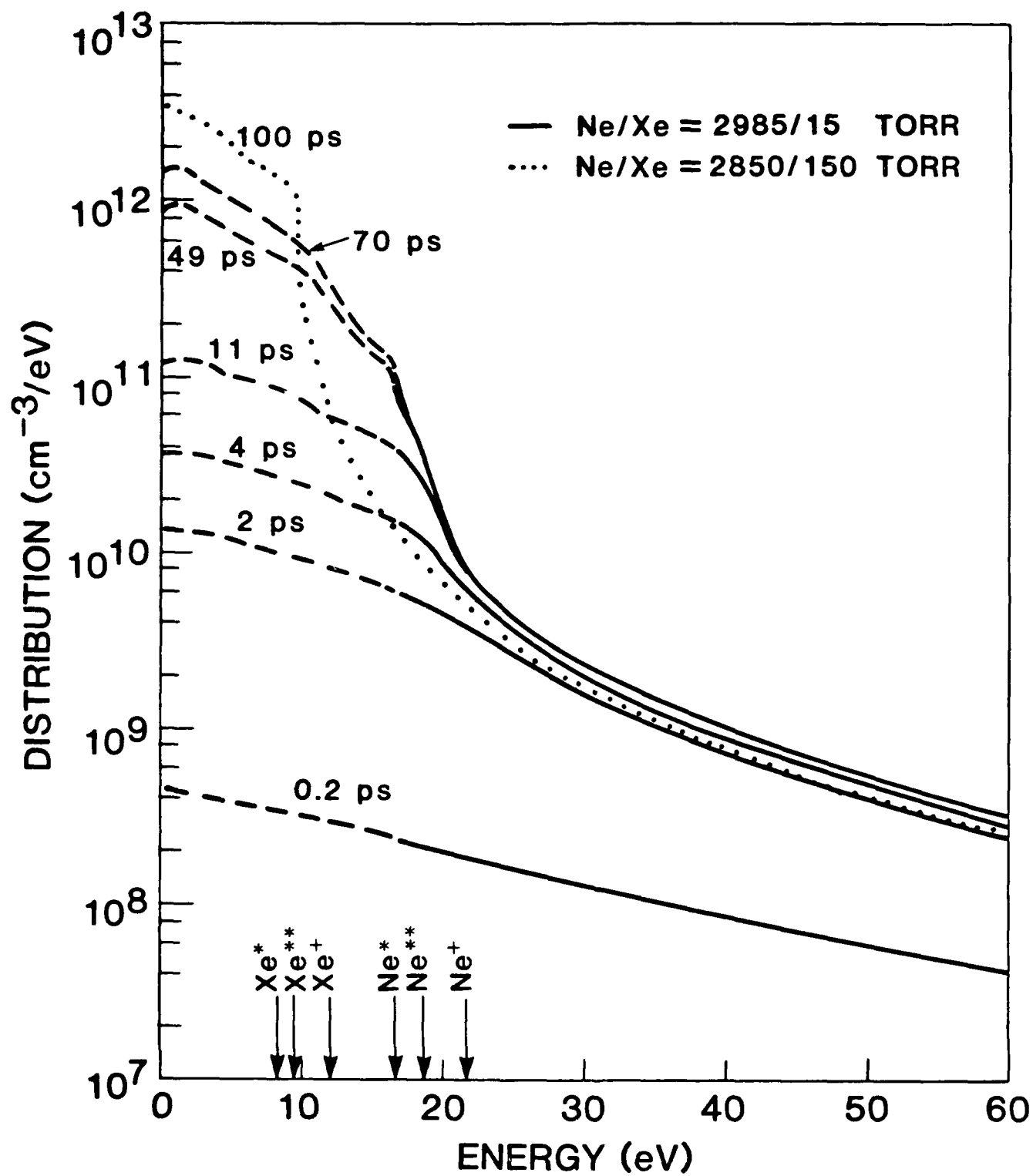
Fig. 1

41

Fig. 2

42

Fig. 3

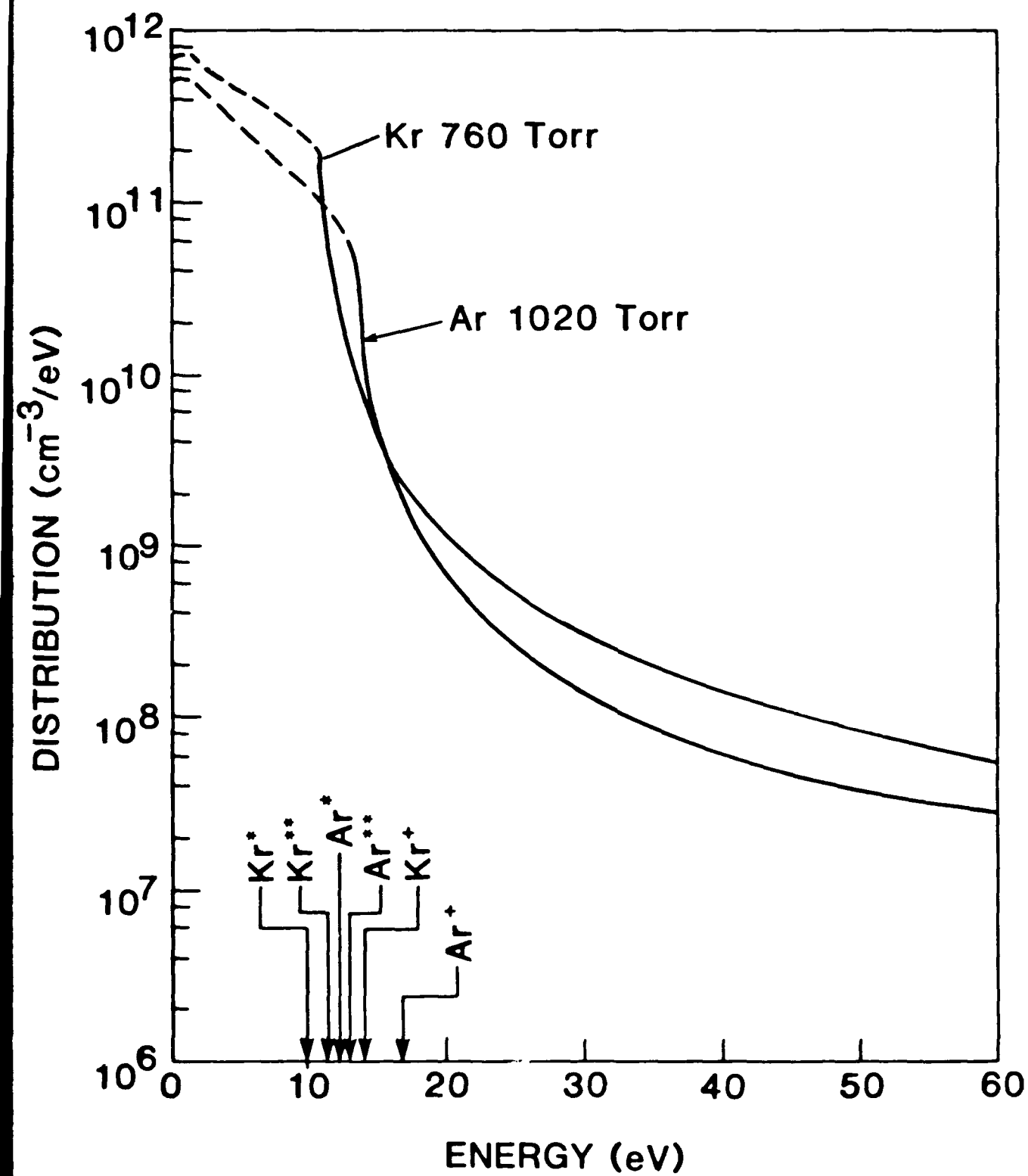43

Fig. 4
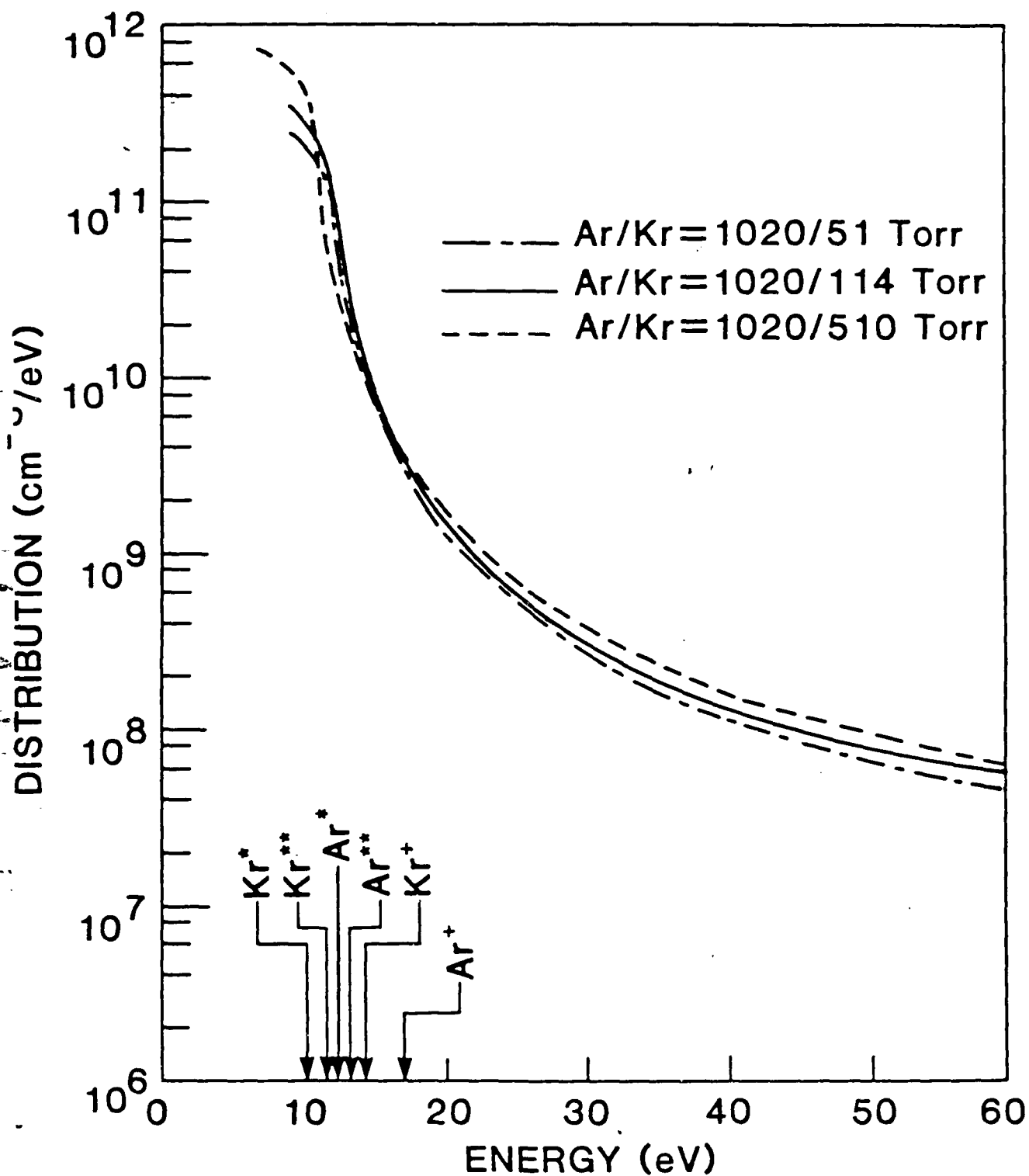
44
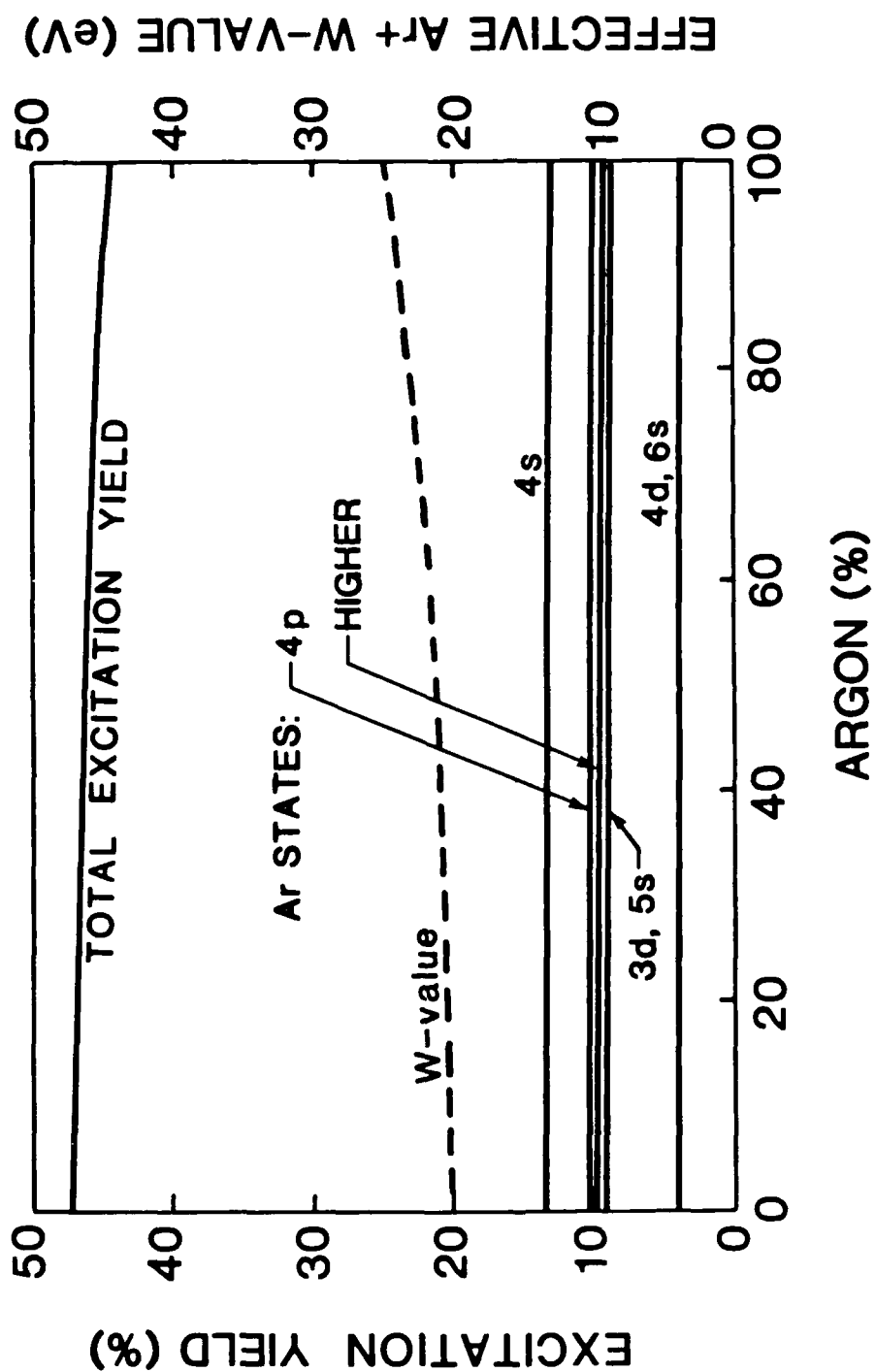
Fig. 5

45

Fig. 6

46

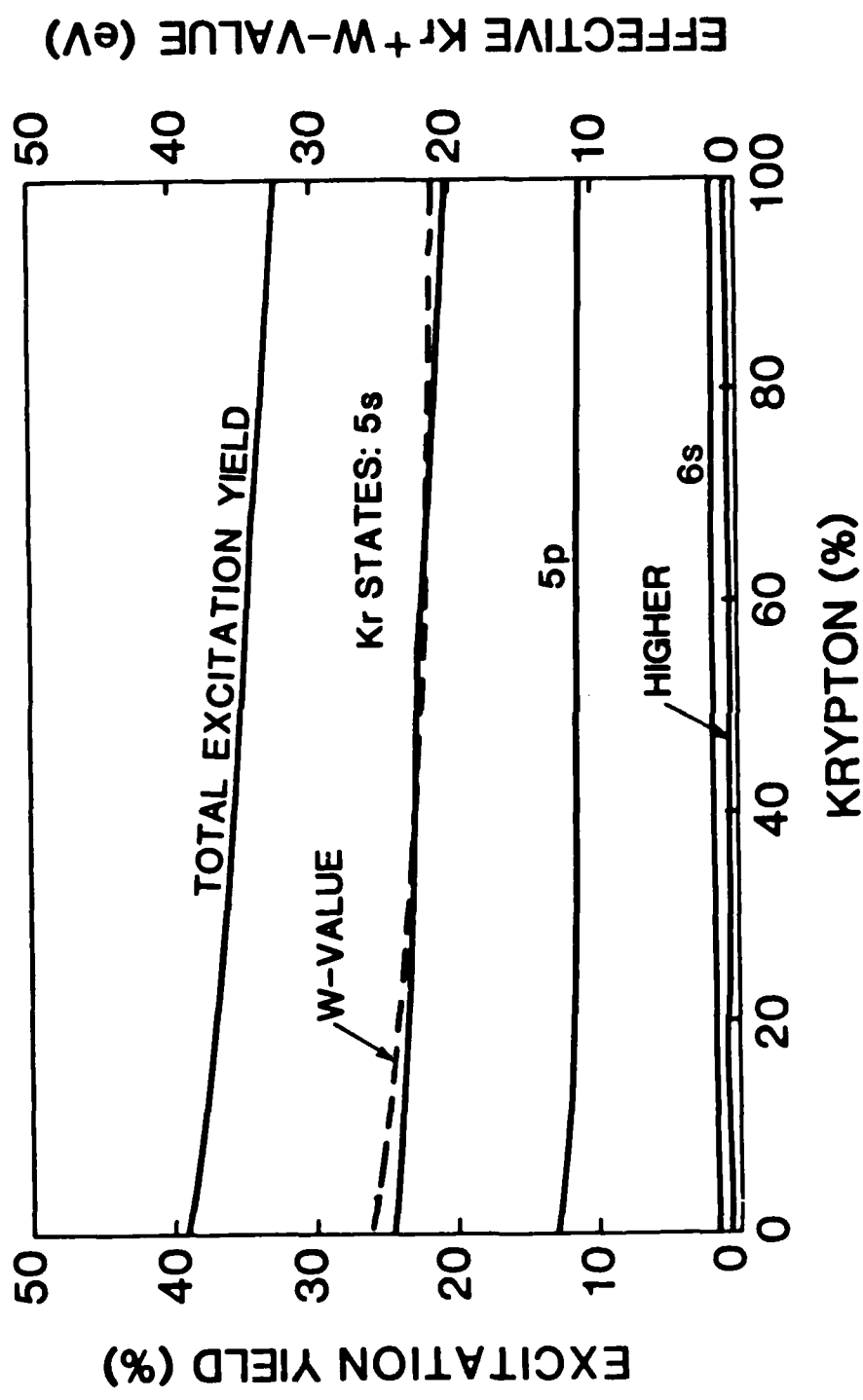Fig. 7

Fig. 8

48
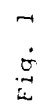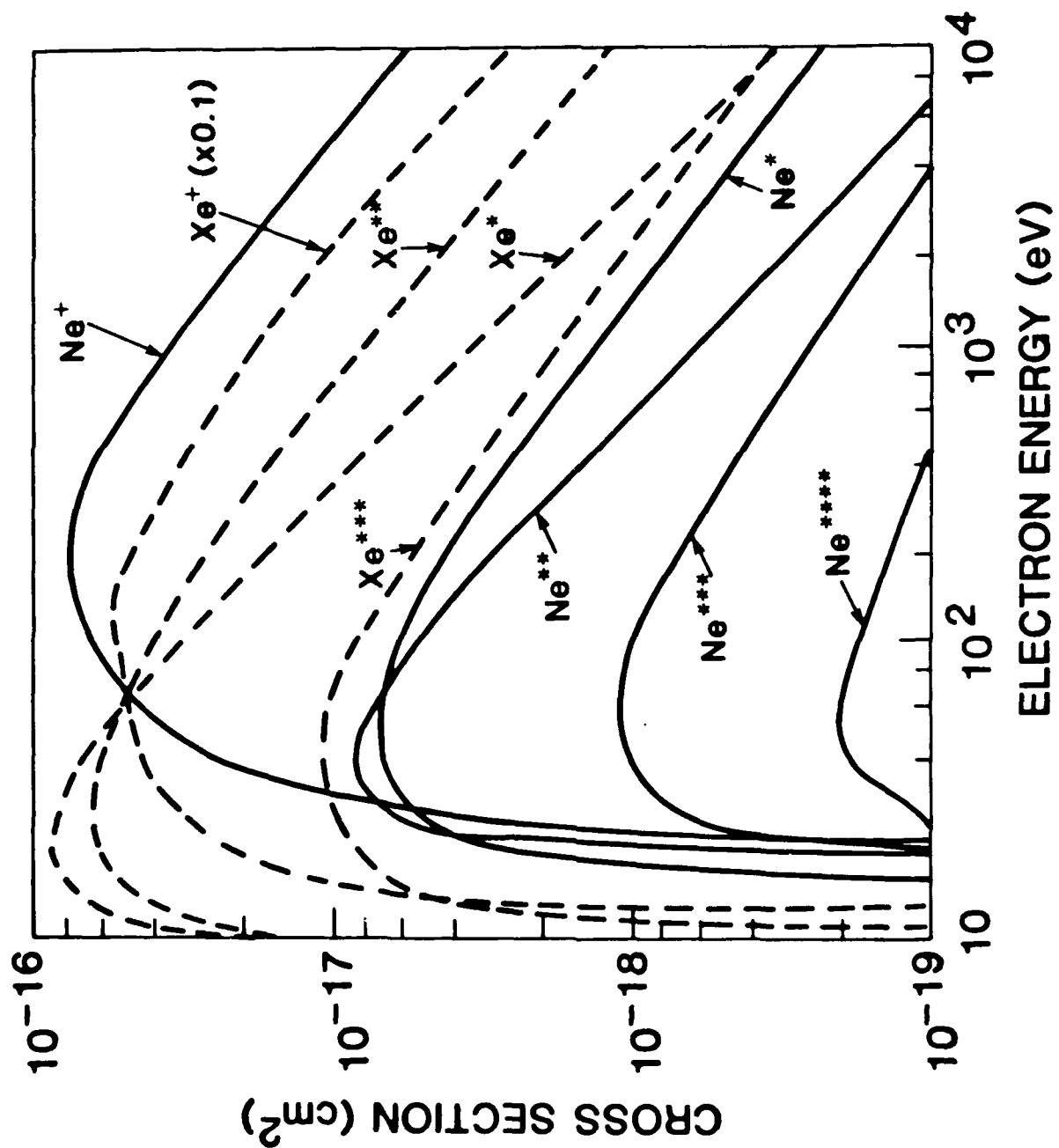
Fig. 9

49

Fig. 10

Low-Energy Electron Distribution

in

Electron-Beam Excited XeCl Laser Mixtures

F. Kannari and W. D. Kimura

Spectra Technology, Inc.

2755 Northup Way

Bellevue, Washington 98004-1495

Abstract

The electron energy distributions for energies lower than 17 eV and their time dependent evolution are calculated for electron-beam (e-beam) excited Ne/Xe/HCl mixtures. A time dependent Boltzmann equation including all interactions between electrons and ground or excited state species is solved together with a detailed full kinetics model for XeCl lasers. Effects of electron-electron collision, HCl concentration, and excitation rate on the steady-state electron energy distribution are examined.

High pressure gases excited by intense electron-beams (e-beams) have been used to produce high densities of excited or ionized species leading to high power laser emission, such as in rare gas dimer and rare gas halide lasers. In such a plasma, most of the ions and excited species are formed either directly by the primary or the high energy secondary electrons. At high electron densities, the effects of electron impact excitation and quenching can be important even for relatively low energy electrons (lower than the ionization energies for the rare gas constituents).

The mechanism of electric discharge excitation employed in discharge pumped lasers is fairly well understood, and theories for the electron energy distribution[1-3], which relates the discharge parameters to the excitation rates, are available. However, a similar detailed electron energy distribution theory has been lacking for e-beam excited lasers. Models published to date typically assume that electrons are in a Maxwellian energy distribution with either a constant or a time dependent average electron temperature; this is particularly true for rare gas halide lasers[4-8].

Eliott and Greene[9], and Bretagne et al.[10,11] have reported electron energy distribution functions for pure xenon and argon gases, respectively. Their calculated distribution functions, using a detailed Boltzmann equation solver that includes the Rockwood formalism[12] for electron-electron and elastic collisions, show significant departures from Maxwellian distributions. Similar calculations performed for Ar/F_2 mixtures have been reported by Rozenberg et al.[13]. In their mixtures, the dissociative electron

attachment reaction of F_2 plays an important role in influencing the distribution of electrons lower than the excitation threshold energy of argon gas (11.8 eV). Fluorine tends to increase the average electron energy as a result of removal of low energy electrons by attachment reactions.

In rare gas mixtures containing a trace of HCl, the relatively large vibrational excitation cross-sections of HCl and the large dissociative attachment rate constants of vibrationally excited HCl can significantly affect on the electron distribution function. A detailed calculation of the electron distribution function is paramount in order to obtain the correct rates for reactions between electrons and ground or excited state species. These rates are necessary for predicting the densities of various transient species in laser gas plasmas, such as the secondary electrons, the halogen molecules, and the excited rare gas atoms.

In this letter, calculated results of the low energy electron distributions in e-beam excited Ne/Xe/HCl laser mixtures are described. The numerical technique, which employs a Boltzmann equation that includes all the collisional processes in which the electrons are involved, is the same as the one applied by Bretagne et al.[11] to pure argon gas.

The high energy electron distribution function calculated for a Ne/Xe mixture using a reduced Boltzmann equation, which was reported in our previous paper[14], is used as the driving term for the full Boltzmann equation of the low energy electron distribution. Since electrons higher than the excitation

threshold of neon (16.7 eV) establish a steady-state distribution in a very short time (less than 100 ps), the high energy distribution function can be treated as static in overall shape, but changing in magnitude proportional to the temporal change of the e-beam excitation rate. It should be emphasized that W-values (defined as the energy required to form an electron-ion pair) for rare gas ion formation, and yields of rare gas excited species relative to the ion formation, which are typically used in models for e-beam excited gas lasers, are not used in our calculations. In our previous paper[14], it was concluded that the dependences of these values is sensitive to the mixture ratio of the rare gases (e.g. Ar/Kr or Ne/Xe) and that the definitions of these parameters can be ambiguous, particularly when applied to the minor rare gas in these mixtures. Therefore, by using a high-energy electron distribution function rather than these macroscopic values, the production of ions and excited species can be more accurately predicted.

As reported by Bretagne et al.[11], the evolution of the distribution function $f(\epsilon,t)$, for energy ϵ (lower than the excitation threshold energy of neon) is expressed as follows:

$$\frac{\partial}{\partial t}f(\epsilon,t) = \left(\frac{\partial f}{\partial t}\right)_{el(e-e)} + \left(\frac{\partial f}{\partial t}\right)_{el(e-n)} + \left(\frac{\partial f}{\partial t}\right)_{inel} + I(t)S\left(\epsilon_p,\epsilon\right), \qquad [1]$$

where the first term on the right-hand side corresponds to electron-electron collisions; the second to elastic electron-ground state species collisions; the third to inelastic collisions including ionizations, excitations, superelastic de-excitations, attachments, recombinations, and Penning effects; and the last term to the production of secondary electrons with energy ϵ by

4

the primary electrons ϵ_p of the e-beam.

Electron-electron and electron-neutral collisions are modeled using the Rockwood[12], and Elliott and Greene[9] formulas as modified by Bretagne et al.[11] to adapt to non-equal segments for the energy intervals. Ionization terms are calculated using differential ionization cross-sections reported by Green and Sawada[15] for ground state rare gases and using empirical formulas obtained for HCl and excited rare gas atoms[14]. The set of cross-sections given in our previous paper[14] are used to calculate the excitations of the rare gases. Cross-sections reported by Davis[16] are used for HCl ionizations and excitations, and those reported by Domcke and Mundel[17] are used for dissociative attachment reactions with ground and vibrationally excited HCl.

During the calculation, the initial secondary electron production rates for each of the energy segments lower than 16.7 eV are calculated from the e-beam electron energy and the static high-energy electron distributions. These calculations are performed only once at the beginning. Afterwards, the rates are adjusted in direct proportion to the time-varying e-beam excitation rate and the density of parental species during e-beam excitation. The differential equations [i.e. Eq. (1)] obtained for the electron populations in each of the energy segments lower than 16.7 eV are simultaneously solved using a fourth-degree Runge Kutta integration method. An important difference between our calculations and the ones done by Elliott and Greene[9], or Bretagne et al.[11] is that a detailed heavy particle kinetics model[6] is simultaneously solved together with the Boltzmann equation. This permits a more accurate

5

accounting of the transient ions and excited species densities that are involved in the Boltzmann equation.

Running both models in a true continuous parallel mode is computationally prohibitive on the computer system (VAX 11/780) used for this work. Therefore, the following algorithm is used to conserve on computation time: 1) During the kinetics calculation, the electron energy distribution is frozen, thereby making the reaction rate constants involving electrons constant. 2) When the electron density changes by 5%, the Boltzmann calculation is called. During the Boltzmann calculation, the kinetics calculation is stopped, and all the densities of species are frozen. The Boltzmann equation calculation is continued until the energy distribution function reaches steady-state using a convergence factor of 10^{-2} (defined as the ratio of the previous calculated value to the current calculated value). 3) The kinetics calculation with new rate constants for the electron reactions restarts and the process repeats itself.

Figure 1 shows the time evolution of the low-energy electron distribution function calculated for a XeCl laser mixture of Ne/Xe/HCl = 2980/15/4.8 Torr. An e-beam current waveform from the Tahoma laser device[18] at an excitation rate of 250 kW/cm^3 and a pulse width of 500 ns full width at half maximum (FWHM) is used. Early in time, the distribution function is truncated near the first excitation threshold of xenon (8.4 eV), which was also observed during the high energy electron distribution calculation[14], and indicates that ionization and excitation processes of the ground state rare

6

gas quickly remove electrons higher than the rare gas energy threshold. Structure seen on the distribution curve at energies less than 10 eV are caused by vibrational excitation of HCl.

At later times, as the electron number density increases, the electron-electron collisions tend to redistribute the low energy electrons towards a Maxwellian distribution at an average electron energy of ≈ 1.9 eV during the time interval 50-600 ns. Superelastic de-excitation reactions also become important as the densities of excited species increases and contribute towards a smoothing out of the distribution function caused by heating of the lower energy electrons. At this HCl concentration, dissociative attachment and vibrational excitation reactions are slower than the redistribution processes.

There are two important points to be noted. First, the induction time to establish a steady state distribution is ≈ 50 ns for the condition studied. This time depends on the risetime of the current pulse and the excitation rate. Second, the part of the distribution function higher than the first excitation threshold of xenon shows significant departure from a Maxwellian distribution, even with the redistribution effects caused by electron-electron processes and superelastic de-excitation reactions. Therefore, assuming a Maxwellian distribution for the secondary electrons can cause a significant error during the calculation of the rate constant of electron reactions, which will result in errors in the transient species densities.

In order to confirm the effect of electron-electron collisions, Fig. 2 shows the results of the steady-state electron distribution as a function of the e-beam excitation rate calculated including the electron-electron collision process [Fig. 2(a)] and without it [Fig. 2(b)]. The gas mixture is the same as in Fig. 1. It is clear that even at a low excitation rate of 2 kW/cm^3, the electron-electron collision process is very important. The structures seen on the curves in Fig. 2(b) exactly correspond to the vibrational excitation of HCl.[16] From Fig. 2(a), however, it is observed that the distribution functions at low excitation rates do slightly depart from Maxwellian distributions, although they are smoothed out. At this particular HCl concentration, the required excitation rate to establish a Maxwellian distribution in the low energy region is approximately 50 kW/cm^3.

Figure 3 shows steady-state distribution functions calculated for various HCl concentrations. The e-beam excitation rate is kept constant at 200 kW/cm^3. Since the distribution function in the low energy region is established as a result of the balance between the electron-electron collisions and vibrational excitation of HCl, HCl excitations become important at high HCl concentrations and quench electrons higher than the vibrational excitation threshold.

Under the more specialized situation of relatively high excitation and relatively low initial HCl concentration, an alternative simpler model that assumes a quasi-Maxwellian distribution is possible. Under these conditions, electron-electron collisions can effectively establish a Maxwellian

distribution for the low energy electrons. In this simplified approach, the distribution function of the low energy region would be treated as Maxwellian whose characteristic temperature is defined by solving an energy balance equation for the low energy electrons during excitation. It should be emphasized that even for this specialized case, only the low energy electron distribution can be approximated as Maxwellian. The high energy regions would still be treated as a static non-Maxwellian distribution as calculated from the reduced Boltzmann equation[14]. Hence, this simplified approach still differs from the models which assume that the entire distribution is Maxwellian.

The modeling process described in this letter, in conjunction with that reported previously for the high energy electron distribution, is a more accurate alternative to the usual modeling methods that use stopping power, W-values of pure rare gases, excitation yields, and a Maxwellian assumption for the entire electron energy distribution. This new approach should improve the performance of the model predictions. It is also applicable to other kinds of lasers excited by e-beams.

REFERENCES

1. J. H. Jacob and J. A. Mangano, Appl. Phys. Lett., 28, 724 (1976).

2. W. H. Long, Jr., Appl. Phys. Lett., 31, 391 (1977).

3. T. H. Johnson, L. J. Palumbo, and A. M. Hunter, II, IEEE J. Quantum Electron., QE-15, 289 (1979).

4. C. W. Werner, E. V. George, P. W. Hoff, and C. K. Rhodes, IEEE J. Quantum Electron., QE-13, 769 (1977).

5. L. A. Levin, S. E. Moody, E. L. Klosterman, R. E. Center, and J. J. Ewing, IEEE J. Quantum Electron., QE-17, 2282 (1981).

6. F. Kannari, A. Suda, M. Obara, and T. Fujioka, IEEE J. Quantum Electron., QE-19, 1587 (1983).

7. F. Kannari, M. Obara, and T. Fujioka, J. Appl. Phys., 57, 4309 (1985).

8. K. S. Jancaitis, Lawrence Livermore National Laboratory, UCRL-53465, 1983 (unpublished).

9. C. J. Elliott and A. E. Greene, J. Appl. Phys., 47, 2946 (1976).

10. J. Bretagne, G. Delouya, J. Godart, and V. Puech, J. Phys. D:Appl. Phys., 14, 1225 (1981).

11. J. Bretagne, J. Godart, and V. Puech, J. Phys. D:Appl. Phys., 15, 2205 (1982).

12. S. D. Rockwood, Phys. Rev., A8, 2348 (1973).

13. Z. Rozenberg, M. Lando, and M. Rokni, Phys. Rev. A, 35, 4151 (1987).

14. F. Kannari and W. D. Kimura, "High-Energy Electron Distribution in Electron-Beam Excited Ar/Kr and Ne/Xe Mixtures," submitted to Journal of Applied Physics, Ms. #R-1327.

15. A. E. S. Green and T. Sawada, J., Atm. Terr. Phys., 34, 1719 (1972).

16. D. K. Davis (private communication).

17. W. Domcke and C. Mundel, J. Phys. B: At. Mol. Phys., 18, 4491 (1985).

18. W. D. Kimura, D. R. Guyer, S. E. Moody, J. F. Seamans, and D. H. Ford, Appl. Phys. Lett., 49, 1569 (1986).

FIGURE CAPTIONS

Fig. 1. Temporal evolution of the low-energy electron distribution function calculated for a mixture of Ne/Xe/HCl = 2980/15/4.8 Torr by solving the time-dependent Boltzmann equation together with a full kinetics model. The excitation rate is $\approx$250 kW/cm^3 and the e-beam pulse width is 500 ns (FWHM). The distribution functions between 100 ns and 560 ns are approximately same as the one at 100 ns.

Fig. 2. Steady state low-energy electron energy distribution functions as a function of e-beam excitation rate for a mixture of Ne/Xe/HCl = 2980/15/4.8 Torr. (a) Electron-electron collisions included. (b) Electron-electron collisions excluded.

Fig. 3. Steady state low-energy electron energy distribution functions as a function of HCl concentration. The mixture contains 0.5% Xe with the balance Ne to 3000 Torr. The e-beam excitation rate is 200 kW/cm^3. Electron-electron collisions are included.
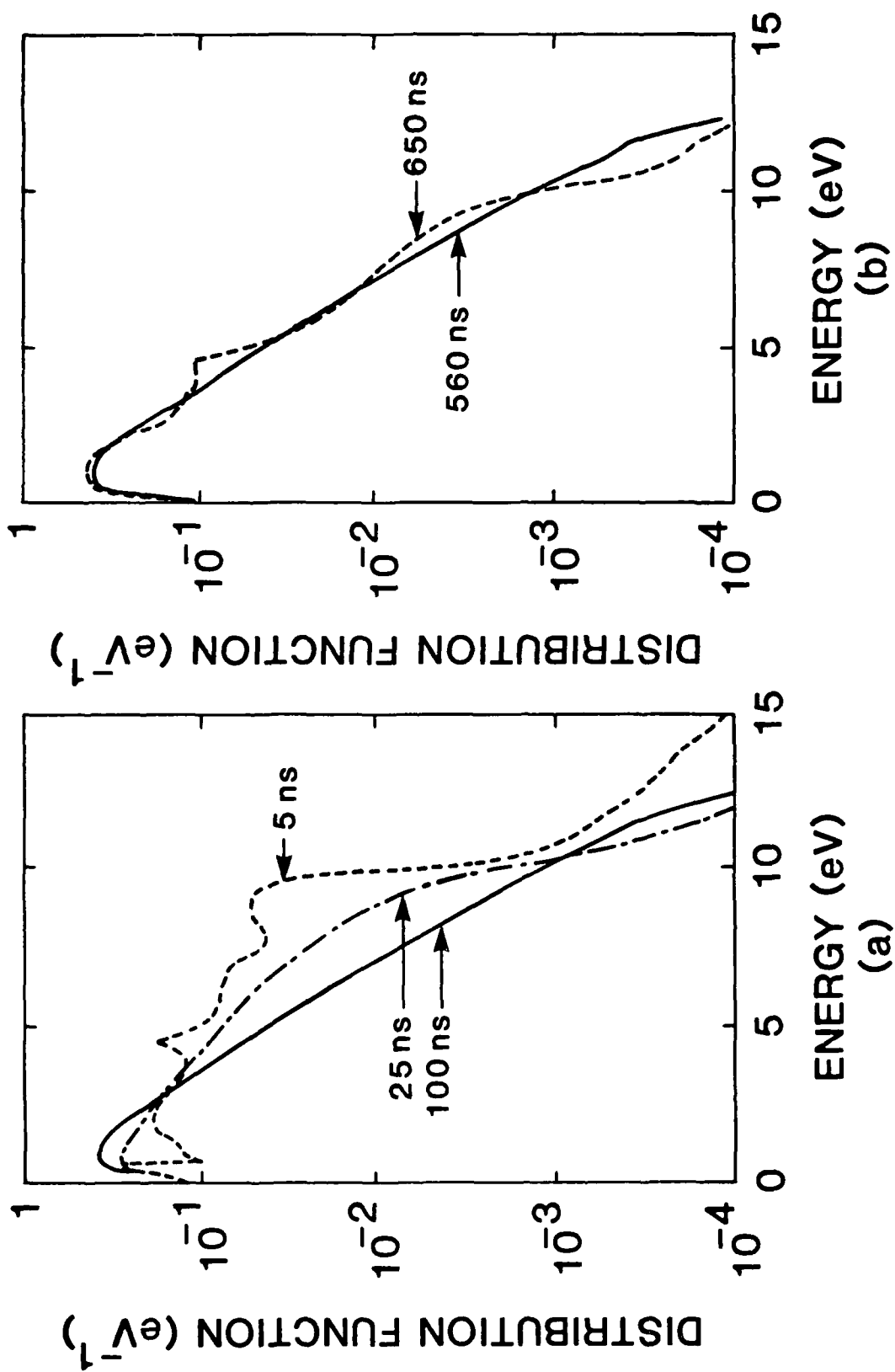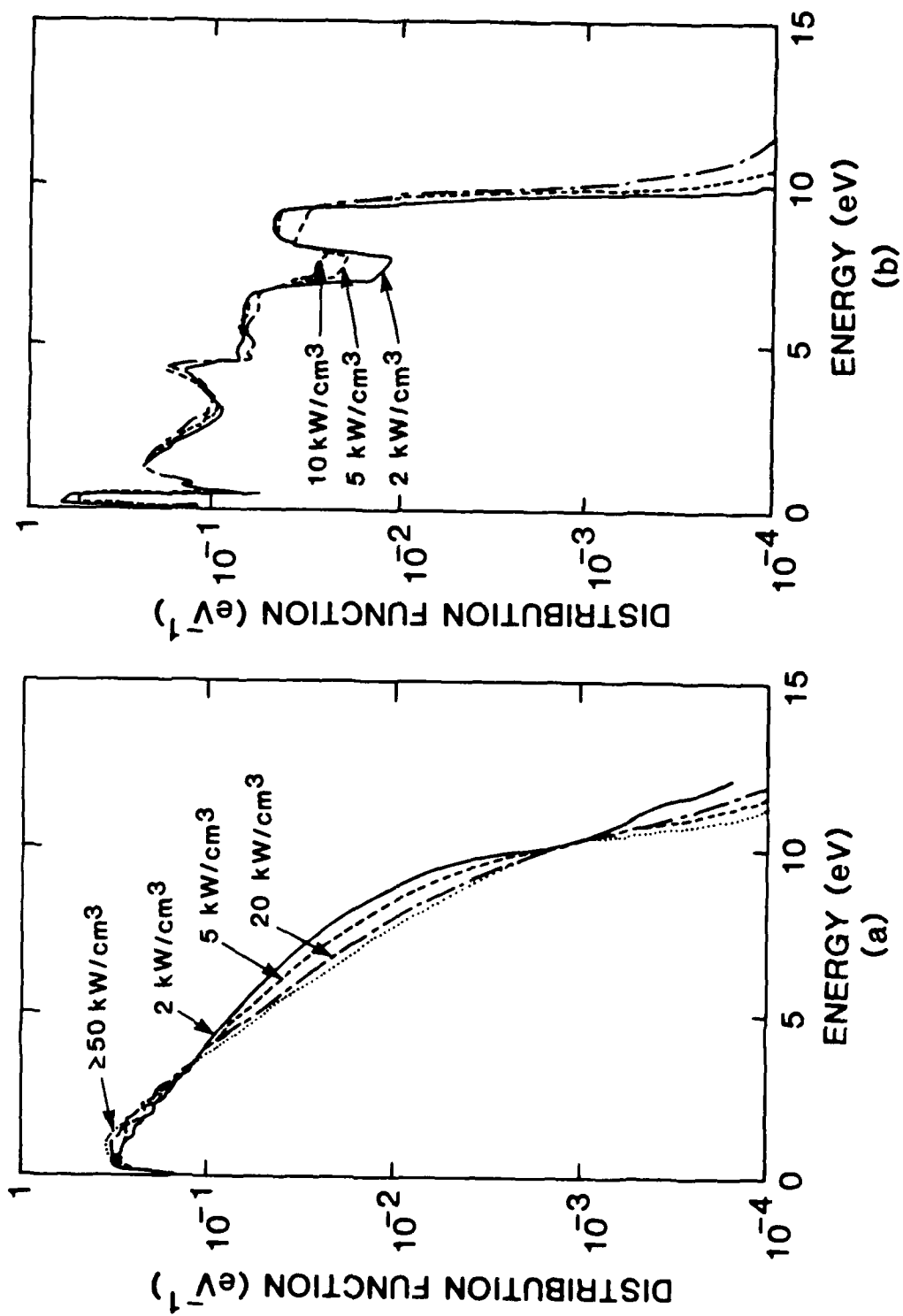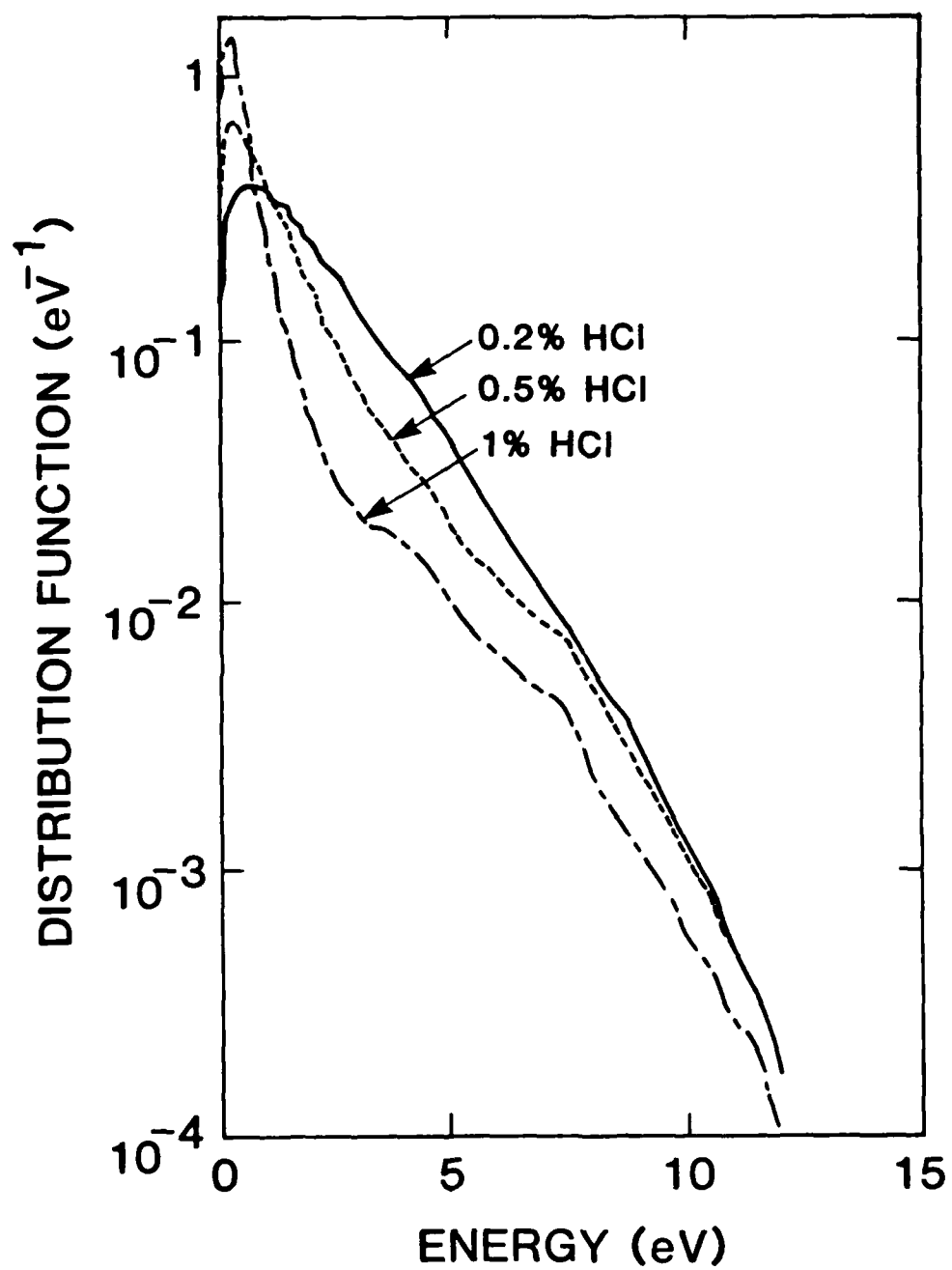
Figure 1

13

Figure 2

14

Figure 3

15

END

DATE

FILMED

6- 1988

DTIC